The Effects of Wet Supercritical CO_2 Treatment on the Storage Potential of Zululand (South Africa) Sandstones.

PhD Thesis

Prepared by

Patience Mavhengere (698151)

Submitted to

School of Chemical and Metallurgical Engineering, Faculty of Engineering and the Built Environment, University of the Witwatersrand, Johannesburg, South Africa in fulfilment of the requirements for the degree of Doctor of Philosophy.

Supervisor(s): Professor Nicola Wagner and Doctor Nandi Malumbazo

April 2021

Declaration

I declare that this thesis is my own, unaided work. The thesis is being submitted for the Degree of Doctor of Philosophy at the University of the Witwatersrand, Johannesburg.

It has not been submitted before for any degree or examination at any other University.

P Mavhengere

_____

11th day of May 2022 at Johannesburg

Abstract

Understanding the mineral and microstructure changes in sandstone samples during wet supercritical CO_2 gas treatment is an important aspect of geological CO_2 sequestration. In order to gain insight into geological storage of CO_2 in South Africa, five core samples extracted from the reservoir caprock and separate sandstone aquifers within the Zululand Basin were studied. The samples were treated with CO_2 gas streams at typical reservoir temperature and pressures (120 bar and 45 ºC, and 175 bar and 73 ºC) under wet conditions. High pressure Parr reactors were used for storing the rock-gas-water mixtures for up to two months using a water:rock ratio of 23:1. Tests were conducted using pure CO_2 and a 99% CO_2 and 1% SO_2 mixed gas stream. Due to the prohibitive costs associated with CO_2 purification, the knowledge of the consequences of key impurities relevant to geological sequestration is critical.

Pre-and post- CO_2 /CO_2-SO_2 treatment characterisation was conducted using X-ray Diffraction (XRD) analyses, Fourier transform infrared spectroscopy (FTIR), and low-pressure gas adsorption (LPGA). In line with literature in the field, varying mineral alterations were observed in all CO_2 treated samples, mainly comprising of calcite, plagioclase and smectite dissolution and the precipitation of quartz, plagioclase, calcite and smectite. The formation of dissolution pores and pore clogging was indicated. In line with XRD results, increased microstructure heterogeneity was indicated in the FTIR profiles after CO_2 treatment through reduced peak intensities. Increases in the adsorption capacity, surface area and pore volume were observed in all samples except for the ZA sample, which showed contradicting results. This was attributed to the significant quartz precipitation observed in the sample.

Two samples (ZC and ZG) were further treated with CO_2-SO_2 gas mixture. After treatment with CO_2-SO_2 gas mixture, increases in mineral reactivity were observed in the ZC sample along with gypsum precipitation, indicating potential improvement in the lateral seal's self-sealing capacity. The introduction of SO_2 lead to the increase in quartz and plagioclase precipitation and increased dissolution of smectite and stilbite in the ZG sample. Minor changes in the pore structure were reported. The study presents a novel investigation of the changes expected to take place during CO_2 injection in sandstone basins. The documented findings provide a crucial foundation for the prediction of long-term CO_2 sequestration effects in the Zululand Basin of South Africa.

Dedication

This thesis is dedicated to my inspirational husband Tafara Mavhengere, my loving parents, Sheillah and George Moyo and my beautiful children, Naomi and Rachel Mavhengere. For their unwavering support and dedication to my success, I am grateful.

Acknowledgements

Firstly, I would like to acknowledge God for the opportunity to undertake this study. I hope that it will be of value to the Zululand Basin Pilot Carbon Dioxide Sequestration Project. To my husband, for all the support throughout this journey, thank you. To my mother, for the constant encouragement, I hope I have made you proud. To my father, thank you for the foundation you laid for me to get to where I am.

With great gratitude, I acknowledge my supervisors, Professor Nicola Wagner and Dr Nandi Malumbazo, the time and dedication they put into providing guidance during this study is remarkable and deeply appreciated.

I would like to acknowledge the funding and partnership offered by the South African Centre for Carbon Dioxide Capture and Storage (SACCCS); SACCCS funded the purchase of the high-pressure reactors used in this study. Funding for the characterisation analyses was provided by Professor Nicola Wagner. The equipment was initially housed at the council for Geosciences, and later at the University of the Witwatersrand.

Lastly, I would also like to acknowledge Minova RSA, for funding the last two years of this study, thank you.

TABLE OF CONTENTS

LIST OF FIGURES

LIST OF TABLES

1 CHAPTER 1: INTRODUCTION

1.1 Background

Carbon dioxide capture and geological storage (CCS) has come to the forefront of carbon dioxide (CO_2) mitigation technologies in recent years (Reichle *et al.*, 1999; Rao and Rubin, 2002; IPCC, 2005; Bae and Bhatia, 2006; Ellis *et al.*, 2010; Wang *et al.*, 2011, 2012; Leung *et al.*, 2014). Up to 90% reduction in CO_2 emissions from large point sources is potentially possible through CCS (Leung *et al.*, 2014). Fossil fuels have been reported to account for up to 78% of the cumulative CO_2 gas emissions from stationary sources globally, with 85% of the energy required for industrial applications supplied by the combustion of fossil fuels (Rao and Rubin, 2002; Stuart Haszeldine, 2009). If the use of fossil fuels for energy production continues at a rate of as little as 10% or more than the present rate, the use of CCS technologies will become inevitable to reduce CO_2 in the atmosphere (Stuart Haszeldine, 2009). CCS technologies present the advantage of an interim process that could enable the transition away from fossil fuels by providing the much-needed time for the development of alternative energy technologies (Rao and Rubin, 2002; Ghaderi *et al.*, 2011). In South Africa, up 90% of the primary energy needs are derived from coal (Beck, 2014). The application of CCS offers fossil fuel dependant countries like South Africa an attractive opportunity to mitigate CO_2 emissions in line with global targets (van Soest *et al.*, 2021).

Geological storage options for CO_2 emissions range from saline aquifers to depleted gas and oil reservoirs, as well as unminable coal seams (Holloway, 1997; Bachu, 2000, 2007; Bachu *et al.*, 2007; Busch *et al.*, 2008; Leung *et al.*, 2014). Deep saline aquifers are proven viable CO_2 storage sites that present the largest potential storage capacity amongst geological storage options (Hsieh *et al.*, 2017). Different CO_2 gas trapping mechanisms are applicable to coal deposits compared to carbonate reservoirs and sandstones. The adsorption trapping that takes place in coal allows for greater volumes and higher densities of CO_2 gas to be stored at shallower depths as compared to the latter (Golding *et al.*, 2011). CO_2 gas trapping in sandstones and carbonate reservoirs occurs in the form of a much slower mineral trapping mechanism in the mineral phase and solubility trapping in the formation waters (Xu *et al.*, 2007; Golding *et al.*, 2011). Shales have been reported to be capable of storing significant

amounts of CO_2 gas which may be dissolved in formation fluids, sorbed into organic compounds or mineral surfaces, or trapped by mineral reactions (Krooss *et al.*, 2002; Busch *et al.*, 2008). Thus, sedimentary rocks (sandstones, shales and coal deposits), are reported to be the major potential hosts for CO_2 sequestration (Bachu, 2000).

Depending on the adopted capture technology and plant type, the captured CO_2 emissions for injection into geological formations will typically contain impurities (de Visser *et al.*, 2008; Stuart Haszeldine, 2009; Koenen *et al.*, 2011). These impurities could be made up of: SO_2, SO_x, H_2S, NO_x and N_2, (Crandell *et al.*, 2010; Liu and Shao, 2010; Wang *et al.*, 2011, 2012; Ziabakhsh-Ganji and Kooi, 2014; Pearce *et al.*, 2015; Gimeno *et al.*, 2017, 2018; Vu *et al.*, 2018). The presence of such impurities is believed to influence the dynamical and thermal properties of the fluid streams, leading to significant physical and chemical effects on the geological material and cap-rock. However, the effects of these impurities on short- and long-term geological storage are uncertain (Xu *et al.*, 2007; Crandell *et al.*, 2010; Heeschen *et al.*, 2011; IEA, 2011; Koenen *et al.*, 2011; Ziabakhsh-Ganji and Kooi, 2014; Pearce *et al.*, 2015; Gimeno *et al.*, 2017, 2018; Vu *et al.*, 2018). This uncertainty is reported to be one of the current challenges faced in the implementation of large-scale CO_2 injection projects; hence the need for guidelines and regulations specifying the purity of injection streams (Gale, 2009; Ellis *et al.*, 2010).

There are excessive costs associated with capture and purification technologies, thus, the knowledge of the consequences of impurities in the CO_2 gas stream during CCS is of immense importance as it may lead to significant cost reductions in the CCS process (Knauss *et al.*, 2005; Gaus, 2010; Wang *et al.*, 2011, 2012; Ziabakhsh-Ganji and Kooi, 2014; Pearce *et al.*, 2015). In a typical amine capture system, a 13% reduction in capital costs and a corresponding 8% reduction on annual expenses has been indicated as the likely result of eliminating only the SO_2 scrubbers from the CCS retrofit process (Glezakou *et al.*, 2012; Pearce *et al.*, 2015).

As a significantly influential impurity, SO_2 is of particular interest. With a higher density than CO_2, SO_2 gas is reported to be capable of increasing the storage capacity, permeability, local porosity, injectivity as well as the self-sealing capability of the cap rock in geological formations (Wang *et al.*, 2011, 2012; Pearce *et al.*, 2015). Comparing different separation technologies, Lee *et al.* (2009), estimates a range of 21 (parts per million by weight) ppmw to

579 ppmw SO_2 in the captured CO_2 gas stream from a pulverised coal fired power plant and these concentrations correspond to those reported by the IEA (IEA, 2011). However, in oxy-fuel combustion plants, NO_x and SO_2 are considered to be the main polluting impurities, with SO_2 concentrations spiralling up to 6 times that of an equivalent air-coal combustion plant without desulphurisation (Liu and Shao, 2010; Wang *et al.*, 2012; Pearce *et al.*, 2015). Pearce *et al.* (2015), reports a range of up to 1% SO_2 concentration from oxyfuel captured CO_2 streams.

1.2 Motivation

The understanding of reservoir rock microstructure is important for the extrapolation of storage capacity, transport efficiency and long-term gas retention during sequestration (Credoz *et al.*, 2009; Dai *et al.*, 2020; Mavhengere *et al.*, 2021). Various researchers have reported changes in the structural and physical properties of the reservoir rocks that have been exposed to CO_2 gas under simulated geological sequestration conditions over time (Goodman *et al.*, 2005; Mavhengere *et al.*, 2015; Pearce *et al.*, 2015). The changes in the physical and structural characteristics of the geological materials are believed to have far-reaching effects on the CO_2 adsorption and mineral trapping behaviour and in turn influence the CO_2 injectivity and storage capacity (Bachu *et al.*, 2007; Pearce *et al.*, 2015).

It is important to understand the physical and micro-structural changes occurring in geological materials accompanying their exposure to the injected CO_2 gas streams. Experimental analyses on site specific reservoir and seal rocks provides a valuable role in the prediction of long-term CO_2 storage effects (Pearce *et al.*, 2015). Studies have reported changes in surface area, porosity and permeability of shales and sandstones over varying timelines (Lahann *et al.*, 2013; Campos *et al.*, 2015; Jiang *et al.*, 2016; Yin *et al.*, 2016; Pan *et al.*, 2018; Wu *et al.*, 2019). The resulting effects on the rock characteristics and long-term trapping mechanisms due to exposure to CO_2 and contaminants (SO_2) could lead to incorrect predictions and complications in evaluating the long-term effects of CO_2 storage (Goodman *et al.*, 2005; Yang *et al.*, 2011; Mavhengere *et al.*, 2015, 2021; Pearce *et al.*, 2015).

According to Hsieh *et al.* (2017), reservoir and caprock stability plays a significant role in determining the effectiveness of a saline aquifer as a CO_2 storage option. The mineral alterations that could take place in the sedimentary basins stand to pose a threat to the overlying

caprock and near wellbore areas during injection (Hangx *et al.*, 2013). The effect of CO_2 injection on carbonate-bearing sandstones has not been studied extensively to date (Hangx *et al.*, 2013). Sedimentary basins present extremely diverse and complex fluid components, mineral compositions, and pore structures, motivating the need for further research to establish a comprehensive understanding of CO_2 behaviour in the respective reservoirs (Xu *et al.*, 2007; Hangx *et al.*, 2013). The sequestration of CO_2 by mineral phases has been shown to vary substantially with the rock type, with the identified CO_2 trapping mineral phases also shown to be study area sensitive (Xu *et al.*, 2004; Pearce *et al.*, 2015). Hence, the need for the characterisation and evaluation of potential storage sites for CO_2 sequestration in the various mineral phases (Xu *et al.*, 2007).

Up to 5% co-contaminant gases are reported to be present in CO_2 streams after purification. However, the majority of relevant CO_2 sequestration research has been conducted using pure/food grade CO_2 (Gaus, 2010; Pearce *et al.*, 2015). Greater potential impacts on the geological sinks and cap-rock are posed by the presence of contaminants such as SO_2, and hence these impacts need to be evaluated. Despite the use of reactive transport modelling techniques to predict the co-injection of CO_2 in geological formations (Knauss *et al.*, 2005; Xu *et al.*, 2007; Pearce *et al.*, 2015), limited experimental studies support these predictions (Pearce *et al.*, 2015). Pure minerals have also been used in most of the reported studies, and these have fallen short in the extrapolation to heterogeneous-natural systems. Hence, the experimental analysis on the unique reservoir and seal rock provides a valuable role in the prediction of long-term effects of CCS (Pearce *et al.*, 2015).

1.3 Problem Statement

A long-term experimental study of the effects of CO_2 storage on the South Africa's Zululand Basin rocks has not yet been reported. With the current plans to undertake pilot test injection in the country, such a study is expected to provide valuable insight to the effects of CO_2 storage in sandstone samples. The extension of the experimental analysis to the influence of SO_2 provides a crucial and novel analysis of South Africa's prospective CCS basins.

Most studies report on CO_2 exposure experiments conducted over short adsorption periods (of up to 2 weeks) at low pressures (<60 bar) (Sakurovs *et al.*, 2007; Romanov and Soong, 2008;

Perera *et al.,* 2011). In order to predict the long-term effects of CO_2 storage in sedimentary basins, the need to develop an understanding of rock-CO_2-water interactions under simulated geological conditions as well as rock-CO_2-SO_2-water interactions and their effects on the formation structure and properties (Larsen, 2004) becomes crucial.

This research intends to address the knowledge gaps in understanding CO_2 storage in South-African sandstone extracted from the Zululand Basin, and the impact of SO_2 as an impurity in the CO_2 stream.

1.4 Research Questions

This study aims to address the following questions:

1. Are the physical and chemical properties of the Zululand Basin sandstone core samples affected by the exposure to typical sequestration conditions using CO_2-water and CO_2-SO_2-water gas mixtures?
2. What are the physical and chemical interactions taking place between the pure and mixed gas streams and the geological materials under CO_2 sequestration conditions?
3. What are the differences in the physical and chemical interactions taking place in each of the samples as a function of their sample composition and gas mixtures used for treatment?
4. What implications do these interactions infer on the long-term storage of such gas streams in the target storage locations?

1.5 Research Aim and Objectives

The current study aims to investigate the long-term effects of CO_2-water and CO_2-SO_2-water gas mixtures on the structure and properties of the sandstone samples at supercritical pressures, providing more insight into the crucial rock-gas interactions relative to CO_2 storage. In order to achieve this, five Zululand Basin core samples were selected for analyses. The following research objectives were undertaken:

i. To determine the physical and structural characteristics of the Zululand Basin core samples. This objective was fulfilled by conducting the following advanced characterisation analyses on each of the Zululand Basin sandstone core samples:
    i. X-Ray diffraction analysis (XRD)
    ii. Fourier-Transform Infrared (FTIR) Spectroscopy
    iii. Low Pressure Gas Adsorption (LPGA) analysis using CO_2 and nitrogen (N_2) gases.

ii. To design and execute an experimental procedure for simulating CO_2 storage conditions pertinent to the sandstone samples for a period of one and two months under supercritical conditions using high pressure reactors and the following concentrations of the CO_2 feed stream:
    a. 100 % CO_2
    b. 1 % SO_2, balance made up of CO_2 (CO_2-SO_2) in line with maximum SO2 concentrations from captured streams (Pearce *et al.*, 2015).

iii. To determine the physical and structural characteristics of the sandstone samples after CO_2 storage experiments using characterisation techniques highlighted in (i).

iv. Compare the physical, chemical and structural properties of the parent (untreated) samples to post CO_2 storage (treated) samples and determine:
    i. Whether or not there are any changes in the characteristics of the sandstone samples after treatment under sequestration conditions.
    ii. Whether or not the presence of SO_2 in the CO_2 stream affects the structural and physical characteristics of each sample under supercritical conditions.

iii. Whether or not the presence of SO_2 in the CO_2 stream affects the CO_2-water-rock interactions taking place during treatment.

Such a comprehensive approach to the influence of SO_2 in CCS has not previously been extended to South African sedimentary basins. South Africa requires a significant amount of research into CCS, and this study provides some vital information that will assist not only in storage capacity estimations, but also in the efforts to predict the long-term effects of CO_2 storage in the Zululand sedimentary basins.

1.6 Study Area

The Zululand Basin (South Africa) is one of the two onshore sedimentary basins earmarked for the South African Centre for Carbon Capture and Storage (SACCCS)'s Pilot CO_2 Storage Project (PCSP) in the near future (Chabangu *et al.*, 2014a). With sediment thickness of up to 2000 km and an onshore area of up to 7 500 km^2, the Zululand Basin contains an appreciable sedimentary package. The Basin's Cretaceous sandstones have been demonstrated to be porous and suitable for CO_2 storage (Viljoen *et al.*, 2010). Its location is indicated in Figure 1.1 amongst other sedimentary basins in the region.

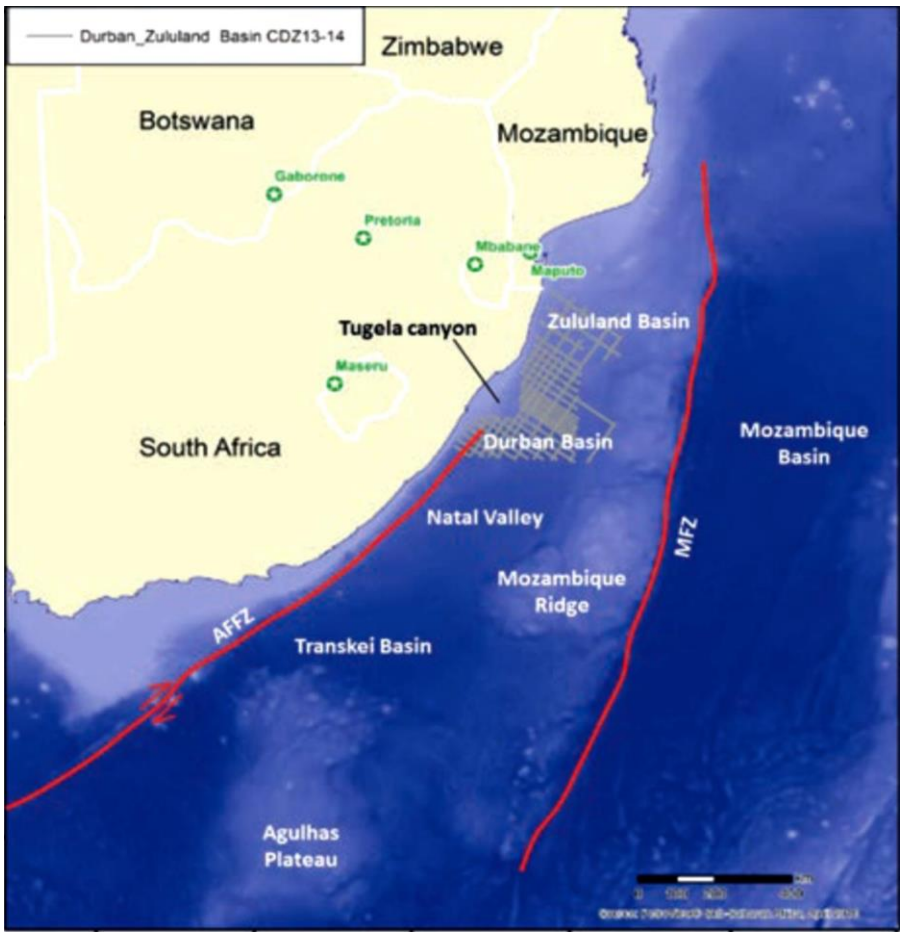

Figure 1.1: Presentation of the Zululand Basin location amongst other sedimentary basins in the region. (Bhattacharya and Duval, 2016).

The Zululand Basin lithologies are made up of three formations, namely: the St Lucia, Mzinene and Makatini Formations (Chabangu *et al.*, 2014a). The sandstone is made up of interbedded sandstone and siltstone (Chabangu *et al.*, 2014a). The exploration boreholes studied consist of layers of fine-grained sandstones and siltstones that form potential seals and reservoirs in the Basin (Viljoen *et al.*, 2010; Chabangu *et al.*, 2014a).

1.7 Thesis Layout

The thesis is presented as seven (7) chapters. The chapters are detailed in the following manner:

- Chapter 2: Provides a detailed background review on the effects of exposing geological materials to CO_2 sequestration conditions.
- Chapter 3: Gives a summary of the methodology, sample preparation and characterization techniques applied are presented. The novel experimental technique used to simulate CO_2 storage using the different gas mixtures is also presented.
- Chapter 4: Presents the characterisation results of the untreated samples.
- Chapter 5: Details the CO_2 treated sample characterisation results.
- Chapter 6: Presents the CO_2-SO_2 treated sample characterisation results.
- Chapter 7: Focuses on the discussion and conclusion of the research and its relevance to CCS in South Africa's Zululand Basin.

1.8 Contribution to knowledge

This study's contribution to knowledge through the published and peer reviewed journal papers and conference presentations. These are listed as follows:

1. Published Article 1: Mavhengere, P., Maphala, T., Wagner, N., 2015. Physical and structural effects of carbon dioxide storage on vitrinite-rich coal particles under subcritical and supercritical conditions. International Journal of Coal Geology 150–151, 1–6.
2. Published Article 2: Mavhengere, P., Wagner, N., Malumbazo, N., 2021. The effects of long-term supercritical CO_2 exposure on Zululand Basin core samples. Energy 220, 119806.
3. Conference Presentation: The Effects of SO_2 in CO_2 Streams on the Physical and Structural Properties of Zululand Basin Core Samples Pertaining to Geological CO_2 Sequestration. Fossil Fuel Foundation Conference In Sustainable Development of

Southern Africa's Energy Resources 29 – 30 November 2017, University Of Johannesburg.

4. Published Article 3: P. Mavhengere, N. Wagner, N. Malumbazo, 2022 Influences of SO_2 contamination in long term supercritical CO_2 treatment on the physical and structural characteristics of the Zululand Basin caprock and reservoir core samples. Journal of Petroleum Science and Engineering, https://doi.org/10.1016/j.petrol.2022.110554.

2 CHAPTER 2: LITERATURE REVIEW

The separation of the CO_2 gas stream from the industrial flue gases and its long-term storage in suitable geological formations describes the process of CCS (Irfan *et al.*, 2018). There is still a limited understanding of the gas-solid interactions occurring during the storage of CO_2 in sedimentary basins (Larsen, 2004; Mirzaeian and Hall, 2006; Viljoen *et al.*, 2010; Mavhengere *et al.*, 2015), particularly with regards to long term implications. The physical and structural properties of reservoir rocks and formation water have been shown to change with exposure to CO_2 under geological sequestration conditions over time (Goodman *et al.*, 2005; Mavhengere *et al.*, 2015; Pearce *et al.*, 2015). This implies that exposure to CO_2 gas may significantly affect the adsorption properties and characteristics of the geological materials in the long term (Yang *et al.*, 2011; Mavhengere *et al.*, 2015, 2021). Of even greater importance is the need for the definition of the rock-gas interactions involving impurities contained in typical captured CO_2 gas streams.

Following on and in order to address the aims and objectives of the study, this chapter provides information on the following:

1. An overview of the potential geological sinks available for sequestration globally and in South Africa. The section includes a justification of the selection of the Zululand Basin core samples for this study.
2. A background assessment on the various CO_2 trapping mechanisms in sedimentary basins.
3. An outline of the effects of CCS on the structural and physical properties of sandstones.
4. A discussion on the influence of SO_2 on rock and aquifer storage potential and capacity.

2.1 Potential Geological Sinks

Bachu (2002), describes geological sequestration of CO_2 as an immediately available and technologically feasible measure for mitigating CO_2 emissions into the atmosphere. The deciding factor in screening out unsafe geological sinks is the elimination of the potential for CO_2 release and migration (Bachu, 2002, 2008). Potential geological sinks comprise of oil and

gas reservoirs (disused or in operation through enhanced oil recovery methods), unmineable coal seams, saline aquifers, and salt caverns (Bachu, 2000, 2008; Herzog and Golomb, 2004). The global storage capacity in saline aquifers is estimated at a range between 10 000 to 200 000 Gt of CO_2 (Bradshaw *et al.*, 2004). The wide range is due to the uncertainty in the technical assessments as a result of limited data availability on the respective aquifers (Bradshaw *et al.*, 2004). According to Bachu (2008), potential geological sinks must have the necessary capacity, injectivity and ability to confine the CO_2 by impeding lateral migration and vertical leakage to the environment. Such capability is mainly observed in oil and gas reservoirs and deep saline aquifers in sedimentary basins (Bachu, 2008). Although a lot has been learnt from various global CO_2 storage pilot projects, it is acknowledged that the geological formations are generally heterogeneous and present varying properties with location (Ahmadinia *et al.*, 2020).

According to Wright *et al.* (2009), only 4 large scale (> 1 million metric tonnes per annum of CO_2) CO_2 sequestration projects have been established. These are the Weyburn-Midale (Canada), the In Salah (Algeria), the Sleipner and the Snøhvit (Norway) (Wright *et al.*, 2009). The Weyburn-Midale presents an enhanced oil recovery sequestration process whilst the rest of the storage sites are sandstone reservoirs. The Sleipner and In Salah were the first two storage sites to be established globally and have sequestered the highest volumes of CO_2 to date (Wright *et al.*, 2009; Ahmadinia *et al.*, 2020; Cao *et al.*, 2021). Initiated in 1996, the Sleipner project was the first commercial scale CO_2 storage project globally (Torp and Gale, 2004; Ghosh *et al.*, 2015; Ahmadinia *et al.*, 2020). The storage site is an offshore saline aquifer at depths between 800 m to 1000 m beneath the sea, sequestering CO_2 captured from a natural gas processing field in close vicinity to the facility (Arts *et al.*, 2004; Head *et al.*, 2004; Ahmadinia *et al.*, 2020). The In Salah, sequestration is carried out into a carboniferous sandstone reservoir measuring 20-25 m in thickness at 1900 m depth below ground surface, the operation was established in 2004 (Wright *et al.*, 2009; Cao *et al.*, 2021).

2.1.1 **Potential Geological Sinks in South Africa**

South Africa boasts of an estimated 150 Gt of CO_2 geological storage capacity, with only 2% being located onshore (Viljoen *et al.*, 2010). The 98% potential capacity represents offshore Mesozoic basins (the Outeniqua and the Orange offshore basins). Onshore basins are associated with lower drilling costs and the feasibility to create 3D seismic data for prospecting and

monitoring as compared to offshore basins (Viljoen *et al.*, 2010). These offshore storage basins, as potential CO_2 storage sites, are believed to compete with oil and gas resources that the country plans to exploit in the future (Viljoen *et al.*, 2010). Saline aquifers contribute 0.86 Gt of potential onshore storage capacity (Viljoen *et al.*, 2010). Figure 2.1 presents the locations of potential saline aquifer geological sinks in South Africa. The onshore storage capacity that makes up the remaining 2% represents an equal split between unmineable coal seams and the Zululand and Algoa Basins (Chabangu *et al.*, 2014b). A focus on the onshore basins for potential CO_2 injection is derived from the scope and funding limitations in the country (Chabangu *et al.*, 2014b).

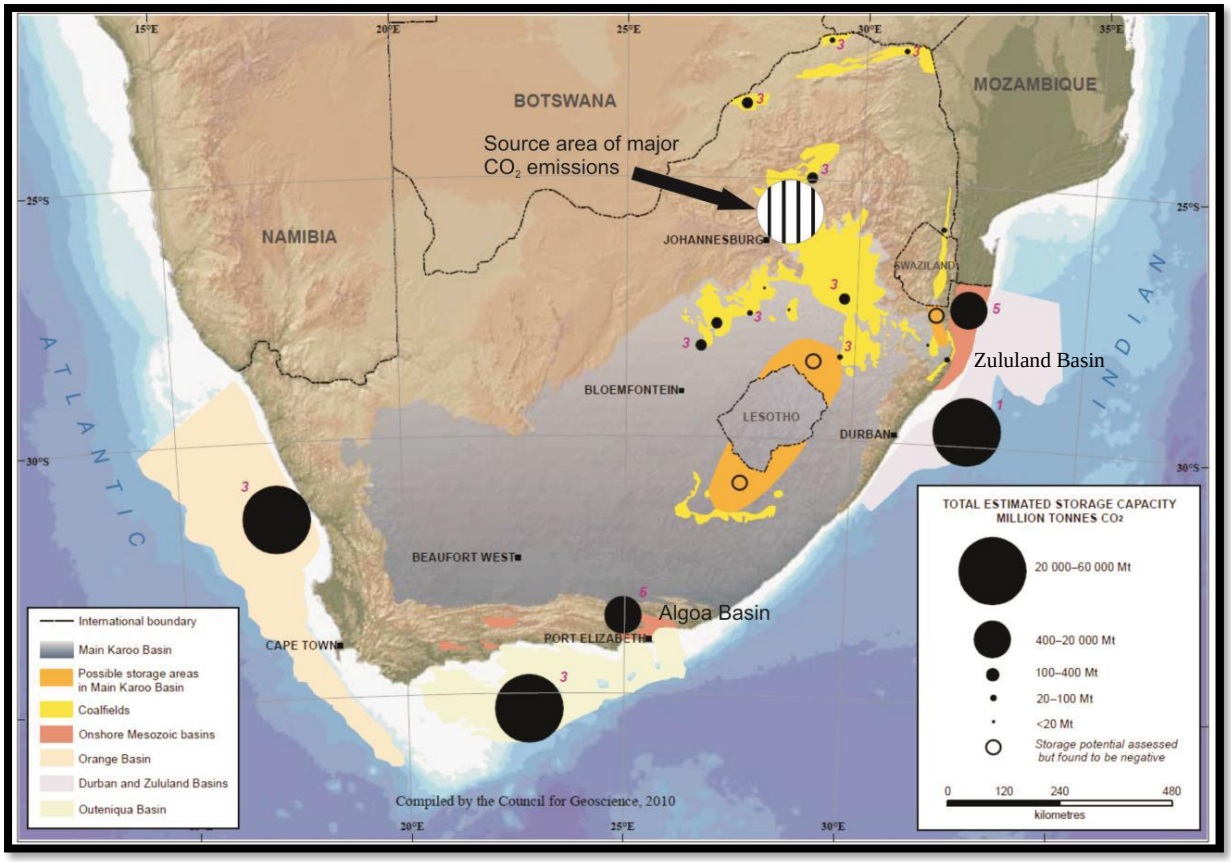

Figure 2.1: Potential geological sinks in deep saline formations in South Africa (Chabangu *et al.*, 2014a)

The onshore Zululand and Algoa Basins are currently earmarked for the SACCCS PCSP project; unfortunately, the project has experienced significant delays. SACCCS was established for the purpose of understanding the technical potential of CCS in South Africa and addressing

the uncertainty around CO_2 storage by the South African government in conjunction with local and international industry (Chabangu *et al.*, 2014a). The centre aims to conduct a PCSP project to store up to 50 000 Gt of CO_2 (Chabangu *et al.*, 2014a). Two saline aquifers /sandstone packages have been identified for potential CO_2 storage (Viljoen *et al.*, 2010; Chabangu *et al.*, 2014a). These are the lowermost Aptian aged sandstone and the Cenomanian sandstone located on the onshore Zululand Basin. The basin is located 400 km from South Africa's major sources of emissions from coal fired power plants (Viljoen *et al.*, 2010; Chabangu *et al.*, 2014a). No literature relating the long-term effects of CO_2 storage on the structural and physical characteristics of the Zululand sandstones has yet been reported.

The Aptian sandstone occurs as a sequence of sandstone and siltstone in the presence of secondary claystone at depths between 1200-1800 m over an area of 1680 km^2 (Chabangu *et al.*, 2014a). A 20 - 200 m thick package of interbedded sandstone and siltstone at depths between 50 and 900 m represents the Cenomanian aged sandstone of the Zululand Basin. The Cenomanian Sandstone covers an area extent of 352 km^2 at depths between 23 m and 1035 m and forms part of the Mzinene and St Lucia Formations. Inadequate and reasonably poor data availability for the Algoa Basin has been reported (Viljoen *et al.*, 2010); the need for new data has been cited in order to confirm its potential capacity for CO_2 storage (Viljoen *et al.*, 2010; Chabangu *et al.*, 2014a). The consideration of the Algoa Basin is however beyond the scope of this project.

2.2 CO_2 trapping mechanisms in sedimentary basins.

In saline aquifers /sedimentary basins (i.e., sandstones and carbonate reservoirs), various CO_2 trapping mechanisms apply. These are namely (Bachu, 2007; Hermanrud *et al.*, 2009; Zhang *et al.*, 2009; Aydin *et al.*, 2010; De Silva and Ranjith, 2012; Cui *et al.*, 2017).

1. solubility/ionic trapping,
2. mineral trapping,
3. structural/stratigraphic trapping,
4. residual gas trapping,
5. hydrodynamic trapping.

De Silva and Ranjith (2012) provides a detailed description these trapping mechanisms and further describes the CO_2 storage capacity evaluation methods pertinent to each of them. These evaluations are discussed further in the subsections that follow.

2.2.1 **Solubility Trapping**

Solubility trapping takes place when CO_2 dissolves in formation water, leading to reactions with minerals in the host formation (Golding *et al.*, 2011; Jiang, 2011). Gilfillan *et al.* (2009) reports that solubility trapping is the dominant trapping mechanism in over 80% of the CO_2 rich gas fields. De Silva and Ranjith (2012) describes the mechanism as a progressive and time dependent process driven by CO_2 diffusion, convection, and dispersion in the aquifer. The rate of solubility trapping is highly dependent on the volume of CO_2 stream coming into contact with formation water (CO_2 unsaturated) in the rock (De Silva and Ranjith, 2012). The composition of the CO_2 stream is also expected to influence the resulting trapping mechanisms in a formation. The increase in density as a function of CO_2 dissolution in the formation water allows the trapped CO_2 to sink to the bottom of the aquifer eliminating risks of leakage (De Silva and Ranjith, 2012; Li and Jiang, 2014). Once CO_2 migration in the aquifer stops, the dissolution process occurs at a much slower rate as it becomes dependant on the CO_2 concentration gradient (De Silva and Ranjith, 2012). According to De Silva and Ranjith (2012), the theoretical CO_2 capacity (M_{CO_2t}) is evaluated as a function of the density difference between the initial stage and the saturation stage $\Delta(\rho X^{CO_2})$, the volume of the aquifer (V) and its porosity ($\emptyset$) (Equation (1)).

$$M_{CO_2t} = \int \emptyset \ \Delta(\rho X^{CO_2}) dV \ldots\ldots\ldots\ldots\ldots\ldots\ldots\ldots\ldots\ldots\ldots\ldots\ldots\ldots (1)$$

Li and Jiang. (2014) studied the effects of N_2 and SO_2 impurities on the CO_2 solubility trapping mechanisms during sequestration and reported a reduction in the CO_2 dissolution rate in the presence of N_2. Impurities like SO_2 were found to enhance solubility trapping whilst N_2 impeded it (Li and Jiang, 2014).

2.2.2 **Mineral Trapping**

Mineral trapping of CO_2 arises from the reaction of the gas in water to form carbonic acid which further reacts with aquifer rock minerals leading to the precipitation of carbonate minerals (Xu *et al.*, 2004; De Silva and Ranjith, 2012). The chemical composition of the formation waters, rock matrix, rock formation-water contact surface area and the pressure and temperature conditions in the aquifer all drive the mineral trapping mechanism in sedimentary basins (Gunter *et al.*, 2004; Gilfillan *et al.*, 2009). Variations in mineral composition and rock type introduce considerable variations in the mineral trapping mechanisms taking place in an aquifer (De Silva and Ranjith, 2012). The precipitation of carbonates leads to a reduction in the porosity of the aquifer, in turn reducing its injectivity and permeability (Xu *et al.*, 2004). The evaluation of the CO_2 mineral trapping capacity can only be conducted using site scale numerical simulations to estimate the capacity that can be stored in the reservoir and the time frame involved (Xu *et al.*, 2004; De Silva and Ranjith, 2012). The mineral trapping CO_2 sequestration method presents the attractive opportunity to immobilize the CO_2 for exceptionally long periods of time (Bachu *et al.*, 2007). The process has been shown to enhance solubility trapping through the dissolution of alkaline aluminosilicates increasing the concentration of soluble carbonates in solution (Xu *et al.*, 2004). Siliclastic reservoirs generally present greater mineral trapping potential than carbonate reservoirs (Gilfillan *et al.*, 2009).

2.2.3 **Structural Trapping**

Structural trapping is described by Hermanrud *et al.* (2009) as trapping beneath a seal/caprock, this is highly dependent on a stratigraphic trap similar to those observed in mobile hydrocarbon accumulations (oil/gas reservoirs), and the most dominant form of trapping in the short term. Supercritical CO_2 ($_{sc}CO_2$) percolates through porous rocks due to its higher buoyancy than other liquids until it is trapped by impermeable caprock (De Silva and Ranjith, 2012). Bachu *et al.* (2007) evaluates the volume of the CO_2 trapped (V_{CO_2t}) as outlined in Equation (2).

$$V_{CO_2t} = Vs_{trap}\emptyset(1 - S_w) \dots\dots\dots\dots\dots\dots\dots\dots\dots\dots\dots\dots\dots (2)$$

Where $Vs_{trap}$is the volume of the available trap, $\emptyset$ is the porosity of the rock and S_w is the water saturation in the aquifer. In this scenario, the injection pressure must be lower than the

maximum bottom hole injection pressure to eliminate rock fracturing (Bachu *et al.*, 2007; De Silva and Ranjith, 2012).

2.2.4 **Residual Gas Trapping**

This mechanism plays a significant role in low permeability saline aquifers (Nghiem *et al.*, 2009). This process takes place when the CO_2 plume penetrates porous rocks, small quantities of CO_2 are then trapped into pore spaces leaving behind a trail of residual static CO_2 in the rock structure (Bachu, 2008; De Silva and Ranjith, 2012). It is generally acknowledged that this trapping mechanism largely takes place after injection has stopped (Bachu *et al.*, 1994). The volume of CO_2 stored is dependent on the porosity, CO_2 saturation and the volume of rock previously saturated by CO_2 (De Silva and Ranjith, 2012).

2.2.5 **Hydrodynamic Trapping**

Hydrodynamic trapping is described a combination of the various trapping mechanisms taking place concurrently in the rock at varying scales (De Silva and Ranjith, 2012). This mechanism has been shown to enhance potential for mineral trapping (Bachu *et al.*, 1994). According to Pruess and García (2002), hydrodynamic trapping presents propensity for CO_2 leakage through imperfect confinement. Reactive transport modelling and experimentation have generally been used to evaluate the effects of hydrodynamic trapping in aquifers (Lucier and Zoback, 2008).

The various time frames associated with the different trapping mechanisms need to be considered when evaluating storage capacity (De Silva and Ranjith, 2012). The structural and residual trapping mechanisms are known to play a crucial role in the first decades of storage (Al-Yaseri *et al.*, 2016). According to Irfan *et al.* (2018), the dissolution and mineral trapping mechanisms can continue for centuries. The rock type and hydrothermal conditions associated with a particular aquifer play a vital role in the development of the residual trapping mechanisms during CO_2 storage (Valle *et al.*, 2018). The mineral components and properties contained in a geological formation influence its CO_2 storage capability. The storage temperature, pressure and time have also been reported to influence the physical and structural characteristics of geological materials (Okamoto *et al.*, 2005; Dai *et al.*, 2020). The variation in the microstructure and composition of geological formations before and after CO_2 exposure also plays a significant role in CO_2 sequestration (Mavhengere *et al.*, 2021).

2.3 Effects of CCS on the Physical and Structural Properties of Sandstones

Experimental analyses on site specific reservoir and seal rocks provides a valuable role in the prediction of long-term CO_2 storage effects (Pearce *et al.*, 2015). For example, changes in surface area, porosity and permeability of shales have been reported by various researchers (Lahann *et al.*, 2013; Yin *et al.*, 2016; Pan *et al.*, 2018). Porosity and surface area are reported to increase with immersion pressure and time (Jiang *et al.*, 2016; Pan *et al.*, 2018). Wu *et al.* (2019) exposed three sandstone samples to supercritical CO_2 and brine and reported measurable impacts on the sample porosities and permeabilities; variable dissolution and reprecipitation of different mineral groups was also reported. Campos *et al.* (2015) reported drastic modifications of sandstone pore structures from the Utrillas Formation (Spain) after treatment with $_{sc}CO_2$ for two months, implying significant impacts on the resulting storage capacities.

Numerous studies are reported on the pore characterisation of sandstone reservoirs and their correlations with permeability, porosity, and pore size distribution (Rezaee *et al.*, 2012; Xi *et al.*, 2016; Qiao *et al.*, 2020). Although critical to storage and percolation capacities, comprehensive pore structure characterization of sandstones is quite challenging (Xiao *et al.*, 2017; Qiao *et al.*, 2020). This is mainly due to the distinctive resolution and specific limitations of each experimental technique used to evaluate the pore structure (Clarkson *et al.*, 2012; Anovitz and Cole, 2015; Zhao *et al.*, 2016). Techniques such as scanning electron microscopy (SEM), low temperature CO_2 and N_2 adsorption, and nuclear magnetic resonance (NMR) are currently employed for pore size distribution and pore geometries analyses (Clarkson *et al.*, 2012; Zhao *et al.*, 2016; Xiao *et al.*, 2017; Qiao *et al.*, 2020). SEM observations are able to assess pore morphology, genesis, and size, but they cannot provide detailed quantitative pore structure analyses (Zhang, 2017; Qiao *et al.*, 2020). NMR requires calibration with other experimental results to determine the pore size distribution of samples by evaluating the relaxation time of hydrogen nuclei of fluids in the pores and throats (Qiao *et al.*, 2020). Low temperature CO_2 and N_2 adsorption only allows for the evaluation of pore sizes under 50 nm.

The influence of pores under 1 µm on sandstone reservoir permeability and storage capacity is reported to vary in relation to sample permeability and carbon content (Xi *et al.*, 2016; Xiao *et al.*, 2017; Wu *et al.*, 2019; Qiao *et al.*, 2020). Qiao *et al.* (2020) studied thirteen sandstone samples from the Jungaar Basin and found that pores under 1 µm contributed up to 70% of the

full range of the pore size distribution (PSD). Xiao *et al.* (2017) describes these pores as consisting of clay-associated pores and intraparticle dissolution pores that contribute both to percolation, storage, and specific surface area. Although pores above 1,5 µm may determine the storage capacity of the reservoirs, the pores under 1 µm are reported to present negative influence on the storage capacity that should be considered in storage capacity evaluations (Qiao *et al.*, 2020; Xiao *et al.*, 2017). Qiao *et al.* (2020) also highlight the inconsistencies in pore classifications presented in literature in relation to sandstone reservoirs, demonstrating the need for more extensive research in the area.

According to Řimnáčová *et al.* (2020), micropores, mesopores and macropores can occur in mineral matter, mainly in clays and quartz minerals. Interparticle pores have been found to be more common than intraparticle pores in inorganic matter (Loucks *et al.*, 2012; Zhang, 2012; Řimnáčová *et al.*, 2020). Weishauptová *et al.* (2017) describes typical mesopores and macropores as interparticle pores in big irregular grains of calcite and plate aggregates of illite. Intraparticle pores in the shape of various cavities can be represented within bigger quartz and calcite particles (Weishauptová *et al.*, 2017). According to Řimnáčová *et al.* (2020) intraparticle mesopores are formed by the dissolution of big calcite grains and some spaces in smaller clay mineral aggregates. Macropore formation as a result of mineral dissolution is also well reported in literature (Fishman *et al.*, 2012; Yang, 2016; Řimnáčová *et al.*, 2020).

The sorption capacity of sedimentary rocks is related to their micropore content (Řimnáčová *et al.*, 2020). The microporous structure has mainly been attributed to the organic components of the rock and the interlayer span in clay minerals (Tan *et al.*, 2014; Řimnáčová *et al.*, 2020). Clay minerals have been classified as mainly mesoporous and macroporous (Chalmers *et al.*, 2012; Curtis *et al.*, 2012). Ross and Bustin (2008) however found that clay minerals contain a notable amount of micropores and determined the micropore volumes for the individual clay minerals. Guo *et al.* (2014) to the contrary, reported little relative micropore volume contribution from clay minerals. Micropores are known to contribute to the sorption capacity of the CO_2 in geological media (Řimnáčová *et al.*, 2020).

The presence of micropores, mesopores and macropores in the Zululand Basin core samples will be investigated using LPGA in the current study. For micropores with pore diameters in

the range of 0.35-1.5 nm, CO_2 adsorption at 273 K is suitable due to its smaller molecular diameter and superior diffusion ability (Pan *et al.*, 2018). The use of CO_2 adsorption for micropore structural characterisation has been reported in coal studies (Marsh, 1987; Şenel *et al.*, 2001; Okolo *et al.*, 2015), and the method has also proven useful in the characterisation of shales and non-carbon materials (Pan *et al.*, 2018). In accordance with the International Union of Pure and Applied Chemistry (IUPAC) classification (Thommes *et al.*, 2015), the CO_2 adsorption analyses will therefore be used to evaluate changes in the sample's micropores (d<1.5 nm (15 Å)). Nitrogen adsorption at 77 K effectively evaluates the characteristics of pores between 1.7 and 200 nm in diameter (Pan *et al.*, 2018). The N_2 adsorption analyses will similarly be used to evaluate changes in the mesopores (2 nm (20 Å) <d<50 nm (500 Å)) and macropores (d>50 nm (500 Å)) (Thommes *et al.*, 2015; Yin *et al.*, 2016).

2.4 Influence of SO_2 in CO_2 storage.

Despite the presence of up to 5% co-contaminant gases in captured CO_2 streams, the majority of the reported water-rock interaction laboratory-based studies related to CCS use pure/food grade CO_2 (Pearce *et al.*, 2015). CO_2 at supercritical conditions dissolves in formation waters, forming weak carbonic acid which results in mineral dissolution and the release of divalent cations (Xu *et al.*, 2005; Gaus, 2010). As time progresses, mineral trapping of CO_2 can occur through the precipitation of carbonates, with potential changes in porosity and permeability of the reservoir (Pearce *et al.*, 2015).

Co-contaminant gases like SO_2 are suggested to significantly influence the physical and chemical properties of the reservoir rock (Xu *et al.*, 2007; Wang *et al.*, 2012; Pearce *et al.*, 2015). CO_2 reacts with water to form carbonic acids, whereas SO_2 in water forms much stronger acids (H_2SO_3 and H_2SO_4); with greater implications on the reservoir rock and geological materials under sequestration conditions (Knauss *et al.*, 2005; Xu *et al.*, 2007; Crandell *et al.*, 2010; Ellis *et al.*, 2010; Pearce *et al.*, 2015). Wang *et al.* (2012) indicate potential benefits of SO_2 in the CO_2 stream such as increased local porosity and permeability in the near well bore which could lead to an increase in injectivity.

Xu *et al.* (2005) report on the reactive transport modelling of CO_2 with SO_2; their models predict enhanced dissolution and porosity coupled with the precipitation of carbonates and

anhydrite and alunite. Mineral trapping potential was also predicted to be greater in SO_2 contaminated CO_2 streams than in pure CO_2 streams. Numerical simulations conducted by Li and Jiang (2014) indicated that SO_2 would lead to enhanced solubility trapping and presented more significant effects in comparison to other impurities like N_2 at similar concentrations. However, very few studies validate such findings using 1% SO_2 concentration in CO_2 gas mixture (Pearce *et al.*, 2015). Laboratory analysis on the particular reservoir and seal rocks have been shown to contribute crucial information towards the prediction and modelling of the long-term effects of CO_2 sequestration (Pearce *et al.*, 2015).

2.5 Chapter Summary

The potential geological sinks in South Africa have been described in this chapter. The two onshore sedimentary basins (Zululand and Algoa basins) are currently undergoing further evaluation as potential storage locations for the SACCCS PCSP. The Algoa Basin has been cited to lack adequate exploration data and further analysis has been recommended. The availability of data in the Zululand Basin has made it possible to include it in the proposed study. The Zululand Basin's prospects are about 57 million tonnes effective capacity of CO_2. The basin is located 400 km from South Africa's major sources of emissions from coal fired power plants (Viljoen *et al.*, 2010; Chabangu *et al.*, 2014a). No literature relating the long-term effects of CO_2 storage on the structural and physical characteristics of the Zululand sandstones has yet been reported.

It is important to understand the physical and micro-structural changes occurring in geological materials accompanying their exposure to the injected CO_2 streams. The resulting effects on the rock characteristics and long-term trapping mechanisms due to exposure to CO_2 and contaminants (SO_2) could lead to incorrect predictions and complications in evaluating the long-term effects of CO_2 storage (Yang *et al.*, 2011; Goodman *et al.*, 2015; Mavhengere *et al.*, 2015; Pearce *et al.*, 2015). There is currently no research reporting on the impact of CO_2 storage on sandstone pores under 1 μm despite the reported influence of these pores on the reservoir's storage capacity.

With up to 5% impurities present in captured CO_2 streams for storage, there is a need to evaluate the effects of particularly influential impurities like SO_2 in CCS. Limited literature is

available on the subject and warrants further research. The available literature has been discussed and outlined in this chapter. Extending the analysis to the influence of SO_2 offers a novel study that could be useful in predicting the long-term effects of CO_2 storage in South Africa's Zululand Basin.

3 CHAPTER 3: SAMPLE PREPARATION AND METHODS

This chapter outlines the collection, preparation and characterisation methods applied to the sandstone samples. As well as the detailed experimental procedure used to conduct the supercritical (Sc)CO_2-water and supercritical (Sc)CO_2-SO_2-water treatment experiments referred to as CO_2 treatment and CO_2-SO_2 treatment respectively in the current study.

3.1 Research Methodology

The research methodology adopted in this study is summarised Figure 3.1. The approach adopted was to facilitate the determination of a baseline characterisation of each of the samples studied through pre-treatment characterisation techniques. This was to allow for comparison with treated samples post CO_2 exposure to evaluate the changes to the physical, structural, and chemical characteristics of the samples during CO_2 and CO_2-SO_2 treatment.

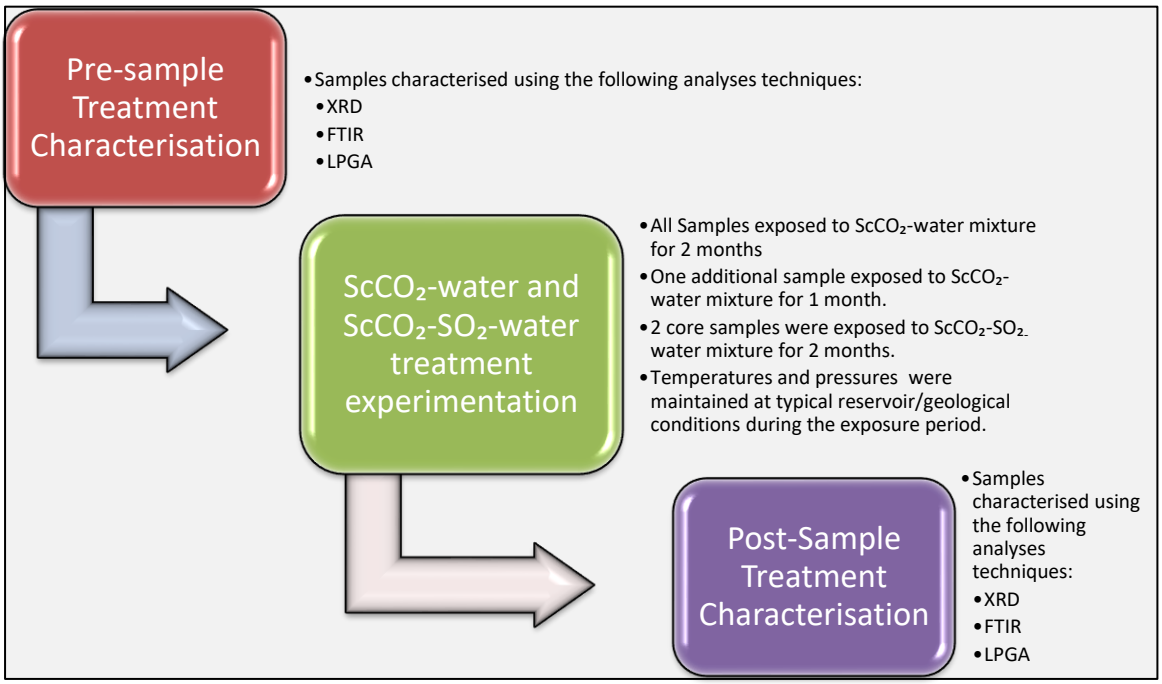

Figure 3.1: Research Methodology

3.2 Samples

3.2.1 Sample Origin

The South African onshore Zululand Basin covers over 7500 km^2 and is an extension of the Mozambique Basin (Gupta *et al.*, 2018). The Aptian and Cenomanian sandstone packages from the Basin have been identified for CO_2 sequestration. Both packages present well developed reservoirs within the Makatini Formation located within the Basin (Chabangu *et al.*, 2014a). According to Chabangu *et al.* (2014a), the Aptian Sandstone mainly consists of coarse to medium grained sandstone and siltstone with subordinate claystone. The sandstone is located at depths of 1200 m to 1800 m over a 1680 km^2 area. The Cenomanian Sandstone covers an aerial extent of 352 km^2 at depths between 23 m and 1035 m. The sandstone is made up of interbedded sandstone and siltstone. The exploration boreholes consist of layers of "fine grained sandstones and siltstones" that form potential seals and reservoirs in the Basin (Gupta *et al.*, 2018).

The locations of the exploration wells drilled in the Zululand Basin are presented in Figure 3.2. Five boreholes were drilled in the 1960's, logged and housed in the Council for Geosciences National Core library in Pretoria (Figure 3.2). These boreholes are part of the SOEKOR boreholes. Although the cores are old, a number of researchers have produced valuable outcomes on the same boreholes over the past few years (Gupta *et al.*, 2004; Linol *et al.*, 2016; Fourie *et al.*, 2017; Hohne *et al.*, 2019; Makiwane, 2019). They are currently the only available boreholes from the Zululand Basin.

Five borehole cores were sampled for use in the present study, namely: ZA, ZC, ZE, ZF and ZG borehole cores. The sandstone samples were selected at depths indicative of the location of the Zululand Basin aquifer and caprock following guidance from Hicks (2016). Table 3.1 describes the sampling depths, stratigraphy horizon and lithology of the selected samples.

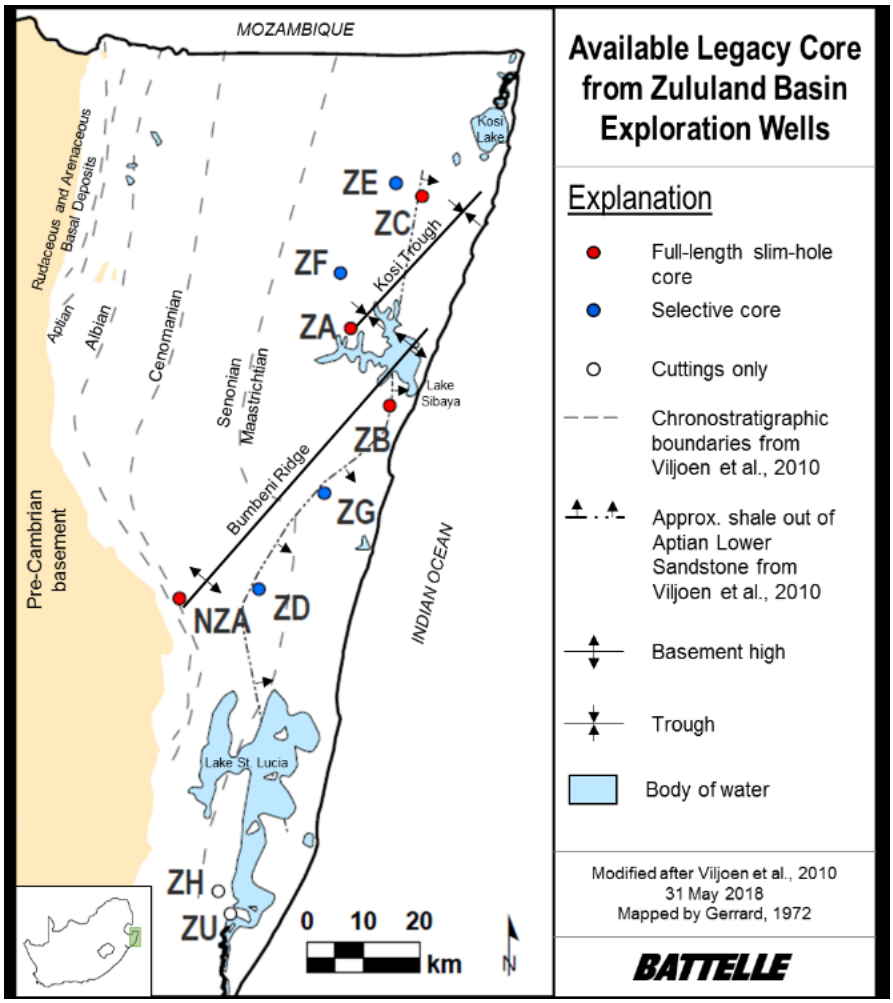

Figure 3.2 Zululand Basin Legacy Core Exploration Wells (Gupta *et al.*, 2018)

Table 3.1: Core Sample Depth, Stratigraphic Horizon and Lithology

Borehole Name	**Sampling Depth (m)**	**Stratigraphic Horizon**	**Lithology**
ZA	691-699	Silt stone lateral seal Aptian sandstone	Sandstone
ZC	691-699	Silt stone lateral seal Aptian sandstone	Siltstone
ZE	1749-1749	Aptian Sandstone	Sandstone
ZF	1740-1745	Aptian Sandstone	Sandstone
ZG	504	Cenomanian Sandstone	Sandstone

3.2.2 **Sample Preparation**

Approximately 100g per sample were crushed in a Retsch centrifugal crusher to -4 mm particle size. Mechanical sample splitting was conducted to obtain representative samples for pre- and post- CO_2 storage experiments/treatment. The selected particle size ensured optimised particle surface area exposure to the $_{sc}CO_2$-water and $_{sc}CO_2$-SO_2-water gas mixture, hence enabling improved reaction rates and minimal reactor pipework and valve blockages. Attempts were made to use $1cm^2$ blocks of sandstone in the treatments. The samples however presented low mechanical strength during exposure as they disintegrated into powder in the surrounding fluid.

3.2.3 **Experimental Set Up**

In order to undertake CO_2 storage experimentation on the selected samples, non-stirred Teflon lined N4766 Parr reactors (Figure 3.3) were employed to simulate geological sequestration conditions. These expensive reactors allow for high pressure tests to be conducted in the presence of water and acid medium. The reactors consist of a 300 ml PTFE lined cylinder vessel with a PTFE head gasket with a split ring closure to prevent sample contamination through vessel corrosion. Attached to the head gasket is a needle valve, pressure gauge, rupture disc, thermocouple, and single inlet dip tube. The maximum working pressure of the units is 207 bar at 350 ºC. Each unit was connected to a heater assembly and a reactor controller which maintained the units at the temperatures and pressures outlined in Table 3.2. The reactors were used in conjunction with an Insco 260D cylinder pump for pressurizing the vessels.

Figure 3.3: N4766 Parr Reactors with controller and heater

Table 3.2: Storage Conditions Applied

Sample	**CO_2 Treatment**	**CO_2-SO_2 Treatment**	**Treatment Temperature (^oC)**	**Treatment Pressure (Bar)**
ZA	X		70±3	175±5
ZC	X	X	70±3	175±5
ZE	X		70±3	175±5
ZF	X		70±3	175±5
ZG	X	X	48±3	100±5

Two types of CO_2 gas storage experiments were conducted on the sandstone core samples. The first experiment involved the use of CO_2 gas at a purity of 99.9%. The second experiment involved the use of a 99% CO_2 and 1% SO_2 gas mixture which was obtained premixed in a gas cylinder supplied by Air Liquide Pty Ltd. Due to equipment failure, only two of the five samples studied underwent storage experiments using both gas mixtures.

All samples were treated with the 99.9% CO_2 gas for up to two months. Samples ZC and ZG, were treated with both 99.9% CO_2 and the mixture of 99% CO_2 and 1% SO_2 gas (Table 3.2) for two months. The temperature and pressure of experiments were selected in accordance with the maximum possible geothermal temperature and pressure that could be obtained in the sample's identified aquifer/sandstone origin. The maximum temperature and pressure related

to the Aptian sandstone and lateral seal was 180 bar and 73 ºC (Viljoen *et al.*, 2010) in line with a maximum depth of 1800 m (Chabangu *et al.*, 2014a). The Cenomanian sandstone parameters were set at 100 bar and 51 ºC in line with the 1035 m maximum depth of the sandstone as reported by Chabangu *et al.* (2014a). The geothermal gradient selected for the borehole cores was 26.6 ºC/Km as reported by Chabangu *et al.* (2014a) at an average surface temperature of 25 ºC (Viljoen *et al.*, 2010). The pressure gradient used was 100 bar/Km, indicating maximum pressures of 100 bars for the Cenomanian sandstone samples and 180 bars for the Aptian sandstone samples. A lower target pressure of 175 bar was adopted in order to remain within 85 % of the maximum 207 bar reactor pressure during the experiment.

A mass of 6 g for all the samples was placed in the reactor along with distilled water at a ratio of 23:1. Nitrogen (N_2) was then flushed through the mixture at low pressure to purge residual air for 48 hours prior to the introduction of CO_2 gas/ CO_2-SO_2 gas mixture. The CO_2 gas or the CO_2-SO_2 gas mixtures were thereafter pumped into the reactors to initiate each of the experiments.

The selected experimental exposure time was 2 months for the present study. According to Yin *et al.* (2016), the first month of experimentation enables the supercritical gas-water and rock mixtures to reach equilibrium and the following month then caters for possible evaluation of long-term effects. The samples were then degassed and collected for physical, structural, and chemical characterisation; these samples are referred to as treated samples. The pre-CO_2 /CO_2-SO_2 treatment samples are referred to as untreated samples. The storage experiments were designed to simulate typical CO_2 injection conditions for the respective cores. This is to facilitate the exposure of the core samples to CCS conditions in order to determine the physical and chemical structure changes imposed by the treatment process.

3.3 Sample Characterization

All samples were characterised pre- and post CO_2/CO_2-SO_2 treatment using XRD, FTIR and LPGA to determine the changes in the rock material as a result of the CO_2/CO_2-SO_2 treatment experiments. These changes are envisaged to influence the CO_2 storage capacity estimations, the CO_2 injection capability and the sealing properties of the caprock/lateral seal.

3.3.1 **X-Ray Diffraction**

Quantitative and qualitative XRD analyses were conducted on the core samples by XRD Analytical and Consulting (Pretoria). The XRD analyses was conducted using a back loading preparation method and analysed with the use on a PANalytical Empyrean diffractometer with PIXcel detector and fixed slits with Fe filtered Co-Kα radiation. The phases in the powder samples were identified using X'Pert Highscore plus software and quantified using the Rietveld method.

XRD has been applied extensively to determine the mineral compositions of inorganic matter in the CCS context (Xu and Van Deventer, 2002; Wollenweber *et al.*, 2010; Rezaee *et al.*, 2012; Wilke, 2012; Richiano *et al.*, 2015; Schmitt *et al.*, 2015; Yin *et al.*, 2016; Dai *et al.*, 2020; Fakher and Imqam, 2020). Changes in mineral phases in the samples can be observed through XRD, allowing for the identification of the geochemical reactions taking place during CO_2/CO_2-SO_2 treatment in the core samples (Wollenweber *et al.*, 2010; Mavhengere *et al.*, 2015; Yin *et al.*, 2016).

3.3.2 **FTIR**

The use of FTIR for surface chemical structure characterisation is well established (Jiang and Xu, 1995; Nakamura *et al.*, 1996; Reig *et al.*, 2002; Guiliano *et al.*, 2007; Chen *et al.*, 2015; Cheng *et al.*, 2020; Chalmers *et al.*, n.d.). A Perkin Elmer Universal Attenuated Total Reflectance (UATR) Spectrum Two FTIR Spectrometer was used to determine the spectra profiles of each of the samples using a spectrum software suite. Diamond crystal UATR FTIR spectroscopy allowed for rapid analyses of the powder samples. The analyses were conducted at the University of Witwatersrand using powder samples of ~1 g each.

3.3.3 **Low Pressure CO_2 and N_2 gases adsorption**

Low pressure gas adsorption (LPGA) has been shown to be an effective method of evaluating the pore structures of geological materials (Clarkson *et al.*, 2012; Pan *et al.*, 2018). The LPGA method using CO_2 and nitrogen (N_2) was executed using a Micrometrics ASAP 2020 surface area and porosity analyser at the North West University, Potchefstroom. Data acquisition was conducted through the use of an ASAP 2020 v 4.0 software package. Samples of ~0.5 g each were degassed under vacuum at a temperature of 90 ºC prior to adsorption.

CO_2 adsorption was used to evaluate the micropore structure. The adsorption isotherms were determined at a temperature of 273 K and a relative pressure range of 0.00 to 0.032. The Dubinin-Radushkecich (D-R), Dubinin-Astakhov (D-A) and BET methods were used for the calculation of the micropore surface areas (Okolo *et al.*, 2015; Pan *et al.*, 2018). The limiting pore volume was determined using the Dubinin-Astakhov (D-A) model (Pan *et al.*, 2018b). The Horvath-Kawazoe (H-K) method was applied to evaluate the average pore diameter and the pore size distribution (PSD) (Okolo *et al.*, 2015).

N_2 adsorption was used to investigate changes in the mesopore and macropore structures at a temperature of -196.15 ºC and a relative pressure range of 0.00 to 0.99. The N_2 adsorption surface area was evaluated using the BET and Langmuir models, the PSD was interpreted using the Barret-Joyner-Halenda (BJH) model (Brunauer *et al.*, 1938; Clarkson *et al.*, 2012).

4 CHAPTER 4: UNTREATED SAMPLE CHARACTERISATION

This chapter presents the results of the analytical techniques applied to each of the untreated sandstone samples. XRD, FTIR and LPGA analyses results are outlined for all five samples.

4.1 XRD

XRD data for the untreated Zululand Basin sandstone core samples (Table 4.1) shows the dominance of quartz and plagioclase in the sandstone samples in line with similar results reported in literature (Ward and Taylor, 1999). Stilbite and diopside are observed in small quantities in the ZC sample (3.6% and 2.7% respectively); minor quantities (below 1.5% and 1.9% respectively) are reported in the remaining four samples. A slightly higher composition of smectite was detected in the ZF sample (7.2%); it is present in small amounts of 2.6% and below for the rest of the samples. The ZF sample also has a comparatively high composition of calcite (10%) while the ZA and ZC sample profiles showed calcium at lower composition of 2,4 and 3,5%, respectively. Pyrite is observed in negligible quantities in all the sandstone samples.

Table 4.1: XRD results of the Zululand Basin sandstone core samples.

Sample	Quartz	Plagioclase	Smectite	Calcite	Other	Pyrite	Stilbite	Diopside
ZA Untreated	47,9	45,2	2,2	2,4	2,3	0,3	0,0	2,0
ZC Untreated	44,1	44,7	1,0	3,5	6,7	0,4	3,6	2,7
ZE Untreated	67,4	28,5	2,6	0,0	1,5	0,2	0,7	0,6
ZF Untreated	34,0	47,7	7,2	10,0	1,1	0,3	0,1	0,7
ZG Untreated	21,5	46,0	22,2	0,0	10,3	0,0	1,2	1,9

4.2 FTIR

The FTIR Spectra for all the untreated Zululand Basin sandstone core samples showed the presence of hydroxyl group molecules (Table 4.2) in the transmission region between ~3650 and ~3000 cm^{-1}(Yin *et al.*, 2016; Kutchko *et al.*, 2020). The ZC and ZF samples displayed the presence of C-H stretching bonds in the ~2900 cm^{-1} transmission region (Jiang and Xu, 1995; Nakamura *et al.*, 1996). Whilst only the ZF sample did not register O-H deformation stretching bonds at ~1640 cm^{-1}, C-H deformation stretching bonds and C-O-H bending vibration peaks at ~1480/1424 cm^{-1} were observed in all other samples (Yuvashree and Balavijayalakshmi, 2019; Klima *et al.*, n.d.). The presence of the hydroxyl bonds indicates surface moisture on the respective samples. The ZF sample presented C-N stretching bonds at ~1224 m^{-1} (Jiang and Xu, 1995; McCarthy *et al.*, 1997). All samples showed SiO stretching bonds at ~1015 cm^{-1}, ~778 cm^{-1}, ~666 cm^{-1} and traces of calcite at ~874 cm^{-1} and ~712 cm^{-1} transmission regions (Kutchko *et al.*, 2020).

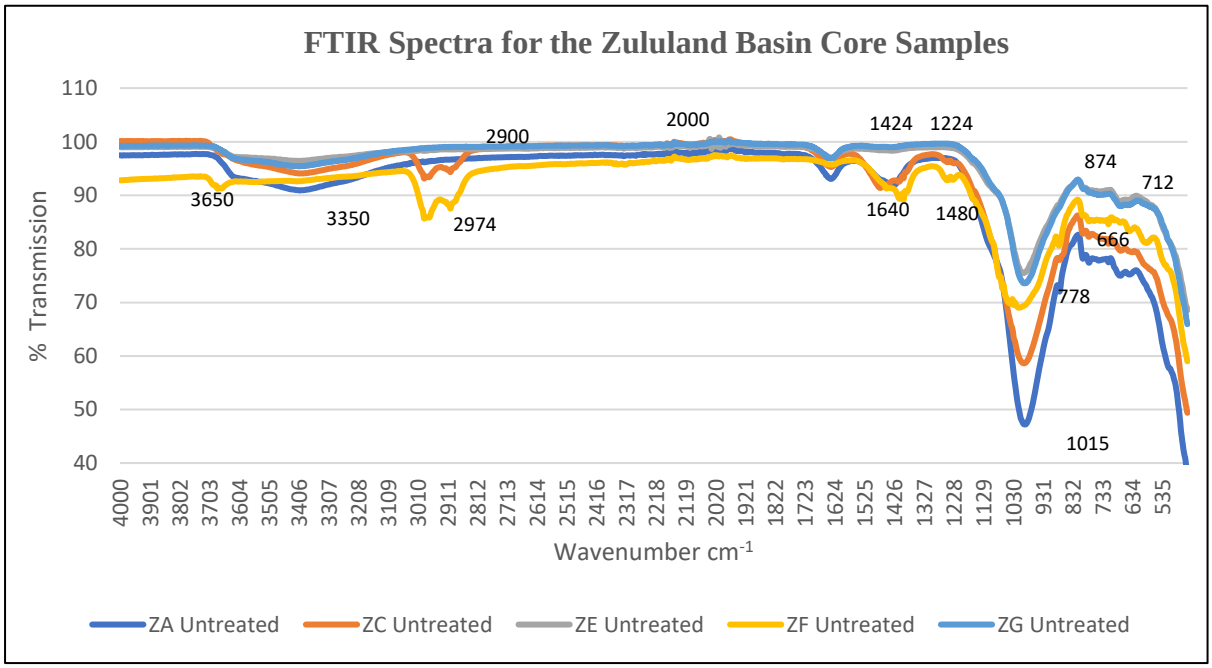

Figure 4.1: FTIR Spectra for the untreated Zululand Basin sandstone samples.

Water stretching bonds were observed at transmission regions of ~3650 and ~1640 cm^{-1} and C-H stretching bonds and bending bonds were observed at transmission regions of ~2900 - ~2974 and ~1480 cm^{-1}. The presence of SiO is indicated by the stretching bonds observed at 1015 cm^{-1} and the bending vibrations at 778 cm^{-1}. Traces of Calcite and pyrite are present in the samples as implied by the stretching bonds at 712 cm^{-1} and 586 $cm^{-1,}$ respectively.

Two representative samples of the untreated ZE core sample (ZE Untreated 1 and ZE Untreated 2) from separate aliquot samples were analysed to verify the repeatability of the analyses, as reported in Mavhengere *et al.* (2021). The two profiles display excellent correlation at an R^2 value of 0.99997 (ZE Untreated samples 1 and 2) as displayed in Figure 4.2.

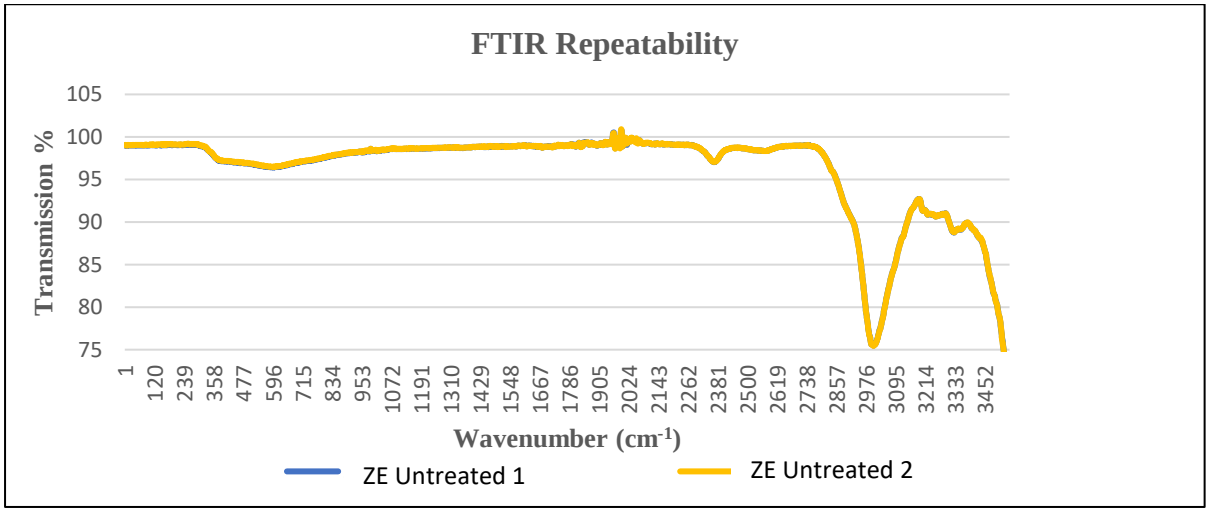

Figure 4.2: FTIR Spectra for ZE representative aliquot samples demonstrating repeatability.

Table 4.2: FTIR Results Summary of the Zululand Basin Sandstone core samples.

Wave-number cm-1	ZA Untreated	ZC Untreated	ZE Untreated	ZF Untreated	ZG Untreated	Peak Assignments
3650	X	X	X	X	X	OH, stretching for water
3350	X	X	X		X	
2974		X		X		C-H stretching of aliphatic bonds (aldehydes and alkanes)
2900		X		X		
2000	X		X	X	X	
1640	X	X	X	X	X	OH, deformation of water
1480		X	X	X	X	CH deformation
1424	X	X	X	X		COH bending vibrations
1224		X		X		C-N bond vibrations
1130	X	X	X		X	C-C stretching modes/ Si-O stretching vibrations in silicates
1050				X		C-O Bond vibrations/Si (Al)-O stretching vibrations in feldspars
1000-1015	X	X	X	X	X	Si (Al)-O stretching vibrations
874	X	X		X		Calcite bending (Out of Plane)
778	X	X	X	X	X	SiO stretching for quartz
712	X	X	X	X		Calcite Bending (In plane)
666	X	X	X	X	X	SiO (perpendicular mode for quartz)

Sources:(Jiang and Xu, 1995; Nakamura *et al.*, 1996; McCarthy *et al.*, 1997; Kloprogge and Frost, 2004; Goodman *et al.*, 2019; Kutchko *et al.*, 2020; Klima *et al.*, n.d.)

4.3 LPGA

LPGA analyses were conducted on all the five (5) untreated samples. Low pressure CO_2 and N_2 adsorption results were used to evaluate the micropore surface area, micropore volume and average pore sizes (**Error! Not a valid bookmark self-reference.**).

Understanding the pore size distribution of geological formations is important for sequestration feasibility assessments (Rani *et al.*, 2020). LPGA was used to evaluate the pore structure of the rock samples. This application is widely applied in sandstone and shale pore structure determination (Labani *et al.*, 2013; Schmitt *et al.*, 2015; Cao *et al.*, 2016; Lai *et al.*, 2018; Lei *et al.*, 2020; Rani *et al.*, 2020). CO_2 gas adsorption was applied in this study for the evaluation of the micropore structure, whereas N_2 gas was employed to outline the mesopore and macropore structure characteristics.

Sandstones are known to present a wide pore size range; this contributes to their permeability and porosity characteristics (Rezaee *et al.*, 2012; Xi *et al.*, 2016; Qiao *et al.*, 2020; Mavhengere *et al.*, 2021). According to Qiao *et al.* (2020), pores under 1µm (10 000 Å) present up to 70% of the pore size distribution in sandstones. Xiao *et al.* (2017) and Zhu *et al.* (2018) reports that these pores are made up of clay associated pores and intraparticle dissolution pores that contribute to percolation, storage, and specific surface area.

Lei *et al.* (2020) studied clay rich tight sandstones classified the pores found into three groups: intercrystalline pores (< less than 100 Å), clay related pores (100- 100 000 Å) and microfractures (>100 000 Å). The micropores are evaluated by low pressure CO_2 adsorption and are a portion of the pores in the intercrystalline pore range. The mesopore and macropore range evaluated by the low-pressure gas adsorption method relates to a small portion of the intercrystalline pores along with the clay dissolution pores which present a strong correlation with porosity and connectivity.

Table 4.3: Low pressure CO_2 gas analyses results on untreated samples

Sample name	**CO_2 D-R Micropore SA (m^2/g)**	**CO_2 D-A Micropore Volume (cm^3/g)**	**Ave Pore size (Å)**
ZA Untreated	18,27	0,0353	9,79
ZC Untreated	18,05	0,0404	9,84
ZE Untreated	13,43	0,0315	10,70
ZF Untreated	16,79	0,0242	10,54
ZG Untreated	12,70	0,0320	6,36

4.3.1 **Micropore Adsorption Isotherms**

Figure 4.3 presents the CO_2 adsorption isotherms for the sandstone samples. The CO_2 adsorption at P/P^0=0.033 ranges between 1.1 and 1,9 cm^3 /g. The ZA, ZC and ZE samples present the highest adsorption capacities presenting maximum quantity adsorbed values above 1,5 cm^3/g. These are followed by the ZF and ZG samples. It is noted that the ZG sample is observed to present almost half the adsorption capacity observed for the ZA, ZC and ZE samples.

It is interesting to note that despite the ZF and ZG samples having the highest clay content as represented by smectite in Table 4.1, their micropore adsorption capacity is the lowest amongst the studied sample. Due to the higher surface area presented by clays, their presence in sandstones is expected to enhance their adsorption capacity (Řimnáčová *et al.*, 2020; Hamza *et al.*, 2021). The micropores in the samples are therefore likely due to the inorganic matter identified in the FTIR spectra of the sandstone samples (Yin *et al.*, 2016; Řimnáčová *et al.*, 2020).

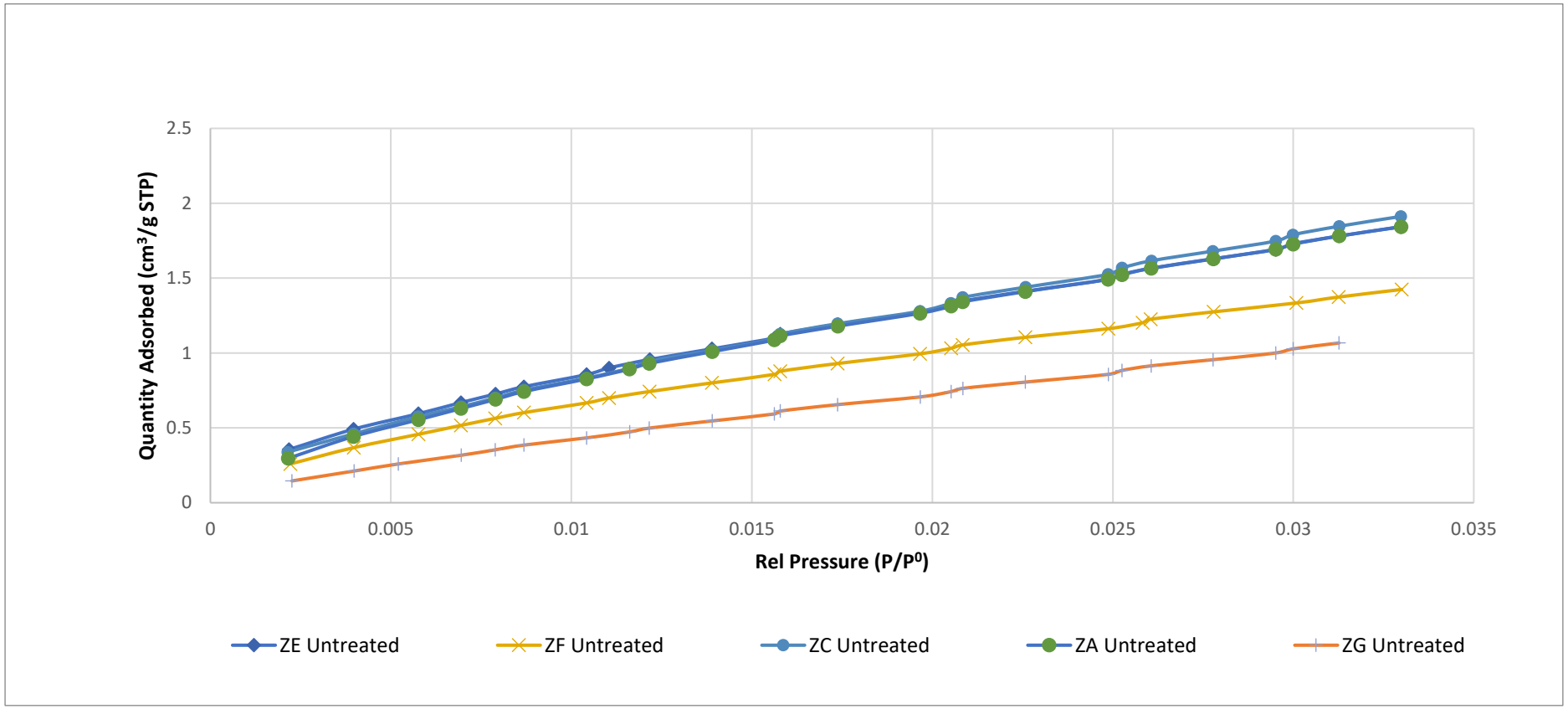

Figure 4.3: CO_2 adsorption isotherms for the untreated Zululand Basin sandstone core samples.

4.3.2 **Micropore PSD profiles**

The H-K model was used to evaluate the micropore PSD profiles in the range of 0 to 5,1 Å (Figure 4.4). Multimodal peaks are observed in all the PSD profiles of the sandstone samples. The sandstone peaks outline similar profiles, apart from for the ZE sample that shows peaks at slightly higher pore widths.

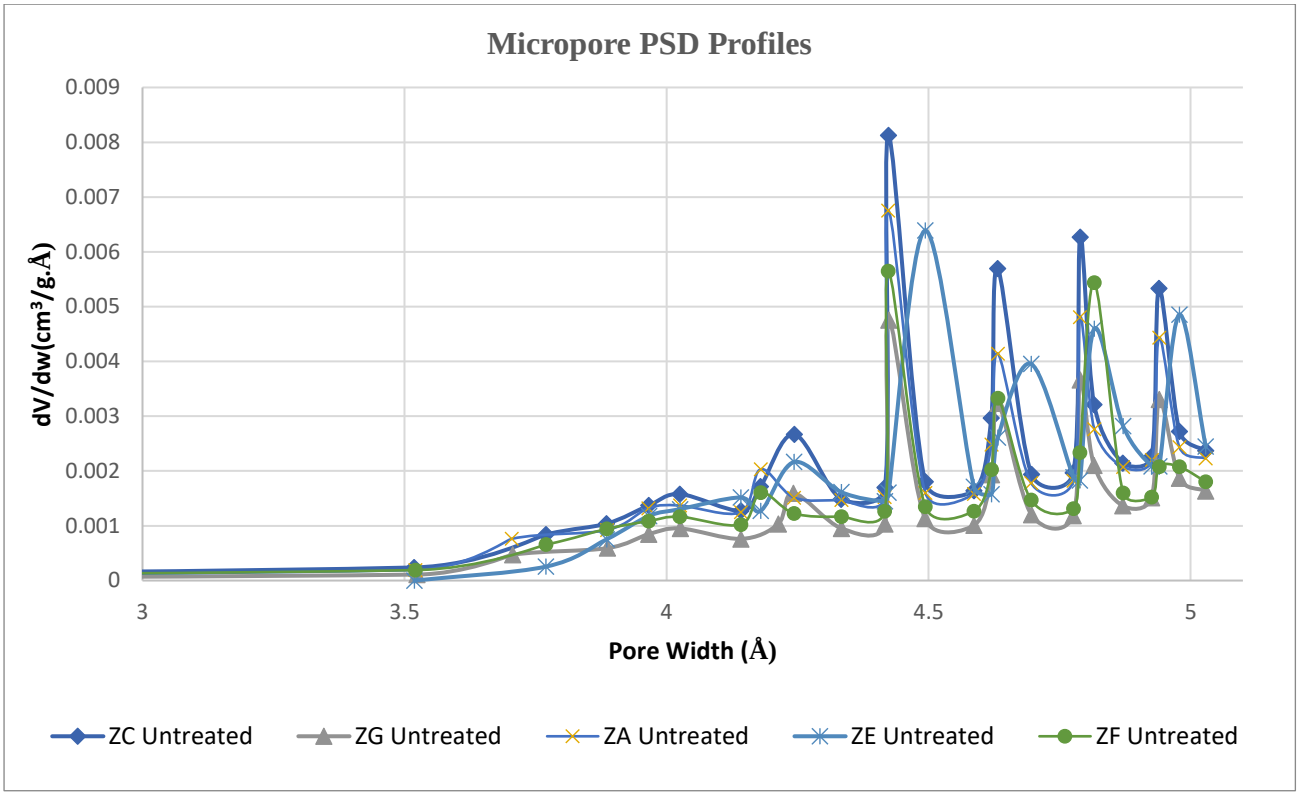

Figure 4.4: Micropore PSD profiles using the H-K method for the untreated Zululand Basin sandstone core samples.

4.3.3 **N_2 Adsorption-Desorption Isotherms**

All the five samples present a type IV N_2 adsorption-desorption isotherms profile (Figure 4.5), which is in accordance with the IUPAC classification (Thommes *et al.*, 2015). Although the untreated ZC sample displays the highest adsorption capacity at the maximum relative pressure of 29,53 cm^3/g STP at P/P^0 of 1, the ZA sample presents a higher adsorption capacity throughout the measurement range. The sample hysteresis loops (difference between the N_2

desorption and adsorption isotherms) are likely a result of the presence of slit shaped pores in the samples (Clarkson *et al.*, 2012; Anovitz and Cole, 2015; Mavhengere *et al.*, 2021).

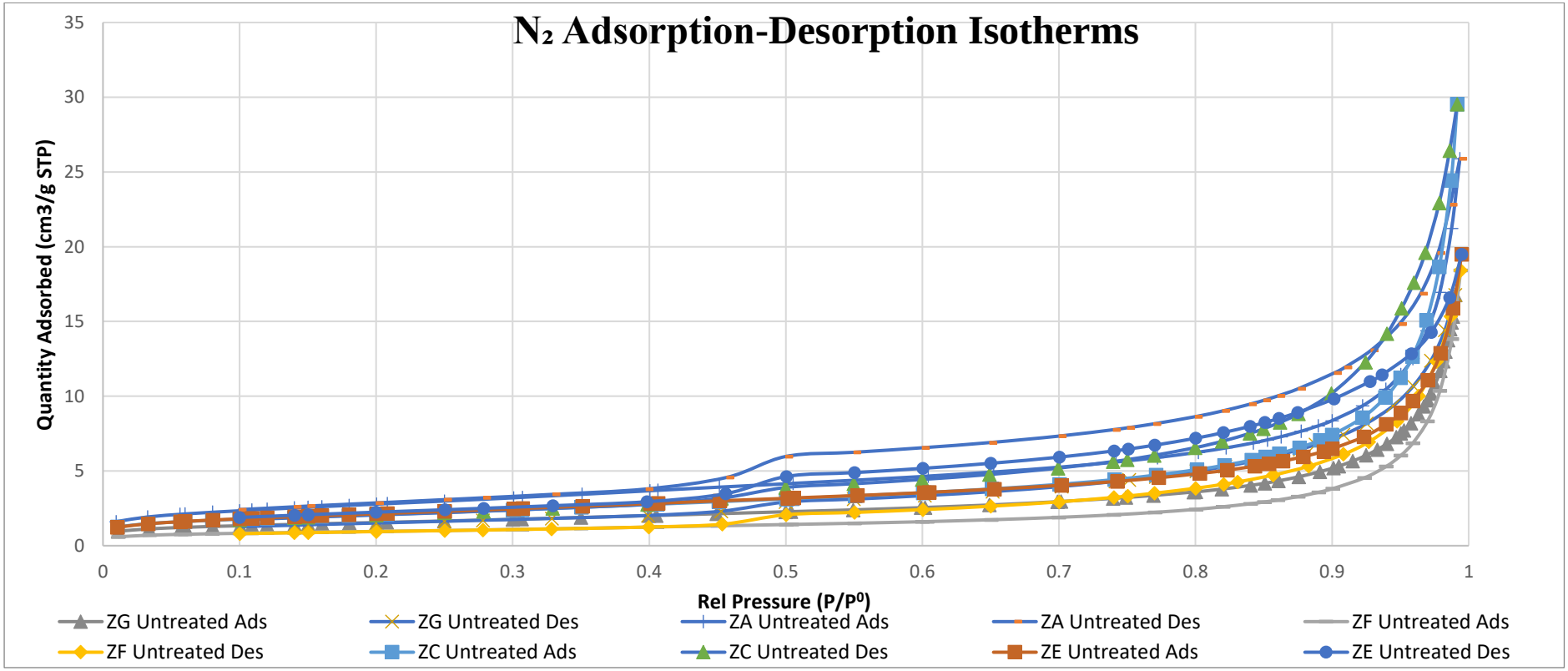

Figure 4.5: N_2 Adsorption (Ads)-Desorption (Des) isotherms for the untreated Zululand Basin sandstone core samples.

4.3.4 **Meso-and Macropore PSD Profiles**

The BJH model was used to determine the PSD profiles of the Zululand Basin sandstone core samples (Figures 4.6 and 4.7). The mesopore PSD profiles for the sandstone core samples display a unimodal peak just below 50 Å pore diameter. The highest mesopore volume (0,000164 cm3/g. Å.) is observed for the ZA untreated sample. A gradual decrease in macropore volume with increasing pore diameter (Figure 4.6) is observed for all the sandstone core samples analysed.

The ZC sample is the only sample that displays weak peaks at a pore diameter of ~ 32 Å in the PSD profile for the range analysed. The highest macropore volume is observed in the ZC sample for the 150-500 Å pore diameter range.

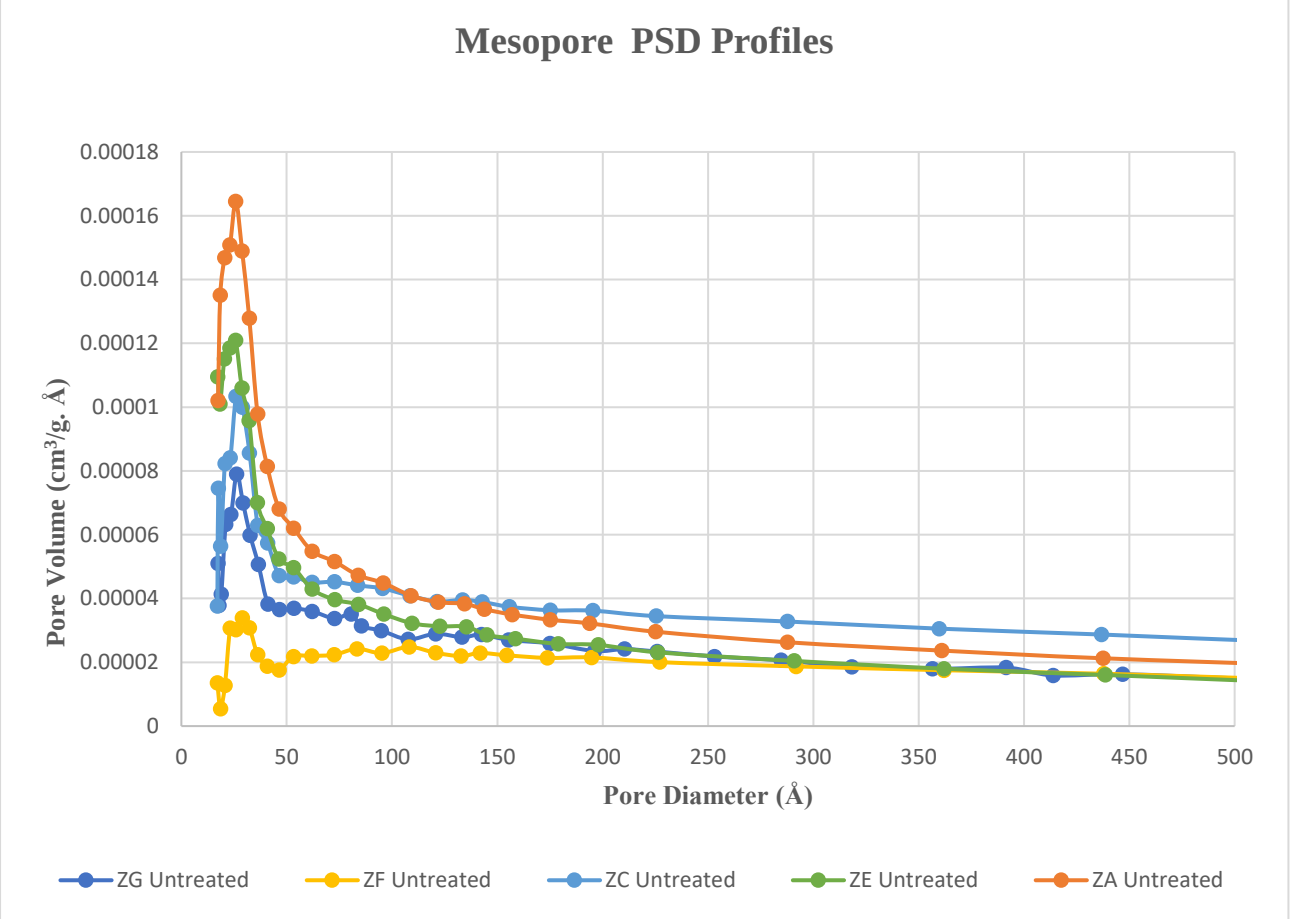

Figure 4.6: N_2 Mesopore PSD profiles determined using the BJH model for the untreated Zululand Basin sandstone samples.

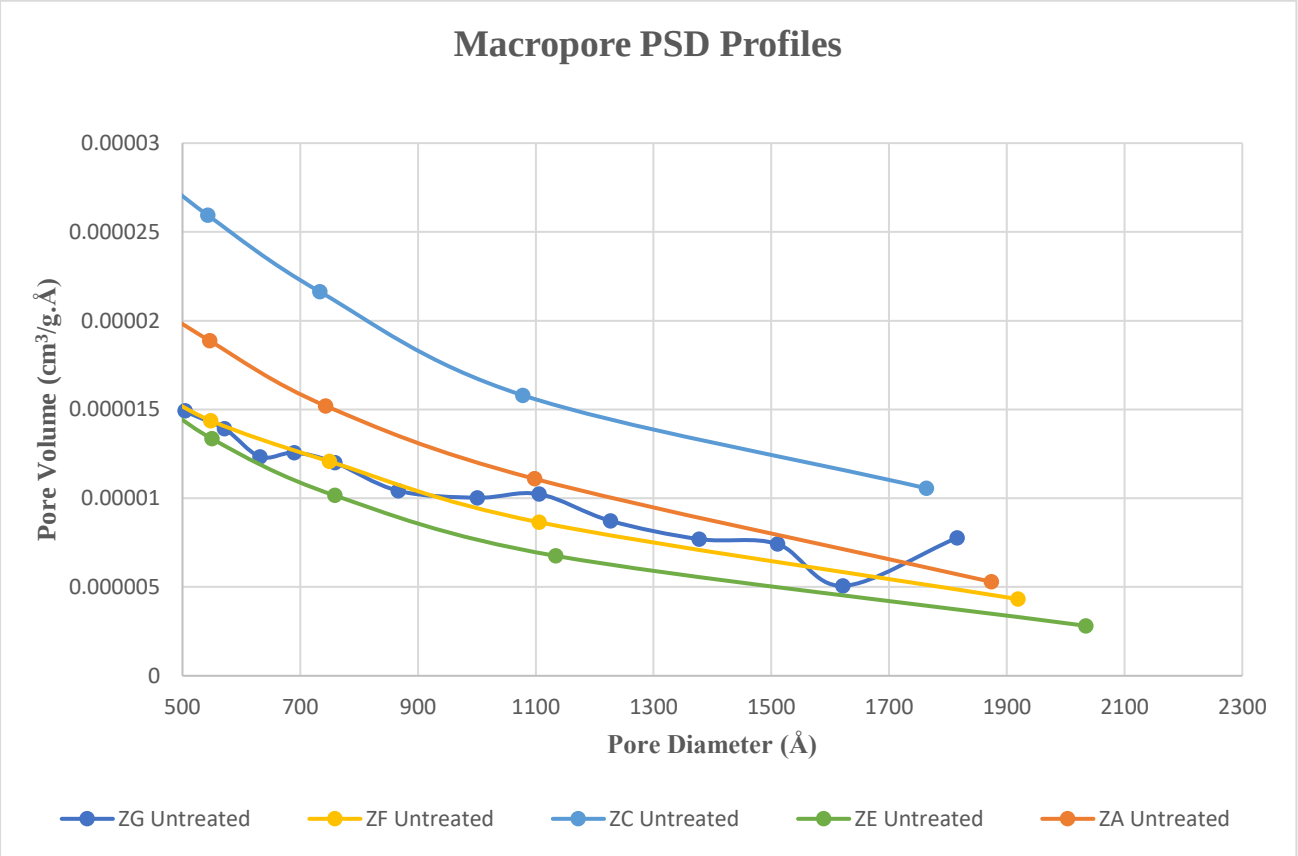

Figure 4.7: Macropore PSD Profiles as evaluated by the BJH model for the untreated Zululand Basin sandstone samples.

4.3.5 **Pore Structure Parameters**

The micropore surface area was determined using the Dubinin-Radushkecich (D-R) method (Table 4.3). The ZA and ZC sandstone untreated samples displayed the highest D-R micropore surface area amongst the sandstone core samples, followed by the ZF, ZE and lastly the ZG sample (16, 79, 13, 43 and 12,7 m^2 /g; respectively). The highest to the lowest surface area order starts with the untreated ZC sandstone untreated sample, this is followed by the ZA, ZF, ZG and lastly the untreated ZE sandstone sample. The Dubinin – Astakhov (D-A) limiting micropore volume was determined along with the average pore sizes for all samples. Amongst the Zululand Basin sandstone core samples, the ZE and ZF samples displayed the highest average pore sizes (9,79 and 9,84 Å respectively) whilst the ZG sample displayed the lowest (6,36 Å).

The low-pressure N_2 gas adsorption isotherms were used to evaluate the meso- and macropore as well as the surface area of the sandstone samples using the BET and Langmuir methods (Table 4.4). The ZA sandstone sample presented the highest meso/macropore surface area; this was followed by the ZC and ZE sandstone samples, and the ZG and ZF samples presented the lowest surface areas amongst the Zululand Basin sandstone core samples. The scatter in the sample results demonstrate pore structure heterogeneity of the Zululand Basin core samples.

Table 4.4: Low Pressure N_2 gas adsorption results of the untreated Zululand Basin sandstone samples.

Sample	**N_2 BET m^2/g**	**N_2 Langmuir m^2/g**
ZA Untreated	3.40	14.72
ZC Untreated	3,17	10,91
ZF Untreated	1,63	5,04
ZE Untreated	2,59	11,37
ZG Untreated	2,1	8,03

4.4 Chapter Summary

Each of the five untreated samples were characterised using XRD, FTIR and LPGA. The chapter offers insight into the mineral composition, surface chemistry and physical pore characteristics of the samples. The XRD results showed quartz and plagioclase dominance in the sandstone samples, which is in line with findings reported for similar studies in literature (Hamza *et al.* 2020). Although the ZA, ZE and ZG samples show similar surface chemistry profiles, differences are observed in the ZC and ZF FTIR profiles.

5 CHAPTER 5: EFFECT OF $_{sc}CO_2$ -WATER TREATMENT

The effects of $_{sc}CO_2$-water treatment were analysed through the comparison between the untreated and treated sample using XRD, FTIR and LPGA. The current chapter focuses on the results of the five untreated and six treated Zululand Basin sandstone core samples (ZA CO_2 treated, ZC CO_2 treated A and B, ZE CO_2 treated, ZG CO_2 treated and ZF CO_2 treated). Samples ZA, ZC, ZE and ZF were obtained from the lower Aptian sandstone with a maximum depth of 1800 m; the ZG sample was collected from the middle Cenomanian sandstone presenting a maximum depth of 1200 m. The shallower ZG sample was therefore treated at a lower pressure and temperature of 120 bars and 43 ºC than the rest of the samples, which were treated at 180 bars and 70 ºC. All samples were exposed to $_{sc}CO_2$ -water treatment for 2 months except for the ZC treated A sample which was treated for a period of 1 month.

5.1 Mineral Alterations as determined by XRD analyses.

XRD is a proven rock sample characterisation technique which has been applied in a number of studies to investigate mineral dissolution and precipitation in samples (Rezaee *et al.*, 2012; Wilke, 2012; Schmitt *et al.*, 2015; Yin *et al.*, 2016; Wu *et al.*, 2019; Yuvashree and Balavijayalakshmi, 2019). Credoz *et al.* (2009) studied mud rock samples treated under CO_2 storage conditions and reported that carbonates, kaolinite and illite/smectite minerals progressively decline with increasing temperature and duration. Comparing the XRD results between the untreated and treated sandstone core samples, various changes in mineral composition are observed (Table 5.1).

Table 5.1: XRD Analyses Results Pre and Post $_{sc}CO_2$ -Water Treatment

Sample name	Quartz (wt. %)	Plagioclase (wt. %)	Smectite (wt. %)	Calcite (wt. %)	Pyrite (wt. %)	Stilbite (wt. %)	Diopside (wt. %)	Orthoclase (wt. %)
ZA Untreated	47,9	45,2	2,2	2,4	0,3	0,0	2,0	0,0
ZA CO_2 treated	61,7	33,8	1,1	0,0	0,0	1,3	2,2	0,0
ZC Untreated	44,1	44,7	1,0	3,5	0,4	3,6	2,7	0,0
ZC CO_2 treated A	47,1	40,8	1,3	2,8	0,4	4,6	3,1	0,0
ZC CO_2 treated B	47,5	42,5	2,5	1,7	0,4	2,7	2,8	0,0
ZE Untreated	67,4	28,5	2,6	0,0	0,2	0,7	0,6	0,0
ZE CO_2 treated	66,7	30,3	1,2	0,0	0,0	1,0	0,7	0,0
ZF Untreated	34,0	47,7	7,2	10,0	0,3	0,1	0,7	0,0
ZF CO_2 treated	37,6	52,1	7,0	0,0	0,4	1,3	1,6	0,0
ZG Untreated	21,5	46,0	22,2	0,0	0,0	2,0	0,0	8,3
ZG CO_2 treated	22,3	50,5	16,3	2,9	0,0	4,8	0,0	3,2

The prominent and expected observation is the dissolution of calcite in all treated samples where calcite is present, in agreement with Emberley *et al.*, 2005, Knauss *et al.*, 2005 and Wang *et al.*, 2017. The changes in mineral composition may be explained by the physiochemical reactions of the acidic $_{sc}CO_2$ -water mixture and the various minerals under high pressure as outlined by Equation (3) (Irfan *et al.*, 2018) (Yin *et al.*, 2016; Mavhengere *et al.*, 2021).

$$CaCO_3\,(calcite) + 2H^+ \rightleftarrows Ca^{2+} + CO_2 + H_2O \ldots\ldots\ldots\ldots (3)$$

A reduction in plagioclase is observed on the ZA and ZC samples (25% and 9% respectively). The ZE, ZF and ZG samples present an apparent increase in plagioclase content (up to 11%). Plagioclase dissolution is known to be associated with calcite formation as a result of the release of Ca^{2+} ions into solution (Carroll and Knauss, 2005; Metz *et al.*, 2005; Kampman *et*

al., 2009; Pham *et al.*, 2011; Munz *et al.*, 2012; Hellevang *et al.*, 2013; Gudbrandsson *et al.*, 2014; Dai *et al.*, 2020). Gudbrandsson *et al.* (2014) further explains that plagioclase dissolution is highly influenced by its structure and composition, implying possible variations in dissolution rates of samples with similar bulk compositions (Oxburgh *et al.*, 1994).

Plagioclase dissolution in acids is outlined in Equations (4) and (5) (Gudbrandsson *et al.*, 2014):

$$Na\,Al\,Si_3O_8(albite) + 4H^+ \rightleftarrows Na^+ + Al^{3+} + 3SiO_{2(aq)} + 2H_{\ 2}O \ldots\ldots\ldots\ldots (4)$$

$$Ca_1Al_2Si_2O_8(anorthite) + 8H^+ \rightleftarrows Ca^{2+} + 2Al^{3+} + 2SiO_{2(aq)} + 4H_{\ 2}O \ldots\ldots\ldots\ldots (5)$$

Some samples, however, present very minor changes in plagioclase concentration; this was also observed by Wang *et al.* (2017) after studying sandstone samples exposed to CO_2 -rich water – rock interaction at a temperature of 85 ºC.

An increase in quartz content of up to 29% is observed in the ZA, ZC, ZF and ZG samples whilst the ZE sample shows negligible changes. Quartz content increase is assumed to be a consequence of the dissolution of other sensitive silicate minerals such as plagioclase, leading to the precipitation of secondary quartz (Dai *et al.*, 2020; Zhang *et al.*, 2020).

The ZC samples portray apparent precipitation of smectite. The rest of the core samples display a reduction in smectite composition after CO_2 treatment, except for the negligible changes observed in the ZF sample. Metz *et al.* (2005) describes the dissolution of smectite in acidic environments as outlined in Equation (6).

$$\begin{aligned}[K_aNa_bCa_cMg_d](Mg_xFe_yAl_z)^{VI}(Al_wSi_{8-w})^{IV}O_{20}[OH]_4 \cdot [H_2O]_n + [12+4w]H^+ \\ + [8-4w]H_2O] \\ \rightleftarrows aK^+ + bNa^+ + cCa^{2+} + [d+x]Mg^{2+} + yFe^{3+} + [z+w]Al^{3+} \\ + [8-w]H_4\,SiO_4 + nH_2O \ldots\ldots\ldots (6)\end{aligned}$$

Smectite precipitation is also reported as an expected product of CO_2 sequestration in typical shale-sandstone systems (Credoz *et al.*, 2009; Thyberg *et al.*, 2010; Lu *et al.*, 2011; Hsieh *et al.*, 2017). Preferential release of Mg and Fe is observed in crystalline basalts as compared to Ca in acidic environments, according to Gudbrandsson *et al.* (2011). This implies the formation of Mg and Fe carbonates over calcite in certain rocks. Reprecipitation of smectite is also common after CO_2 -water -rock treatment (Wu *et al.*, 2019). In fact, Wu *et al.* (2019) reported

a complete conversion of the Ordos Basin sandstone after treatment to $_{sc}CO_2$ and brine through clay mineral dissolution, reprecipitation and re migration. The precipitated clays were observed to remigrate and lead to changes in the physical and structural pore system of the resulting rock.

The ZG samples also present orthoclase dissolution. The ZG sample is the only sample that contained orthoclase amongst the samples studied. The dissolution of orthoclase is acknowledged in similar research and described as follows (Blake and Walter, 1999; Gao *et al.*, 2013):

$$2KAlSi_3O_8 + 2CO_2 + 3H_2O \rightleftarrows 2KHCO_3 + 4SiO_2 + Al_2Si_2H_4O_9 \quad \ldots\ldots\ldots (7)$$

The various mineral alterations are further discussed for each sample in the sections that follow.

5.1.1 **ZA**

The changes in the ZA sample mineral composition after CO_2 treatment are summarised in Figure 5.1. A comparison of the results for the untreated and treated samples was conducted in accordance with Equation (8).

$$\%\ apparent\ variation = \frac{(x - y)}{y} \ldots\ldots\ldots (8)$$

Where:

x is the CO_2 treated sample mineral composition

y is the untreated sample mineral composition.

Calcite dissolution is expected to lead to an apparent increase in mineral composition purely as a function of the reduction in the overall precipitated minerals available. This effect is catered for (Figure 5.1) through the application of Equation (9).

$$a = \left(\frac{y}{1 - c}\right) \ldots\ldots\ldots (9)$$

Where:

a is the percentage resulting mineral composition due to calcite dissolution it is referred to as the "effective variation."

c is the difference between the calcite compositions before and after treatment.

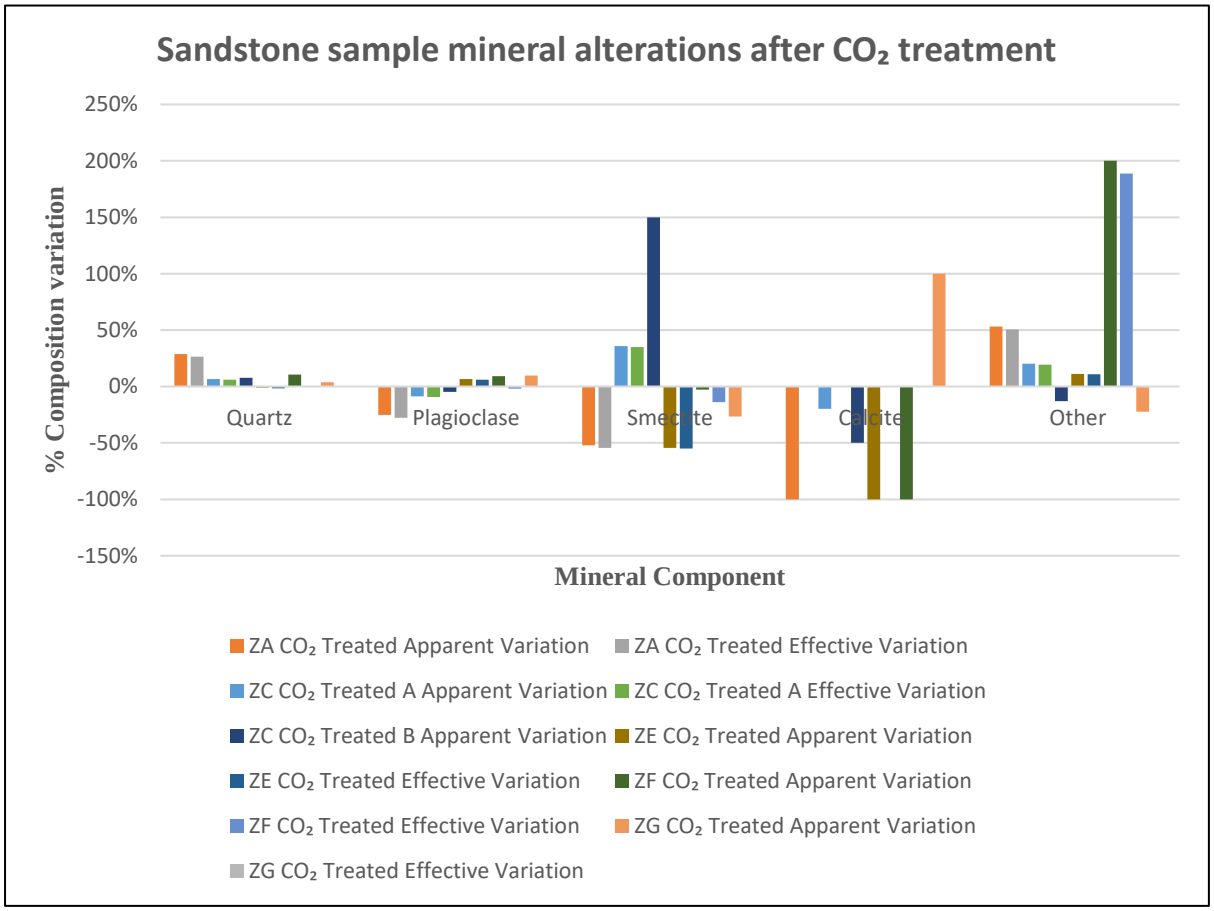

Figure 5.1: Sandstone Core sample variation after CO_2 -Water Treatment

The percentage effective change in composition due to calcite dissolution was evaluated according to Equation (10) and referred to as the calcite effect:

$$d = \frac{(a - y)}{y} \ldots\ldots\ldots (10)$$

An apparent increase of 29% in quartz is observed in the sample after CO_2 treatment. This apparent increase is shown to have been contributed to 2% by calcite dissolution in the sample. The effective variation observed is as a result of calcite dissolution which demonstrates an average 2% increase in composition (calcite effect) of all the other minerals except for the calcite. The decrease in plagioclase of 25% is shown as an apparent decrease of an effective 27% as a result of calcite dissolution in the sample. Smectite also demonstrates an apparent reduction of 52% (apparent variation) indicating a 54% effective reduction. A 53% apparent increase in other minor mineral components (stilbite and diopside) is observed; eliminating the calcite effect leads to an effective increase in composition of approximately 51%. The minimal calcite effect observed in comparison to the apparent variation indicates that the rise in quartz composition is as a result of the secondary precipitation of quartz due to plagioclase and smectite dissolution, in agreement with findings by Dai *et al.* (2020) and Zhang *et al.* (2020).

5.1.2 **ZC**

The ZC treated A and B samples present an apparent increase in quartz composition of up to 7% and 8 %, respectively. Plagioclase is observed to decrease by up to 9% in the ZC treated A sample and the ZC treated B sample similarly shows a decrease of up to 7%. Interestingly, an increase of smectite composition is reported, up to 35% for the ZC treated A sample and a 150% increase in the ZC treated B sample. A 20% and 50% reduction in calcite is observed for the ZC treated A and B samples, respectively. The calcite dissolution effect is observed to increase each of the mineral components of the ZC treated A and B samples by 1% and 2%, respectively. The implied changes in quartz composition are very negligible and are in line with the average absolute deviation of 6% evaluated as the experimental error margins. This indicates negligible changes in quartz composition in the samples. Plagioclase dissolution is also indicated in small magnitudes of 10% and 7%, respectively in the ZC treated A and B samples. A notable increase in smectite composition is observed at varying levels for the two treated core samples (35% and 148% effective increases in smectite composition). Smectite precipitation is observed to significantly increase in ZC treated B sample than in ZC treated A sample. The ZC treated A core sample shows varying minor changes (increase in composition of 17% in the ZC treated A sample and a decrease in composition of 16% in the ZC treated B sample) in the remaining minor mineral components in line with the higher average absolute deviation of 13%. This behaviour is in line with findings reported by Wu *et al.* (2019).

Dissolution and precipitation of various clay minerals is observed in the ZC treated samples; this is shown to be higher in the ZC treated sample B that was treated for a longer period of 2 months.

5.1.3 **ZE**

The ZE sample presents negligible changes in quartz composition of -1%, and a 6% plagioclase reduction is also reported. Smectite is observed to decrease by 54%, whilst minor minerals are observed to increase by 22% between the untreated and treated samples. Considering the small compositions of the smectite and minor minerals in the rock, (2,6% and 1,3 % respectively), it is acknowledged that the changes in mineral composition are minimal. It can be concluded that only slight smectite dissolution was observed after $_{sc}CO_2$ -water treatment along with the negligible precipitation of diopside and stilbite. The ZE sample contains the highest composition of quartz mineral in comparison to the other samples studied. This might explain the low reactivity of the sample. The plagioclase is the second highest component at 28.5%, and a slight increase in concentration is observed after treatment, it must be noted that the increase in composition reported may also be partially attributed to the combined smectite and calcite dissolution effect. The resulting effect indicates poor reactivity of the quartz, and plagioclase components dominate the sample. It may be inferred that the contained plagioclase group in this sample is possibly the less reactive anorthite group.

5.1.4 **ZF**

The ZF sample presents apparent increases in quartz and plagioclase following treatment. A slight decrease in smectite composition of 3% is observed. The calcite contained in the sample is shown to be reduced completely resulting in no calcite being observed in the treated sample. Other minor mineral components are observed to show an increase in composition of up to 70 %. The effect of calcite dissolution is observed to result in a 11% apparent increase in composition across all the other minerals. This indicates that no changes in quartz composition and only minor plagioclase dissolution is observed as a result of $_{sc}CO_2$ -water treatment. An effective reduction in smectite dissolution of 14% is observed, indicating minor dissolution of smectite which could be led to the precipitation of other minor minerals in line with findings reported on the ZE sample. The mineral component reactivity therefore demonstrates complete dissolution of calcite (10% of the samples), partial dissolution of smectite (7.2% of the sample)

and the precipitation of minor minerals stilbite and diopside which represent ~2% of the rock sample.

5.1.5 **ZG**

Quartz, plagioclase, and calcite precipitation are reported after $_{sc}CO_2$ -water treatment at precipitation rates of 4%, 10% and 100% respectively. In the absence of calcite, smectite is shown to dissolve during treatment in the ZG sample. The dissolution of smectite may in turn lead to calcite precipitation.

This sample presents notably different reactions taking place during treatment; this is partly due to the difference in sample composition when compared to the other core samples. The ZG sample presents the lowest composition of quartz in the untreated sample (21.5%) and high compositions of mineral clays such as smectite at 22% composition. The dissolution of smectite facilitates the precipitation of plagioclase, quartz and calcite as outlined by Equation (6). The dissolution of orthoclase also contributes to the precipitation of quartz and introduces aqueous SiO_2 into the $_{sc}CO_2$ -water-rock mixture. Orthoclase is also observed to dissolve by over 60% from 8.3% to 3.5%.

5.2 The Effects of CO_2 on the Chemical Structure as Determined by FTIR Analysis

FTIR spectroscopy has been widely applied for molecular characterisation of geological materials (Yin *et al.*, 2016; Theodosoglou *et al.*, 2017; Mavhengere *et al.*, 2021). The technique allows for the simultaneous study of both inorganic and organic species in a relatively small quantity of sample (Theodosoglou *et al.*, 2017). Applications of the FTIR technique has demonstrated its ability to satisfactorily characterise sediments such as those expected in the samples under study (Herbert *et al.*, 1992; Bishop *et al.*, 1996; Reig *et al.*, 2002; Theodosoglou *et al.*, 2017). According to Yin *et al.* (2016) and Lu *et al.* (2015), surface chemistry alterations may influence rock adsorption behaviour of CO_2 and other gases.

FTIR analyses results for each of the samples are discussed. It is generally observed that the peak intensities are significantly reduced after CO_2 treatment (Figures 5.2 to 5.6). The lower peak intensities were observed in similar studies on CO_2 treated samples such as Yin *et al.* (2016) and Goodman *et al.* (2019). The peak assignments are outlined in Table 5.2.

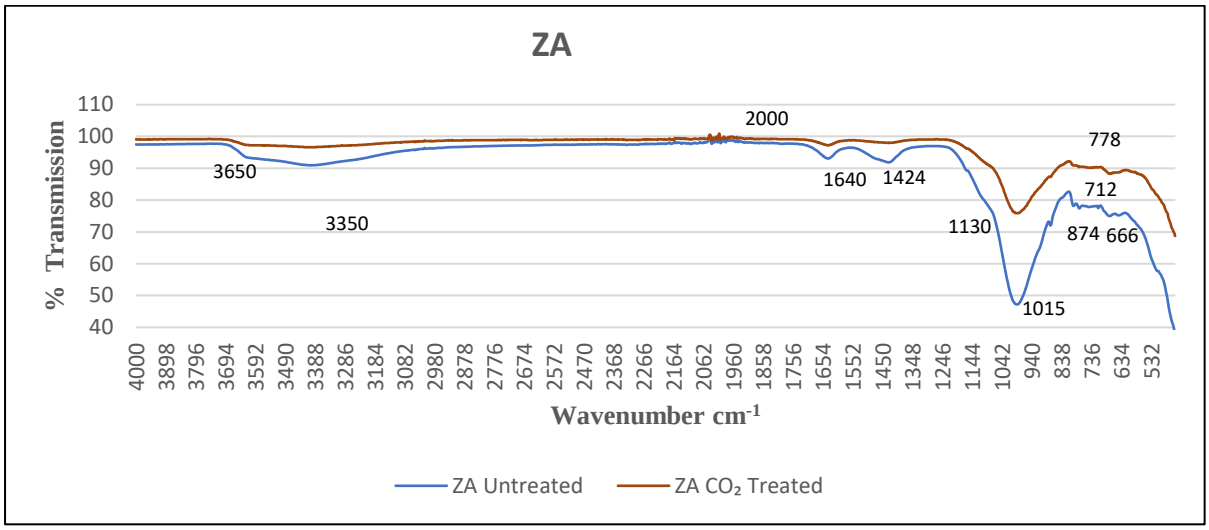

Figure 5.2: ZA FTIR Spectra for the untreated and CO_2 treated samples.

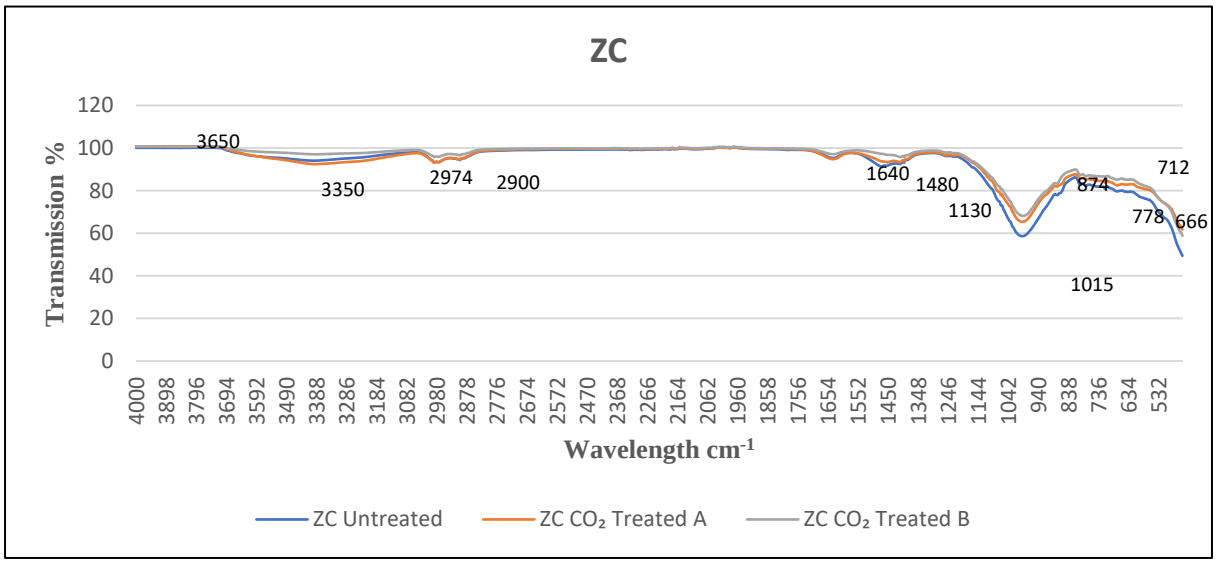

Figure 5.3: ZC FTIR Spectra for the untreated and CO_2 treated samples.

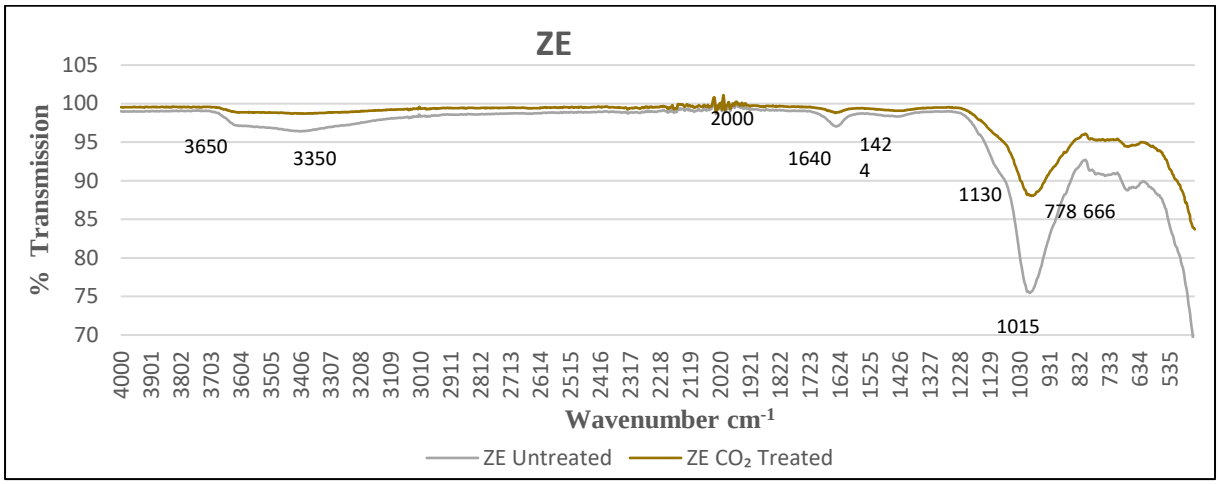

Figure 5.4: ZE FTIR Spectra for the untreated and CO_2 treated samples.

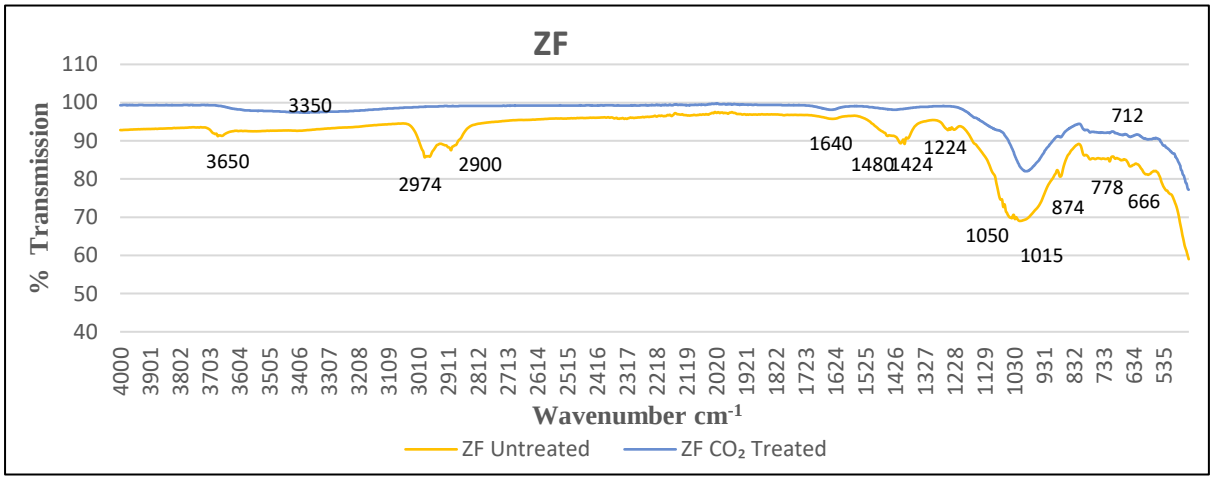

Figure 5.5: ZF FTIR Spectra for the untreated and CO_2 treated samples.

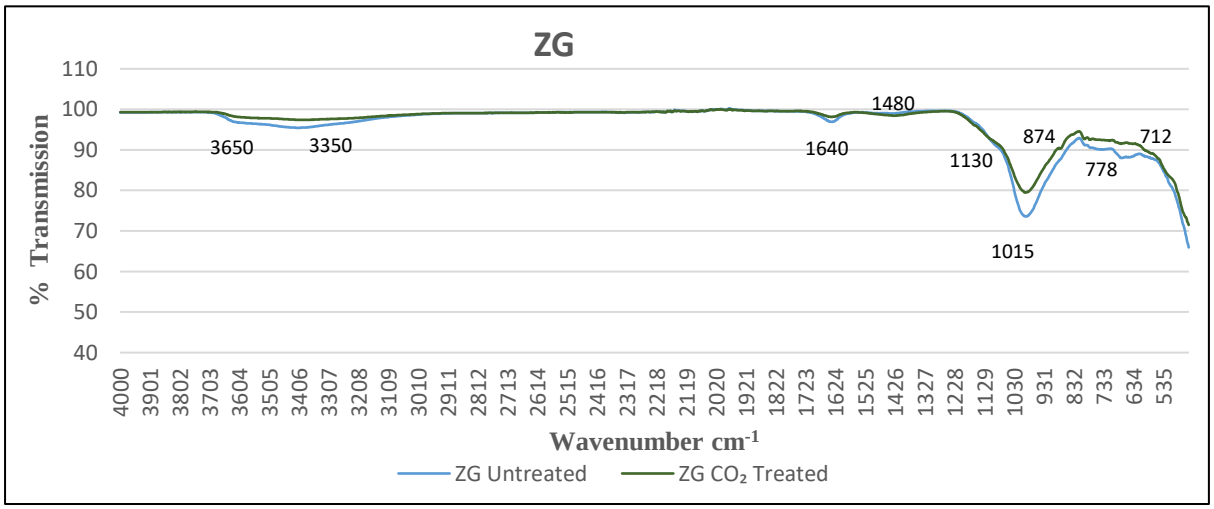

Figure 5.6: ZG FTIR Spectra for the untreated and CO_2 treated samples

Table 5.2: FTIR Peak Assignments.

Wave- number cm-1	ZA		ZC			ZE		ZF		ZG		Functional group assignments
	Untreated	CO_2 treated	Untreated	CO_2 treated A	CO_2 treated B	Untreated	CO_2 treated	Untreated	CO_2 treated	Untreated	CO_2 treated	
3650	X	X	X	X	X	X	X	X	X	X	X	OH, stretching for water
3350	X	X	X	X	X	X	X		X	X	X	
2974			X	X	X			X				C-H stretching of aliphatic bonds (aldehydes and alkanes)
2900			X	X	X			X				
2000	X	X				X	X	X	X	X	X	
1640	X	X	X	X	X	X	X	X	X	X	X	OH, deformation of water
1480			X	X	X	X		X	X	X	X	CH deformation
1424	X	X	X	X	X	X	X	X	X			COH bending vibrations
1224			X	X	X			X	X			C-N bond vibrations
1130	X	X	X	X	X	X	X		X	X	X	C-C stretching modes/ Si-O stretching Vibrations in silicates
1050								X				C-O Bond vibrations/Si (Al)-O stretching vibrations in feldspars
1000-1015	X	X	X	X	X	X	X	X	X	X	X	Si (Al)-O stretching vibrations
874	X	X	X	X	X			X	X		X	Calcite bending (Out of Plane)
778	X	X	X	X	X	X		X	X	X	X	SiO stretching for quartz
712	X		X	X	X	X		X	X		X	Calcite Bending (In plane)
666	X	X	X	X	X	X	X	X	X	X	X	SiO (perpendicular mode for quartz)
580-600												FeO/ O-Si (Al)-O bond vibrations for example in feldspars

Sources:(Allen *et al.*, 1994; Jiang and Xu, 1995; Nakamura *et al.*, 1996; McCarthy *et al.*, 1997; Reig *et al.*, 2002; Kloprogge and Frost, 2004; Lane, 2007; Schuttlefield *et al.*, 2007; Rubasinghege and Grassian, 2013; Thompson *et al.*, 2013; Loring *et al.*, 2015; Theodosoglou *et al.*, 2017; Goodman *et al.*, 2019; Yuvashree and Balavijayalakshmi, 2019; Kutchko *et al.*, 2020; Klima *et al.*, n.d.)

The spectra reports the presence of non-structural water through O-H bond at wavelengths of 3650-3350 cm^{-1} and 1640 cm^{-1} (Table 5.4) in the sandstone core samples, in agreement with findings observed by Goodman *et al.* (2019) and Kutchko *et al.* (2020). Water films on mineral surfaces has been confirmed in numerous studies through the identification of broad anti-symmetric and symmetric stretching and bending modes at 3380 cm^{-1} and 1640 cm^{-1} respectively (Schuttlefield *et al.*, 2007; Rubasinghege and Grassian, 2013; Thompson *et al.*, 2013; Loring *et al.*, 2015; Goodman *et al.*, 2019). According to Schuttlefield *et al.* (2007) and Goodman *et al.* (2019), absorption bands were observed near 3400 and 1635 cm^{-1} at high humidity levels, indicating water absorption on external surfaces and in the available clay interlayers. It is interesting to note that all the analysed samples presented a degree of water film coating on the sample surfaces. This is shown to reduce after treatment due to the sample drying process under which only the treated rock samples were exposed.

The presence of organic matter such as aldehydes, alkanes and allenes are indicated by the peaks observed at 1424, 2000, 2900 and ~2974 cm^{-1}. The peaks at 2000, 2900 and 2974 cm^{-1} are related to C-H vibrations associated with aldehydes, allenes and alkanes whilst the peak at 1424 cm^{-1} denotes the presence of the C-OH bonds representing amines and alcohol. Oxygen containing functional groups have been known to play a significant role in the adsorption of CO_2 at high pressures (~25 MPa) as shown by Liu and Wilcox (2012) and Yin *et al.* (2016). The 1130 peak was identified by Theodosoglou *et al.* (2017) whilst analysing feldspar FTIR spectra as indicative of the presence of Si-O functional group in silicates. The 1050 cm^{-1} peak has been observed to represent the Si (Al)-O stretching vibrations in feldspars by Theodosoglou *et al.* (2017). The same peak was also observed to indicate the presence of the C-O bond by Yin *et al.* (2016) when he studied the effects of $_{sc}CO_2$ treatment on shale samples. The presence of quartz is indicated by the dominant peak at 1015 cm^{-1} along with the peaks at 778 cm^{-1} and 666 cm^{-1}, which represent the SiO functional groups (Schuttlefield *et al.*, 2007; Kutchko *et al.*, 2020). Calcite peaks are observed at wavelengths of 712 cm^{-1} and 874 cm^{-1} (Reig *et al.*, 2002; Goodman *et al.*, 2019). The peaks between 580 and 600 were identified to represent the presence of at 586 cm^{-1} implies the presence of O-Si (Al)-O bonds in feldspars as observed by Theodosoglou *et al.* (2017) or FeO bonds representing the presence of pyrite (Kutchko *et al.*, 2020).

5.2.1 **ZA**

Figure 5.2 presents the FTIR spectra of the ZA untreated and CO_2 treated samples. Although similar profiles are observed for the two samples, minor variations in peak profiles are noted in the region between 874 cm^{-1} to 712 cm^{-1} relating to the presence of calcite in the untreated sample (Table 5.2). The 712 cm^{-1} peak is not detected in the treated sample, indicating the absence of calcite. Smaller and pronounced peaks are observed in the untreated sample in comparison to the treated sample throughout the profile. This indicates a subtle variation in functional group constitution after CO_2 treatment. This observation corresponds with XRD results that indicate calcite dissolution after CO_2 treatment.

5.2.2 **ZC**

The ZC samples do not show obvious signs of functional group changes after treatment. The three profiles for the untreated, treated A (sample treated with $_{sc}CO_2$ -water for 1 month) and treated B (sample treated with $_{sc}CO_2$ -water for 2 months) samples are presented in Figure 5.3. The ZC CO_2 treated A sample shows stronger hydroxyl peaks at 3650-3350 cm^{-1} as compared to the untreated and CO_2 treated B sample. The ZC CO_2 treated A had C-H and O-H deformation peaks at 2900-2974 and 1624 cm^{-1} are identical to the untreated sample. The 1480 to 544 cm^{-1} vibrational peak range shows a decrease in peak intensity throughout the rest of the spectrum. A reduction in the C-H deformation peak is observed at 1480 cm^{-1} where a slight change in profile peak is noted. Mayerhöfer, 2004, reports that the reduction in peak intensity after CO_2 treatment has been shown to indicate an increase in micro heterogeneity of the sample. This may also explain the stronger hydroxyl peaks observed only in the A sample, these likely indicates reduced sample heterogeneity in line with the increased mineral dissolution reported in the same sample during XRD analyses.

5.2.3 **ZA**

The ZA CO_2 treated B sample generally shows a less intense spectrum as compared to the untreated and CO_2 treated sample. All peaks are maintained or remain the same in the ZA CO_2 treated B spectrum except for the C-N bond vibration peak.

5.2.4 **ZE**

The ZE CO_2 treated sample similarly shows a notable reduction in intensity of the spectrum peaks compared to the untreated sample (Figure 5.4). The sample shows presence of O-H functional group for water (3650 - 3350 and 1640 cm^{-1}), subtle organic group vibrations in 2000 and 1424 cm^{-1}), SiO functional groups for quartz at 1000-1015 cm^{-1} and 778 cm^{-1}.

5.2.5 **ZF**

The ZF CO_2 treated sample displays a different spectrum in comparison with the ZF untreated sample spectrum. The untreated sample is observed to contain water (1640, 3350 - 3650 cm^{-1}), organic matter (1050, 1224, 1424, 1480, 2900-2974 cm^{-1}), silica (778, 1000 - 1015 cm^{-1}) and calcite (874 cm^{-1}). The absence of some of the organic matter and silicate functional groups is observed in the CO_2 treated sample in comparison to the untreated sample (1050, 1224, 2900 and 2974 cm^{-1} representing C-H and C-N functional groups respectively). Yin *et al.* (2016) observed similar findings which he attributed to the probable dissolution of organic matter in the sample during treatment. A reduction in the calcite peak (874 cm^{-1}) after CO_2 treatment is observed in agreement with the XRD results. It may be stated that the treated samples present higher micro-heterogeneity as compared to the untreated sample.

5.2.6 **ZG**

Minimal changes in the spectra profile peaks are observed in the ZG samples. The O-H functional groups for the presence of water at 1640 and 3350-3650 cm^{-1}, are observed in both the treated and untreated samples. The organic functional group peaks (1130 and 1480 cm^{-1} representing the C-C and C-H functional groups respectively) are also observed in both samples.

The $CaCO_3$ IR vibrational modes are observed at 712 cm^{-1} and 874 cm^{-1}. A weaker peak at 712 cm^{-1} is observed after treatment, and the 874 cm^{-1} peak is only observed in the treated sample spectrum in agreement with XRD results. The presence of quartz is indicated by the SiO functional group peaks at 1015 cm^{-1} and 778 cm^{-1}; these peaks are observed on both samples.

5.3 The Effects of CO_2 on the Sandstone Physical Characteristics as determined by LPGA

5.3.1 Low Pressure CO_2 Adsorption

5.3.1.1 CO_2 Adsorption Isotherms

It is known that the micropores of geological materials contribute to the adsorption of CO_2 (Ross and Bustin, 2007). All the Zululand Basin sandstone samples displayed an increase in the CO_2 adsorption isotherms after $_{sc}CO_2$ -water treatment except for the ZA sample, which presents the contrary (Figure 5.7 to Figure 5.11). The ZA sample presents a 9% decrease in adsorption capacity at P/P^0 of 0.033; this may be influenced by the mineral alterations in the sample after treatment (Figure 5.7). The ZA sample displayed significant quartz and stilbite reprecipitation characteristics compared to the other rock samples, which could have led to micropore clogging (Farquhar *et al.*, 2015; Luo *et al.*, 2018). The ZC untreated sample adsorption isotherm differs from the ZC treated A and B sample adsorption isotherms, the latter showing almost identical adsorption isotherms. A 14 % increase in the quantity of CO_2 adsorbed at $P/P^0 = 0.033$ is determined for ZC treated A sample. The ZC treated B sample presents a 12% increase in adsorbed CO_2 quantity at the same relative pressure. The ZE, ZF and ZG CO_2 treated samples show a 7%, 9% and a notable 70% increase in CO_2 adsorbed at $P/P^0 = 0.033$ compared to the respective untreated samples. The higher increase in the adsorption capacity reported in the ZG sample may be a result of the dissolution of orthoclase and smectite to form calcite and plagioclase. It is interesting to note the difference in the nature and magnitude of the alterations in all treated samples.

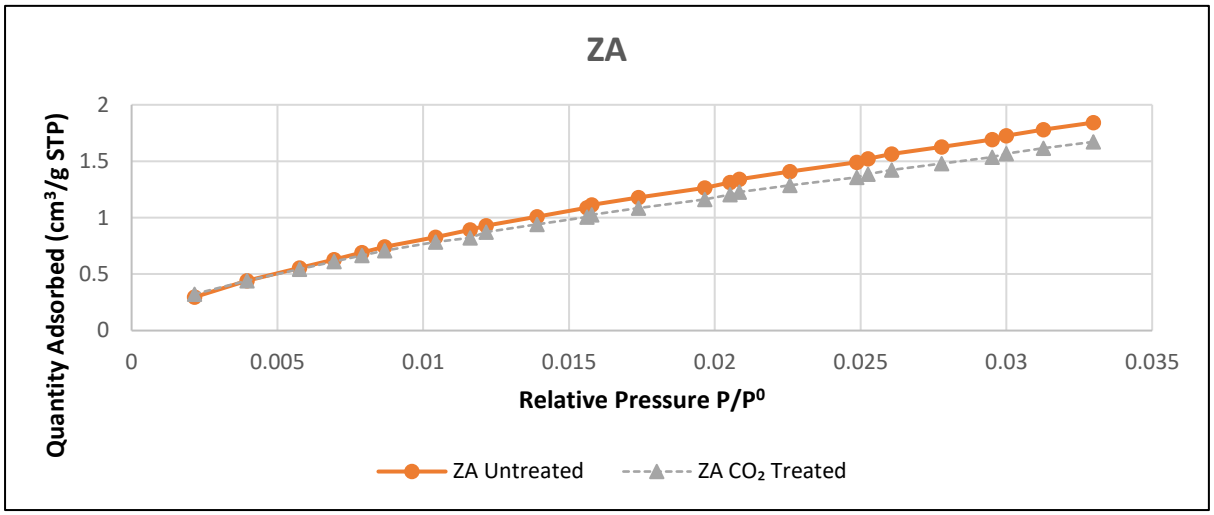

Figure 5.7: ZA untreated and treated samples: CO_2 Adsorption Isotherms

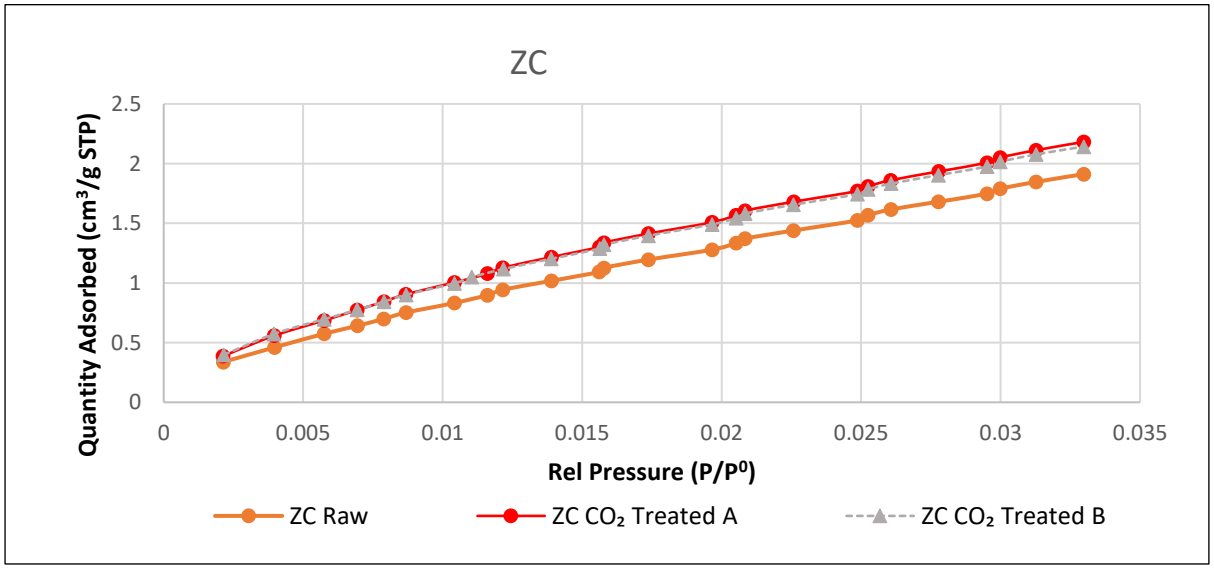

Figure 5.8: ZC untreated and treated samples: CO_2 Adsorption Isotherms

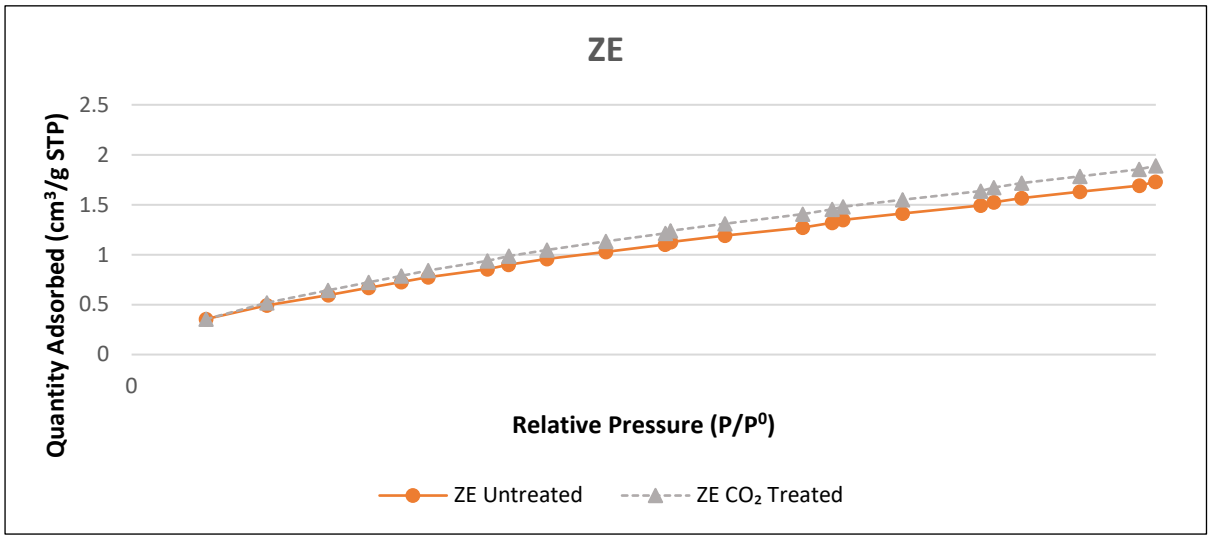

Figure 5.9: ZE untreated and treated samples: CO_2 Adsorption Isotherms

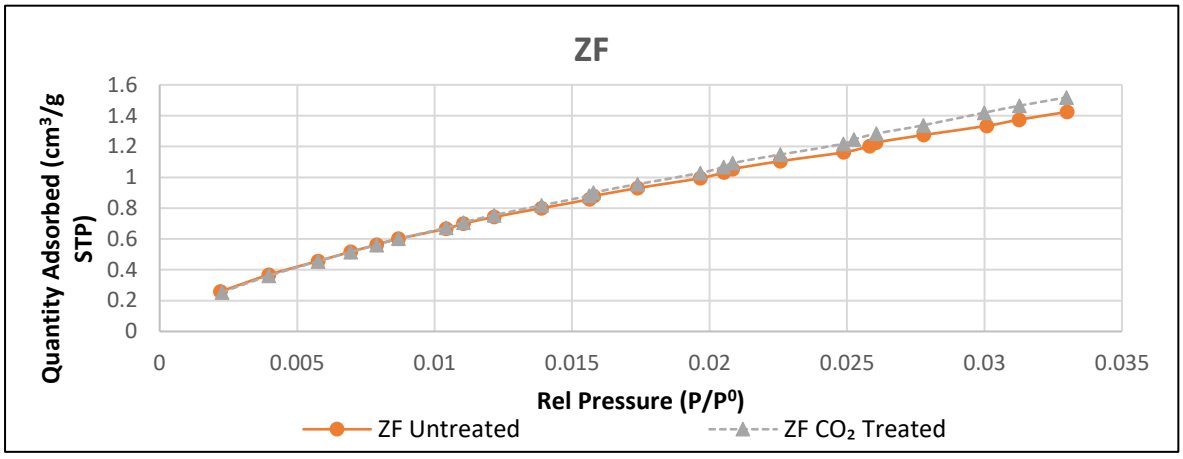

Figure 5.10: ZF untreated and treated samples: CO_2 Adsorption Isotherms

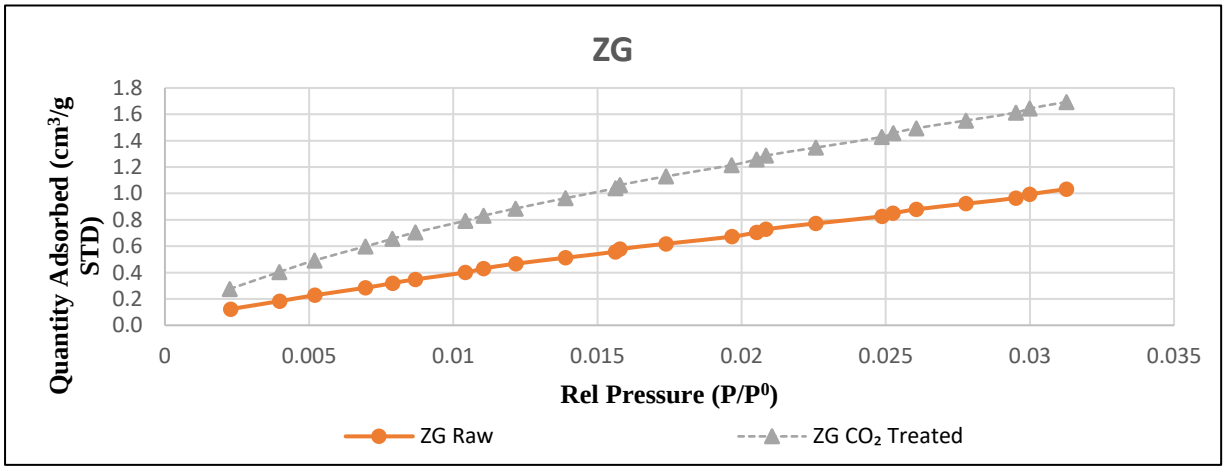

Figure 5.11: ZG untreated and treated samples: CO_2 Adsorption Isotherms

5.3.1.2 Micropore size distribution profiles

The H-K method was used to evaluate the Micropore Size Distribution (MSD) profiles of the samples (Figure 5.12 to Figure 5.16). The MSD profiles display micropore volumes in the pore width ranges of 3 to 5 Å (0.3 to 0.5 nm). All samples (both untreated and treated) present multimodal PSD profiles. The ZA sample displays a lower pore volume profile after $_{sc}CO_2$ -water treatment. Higher pore volume peaks are reported in one of the multimodal profiles of the ZC and ZE samples, at pore widths of 4.78 Å and 4. 94 Å, respectively. The ZF untreated sample reports higher pore volume peaks than the treated sample at two pore width sizes at 4.42 Å and 4.82 Å on the PSD profile. The ZG sample shows a significantly higher pore volume profile with all peaks observed on the untreated sample appearing at much higher peaks on the treated sample profile. It is interesting to note the shift in the peak observed at 4.18 Å in the ZG untreated sample to 4.24 Å in the ZG CO_2 treated sample. This indicates a decrease in the micropore sizes in this range during treatment. The same shift in the peaks is also observed in the ZC treated B sample. The ZC treated A sample shows the highest pore volume in a pore width range of 3.00 - 4.14 Å; beyond which the ZC treated B sample portrays the highest pore volume and records a peak at 4.18 Å pore width. A dip in pore volume is then observed up to 4.33 Å, where after the pore volume profiles of the ZC treated A and B samples are similar. The ZF sample also shows a shift in the 4.82 Å pore width peak to 4.78 Å in the treated sample. The ZG sample similarly demonstrates a shift in the peak at 4,24 Å to 4,21 Å pore width after treatment. These results demonstrate alterations in the MSD's as a result of $_{sc}CO_2$ -water interactions. Other researchers have reported that micropore alterations were observed in carbonate rich shales and sandstones after $_{sc}CO_2$ -water treatment (Jiang *et al.,* 2016; Yin *et al.,* 2016; Pan *et al.,* 2018; Goodman *et al.,* 2019). Micropores in sandstones have been shown to occur as a distribution of dissolution micropores, ductile rock fragments and within clay minerals (Zhu *et al.,* 2018). The dissolution micropores may arise from the presence of partial carbonate minerals in the sample that may dissolve, leading to an increase in pore volume (Luo *et al.,* 2018). The $_{sc}CO_2$ -water treatment interactions influencing the micropore structure are discussed in detail below.

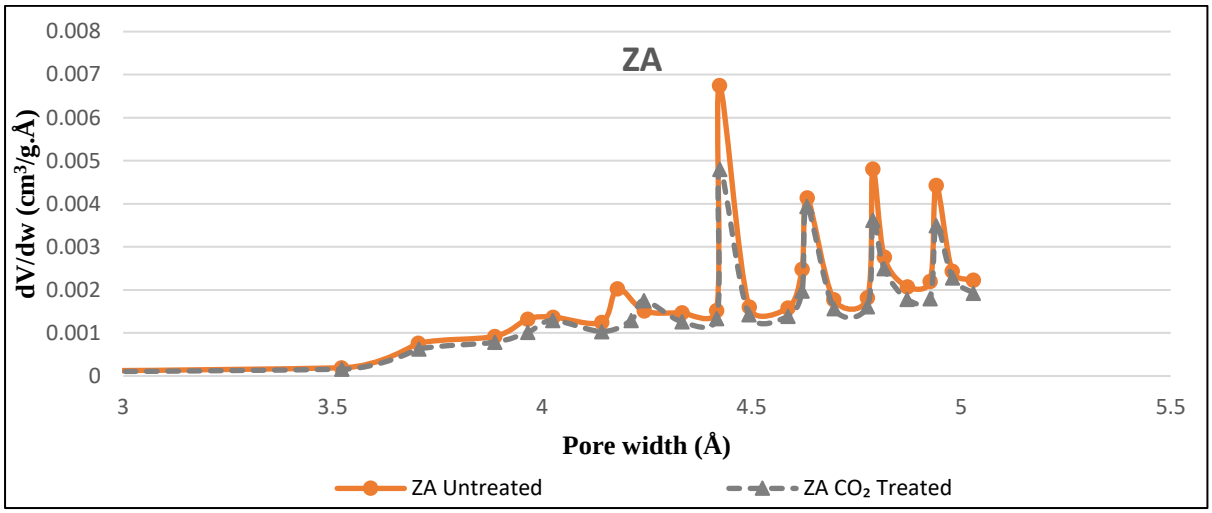

Figure 5.12: ZA untreated and treated samples: Pore Size Distribution profiles

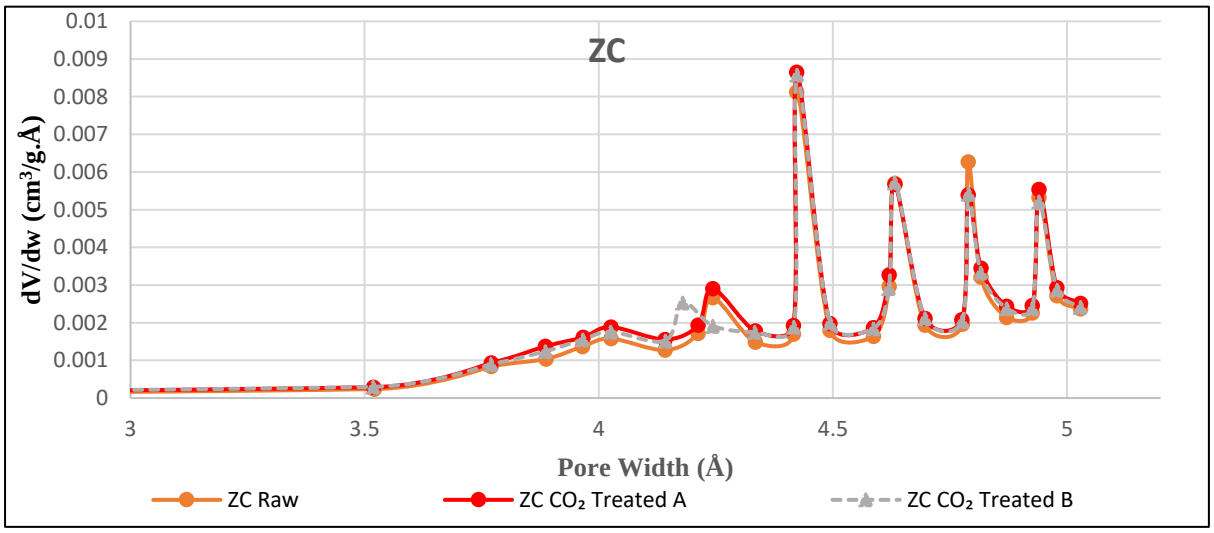

Figure 5.13: ZC untreated and treated samples: Pore Size Distribution profiles

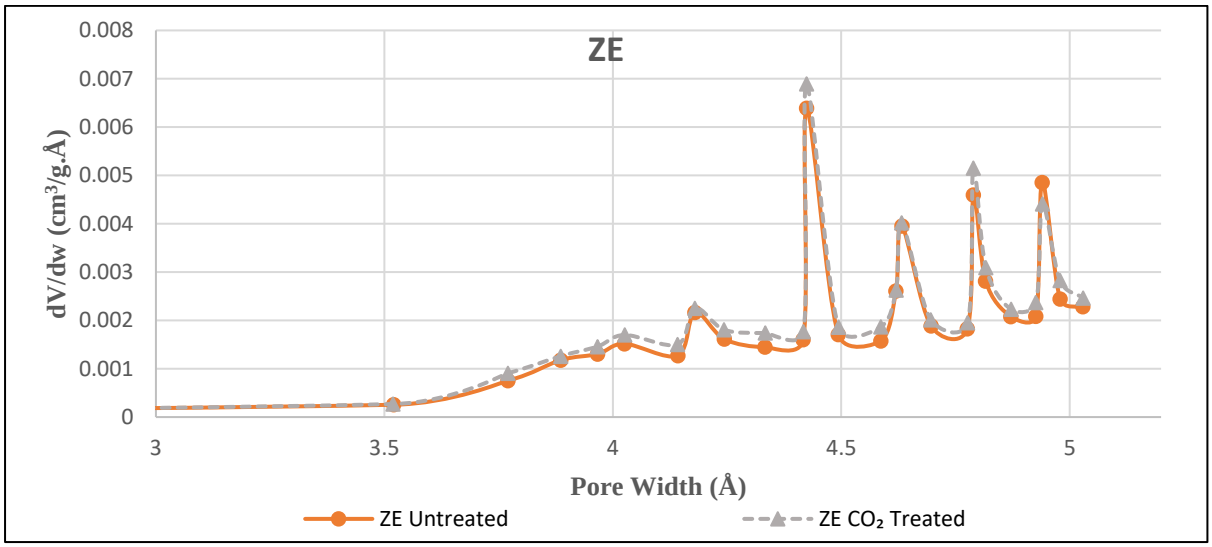

Figure 5.14: ZE untreated and treated samples: Pore Size Distribution profiles

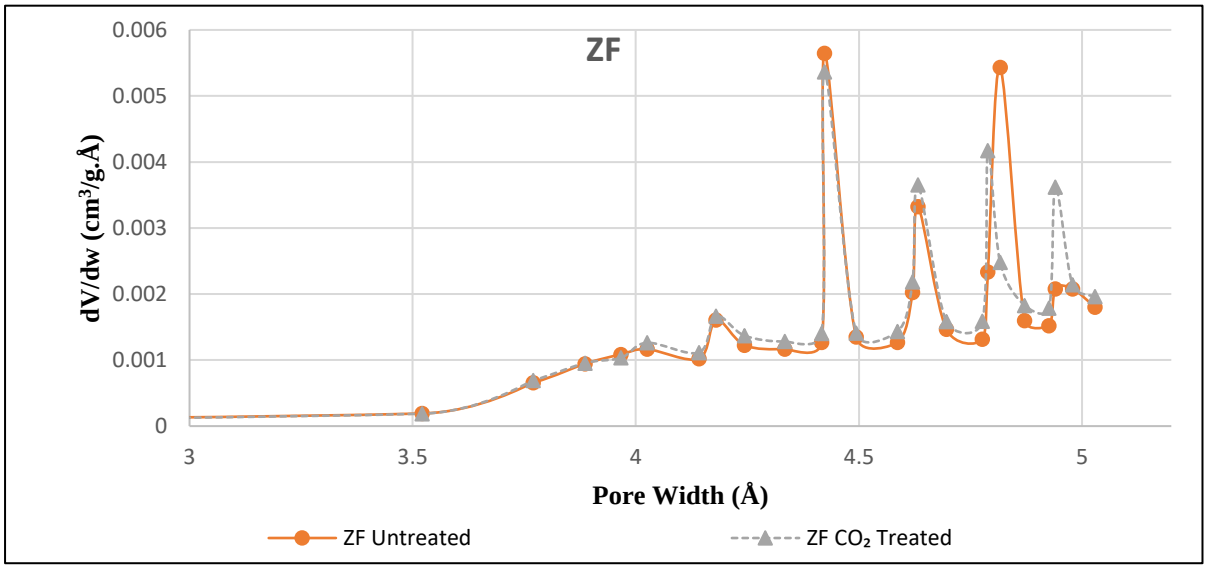

Figure 5.15: ZF untreated and treated samples: Pore Size Distribution profiles

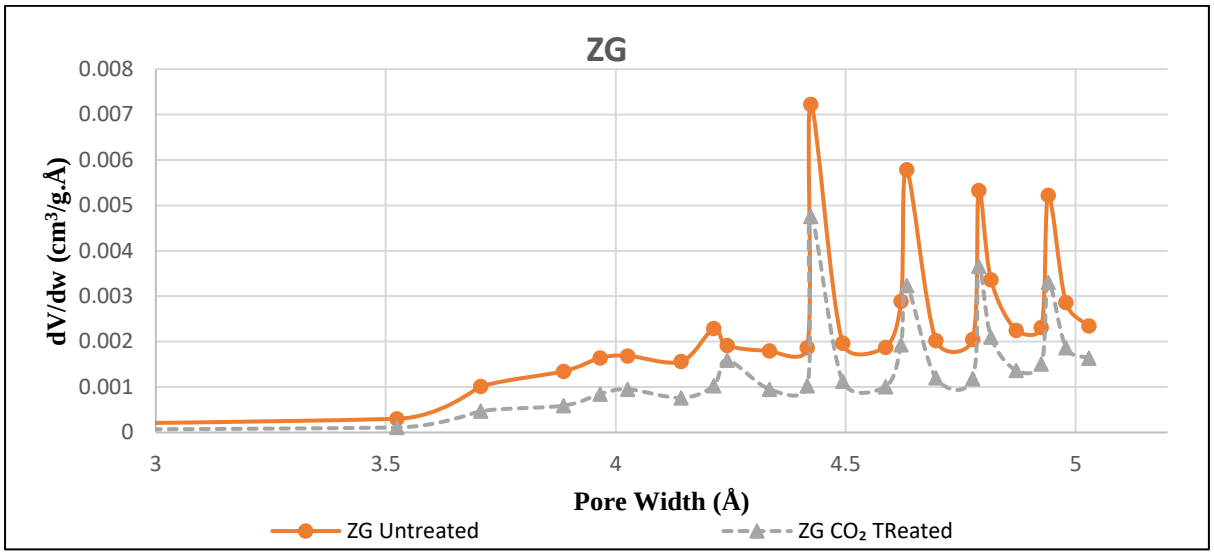

Figure 5.16: ZG untreated and treated samples: Pore Size Distribution profiles

5.3.1.3 Micropore Surface Area and Volume

The D-R and BET micropore surface areas, DA limiting micropore volume and the average pore sizes are evaluated for each of the untreated and $_{sc}CO_2$ treated samples (Table 5.3). The D-R micropore surface area ranged between 13,43 m^2/g (ZE untreated sample) and 20,61 m^2/g (ZC treated A). A reduction in the micropore surface area and limiting micropore volume are reported with an increase in the average pore volume for the ZA sample after CO_2 treatment.

The ZC CO_2 treated A sample displays an increase in D-R micropore surface area of 14% after a month of treatment, but the sample treated for 2 months (ZC CO_2 treated B) shows a slightly lower increase in micropore surface area of 10%.

The D-A micropore volumes for the untreated samples range from 0,02419 cm^3/g (ZF) to 0,04037 m^3/g (ZC). The limiting micropore volume is observed to decrease in the ZC sample after CO_2 treatment. The magnitude of pore volume reduction is observed to be higher after 2 months of treatment (9%) than after 1 month of CO_2 treatment (4%). The ZE sample displays a 9% increase in the limiting pore volume whereas the ZF and ZG samples present an increase of 25% and 8% magnitude, respectively.

Table 5.3: CO_2 Micropore surface area and volume

Sample name	**CO_2 Dubinin-Radushkecich Micropore SA (m^2/g)**	**CO_2 Dubinin-Astakhov Limiting Micropore Volume (cm^3/g)**	**Ave Pore size(Å)**
ZA Untreated	18,27	0,0353	9,79
ZA CO_2 treated	15,357	0,0278	10,7325
ZC Untreated	18,05	0,04037	9,84
ZC CO_2 treated A	20,61	0,03894	10,34
ZC CO_2 treated B	19,83	0,03668	10,60
ZE Untreated	13,43	0,03148	10,70
ZE CO_2 treated	14,98	0,03424	10,44
ZF Untreated	16,79	0,02419	10,54
ZF CO_2 treated	19,19	0,03019	9,73
ZG Untreated	12,70	0,0320	6,36
ZG CO_2 treated	19,798	0,0344	9,6155

The reduction in micropore surface area and adsorption observed in the ZA sample is likely due to the higher levels of precipitation within the sample, indicating higher mineral migration

which then affects the micropore structure due to potential pore clogging (Shi *et al.*, 2019; Wu *et al.*, 2019, 2019). The rest of the samples show an increase in micropore surface area after CO_2 treatment. Increases in micropore surface areas of high quartz and clay content terrestrial shales are reported by Pan *et al.* (2018). Pan *et al.* (2018) also reported decreases in micropore surface area of high quartz and carbonate marine shales after similar treatment. This indicates the complexity of the geochemical $_{sc}CO_2$ -rock interactions during storage and further emphasizes the need for rock specific experimental simulations to be conducted in order to evaluate the resulting changes (Mavhengere *et al.*, 2021). The maturity level of the sedimentary organic matter was proposed to influence the reported pore structure modifications in $_{sc}CO_2$ -rock interactions (Pan *et al.*, 2018; Mavhengere *et al.*, 2021). Lahann *et al.* (2013) and Mouzakis *et al.* (2016) reported increases in BET micropore surface area after treating shale and caprock samples with $_{sc}CO_2$ -Water/brine mixtures. The increase in the average pore volume may be as a result of the clay dissolution in the samples during treatment (Luo *et al.*, 2018).

The increase in average pore size in the ZA, ZC and ZG samples may be a result the influence of clay dissolution in the samples during treatment potentially leading to the reduction in pore volume in the ZA and ZC samples. The dissolution is associated with precipitation of secondary quartz, stilbite and diopside. According to Wu *et al.* (2019) the precipitated minerals have been observed to remigrate and lead to changes in the physical and structural pore system of the resulting treated samples. In fact, Wu *et al.* (2019) reported a complete conversion of the Ordos Basin sandstone after treatment to $_{sc}CO_2$ and brine through clay mineral dissolution, reprecipitation and re migration.

5.3.2 Low Pressure N_2 Gas Adsorption Analyses

Shi *et al.* (2019) reports that the mesoporous size range that is studied through low pressure N_2 gas adsorption mainly exists in clays. Clay dissolution would then be seen through a decrease in the mesopore surface area and pore volume. Clays are known to be the main components of the cement binding the quartz particles together in sandstones (Shi *et al.*, 2019). The low-pressure N_2 gas adsorption results are presented in this section. These are presented in the form of the adsorption- desorption isotherms, the PSD profiles as determined by the application of

the BJH model, as well as the surface parameters analysed through the application of the Langmuir model.

5.3.2.1 N_2 Adsorption-Desorption Isotherms

According to the IUPAC classification, the N_2 adsorption isotherms (Figure 5.17 to Figure 5.21) are all Type IV isotherms (Gudbrandsson *et al.*, 2014; Okolo *et al.*, 2015; Thommes *et al.*, 2015; Mavhengere *et al.*, 2021).

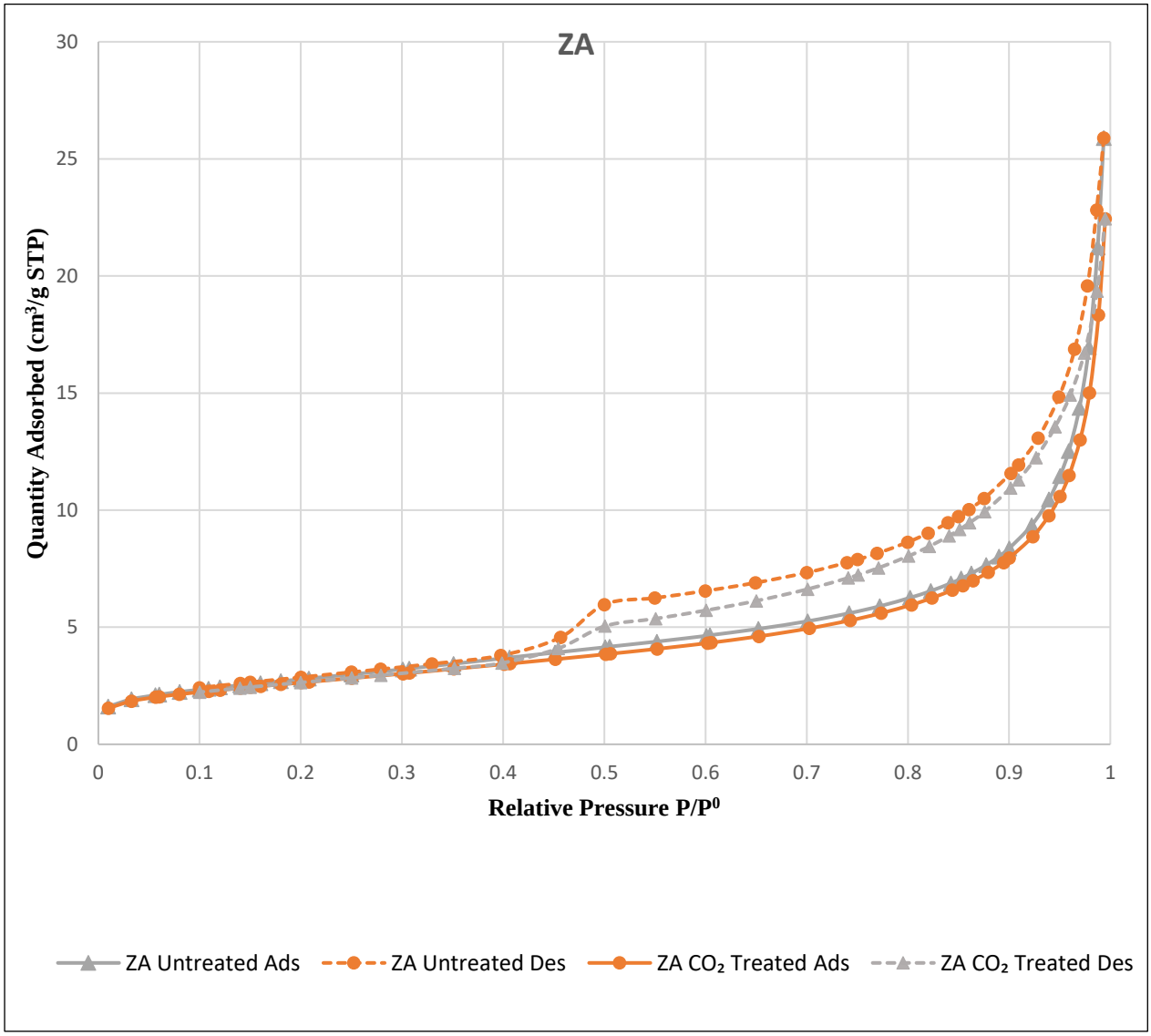

Figure 5.17: ZA untreated and CO_2 treated samples: N_2 Adsorption (Ads)-Desorption (Des) Isotherms.

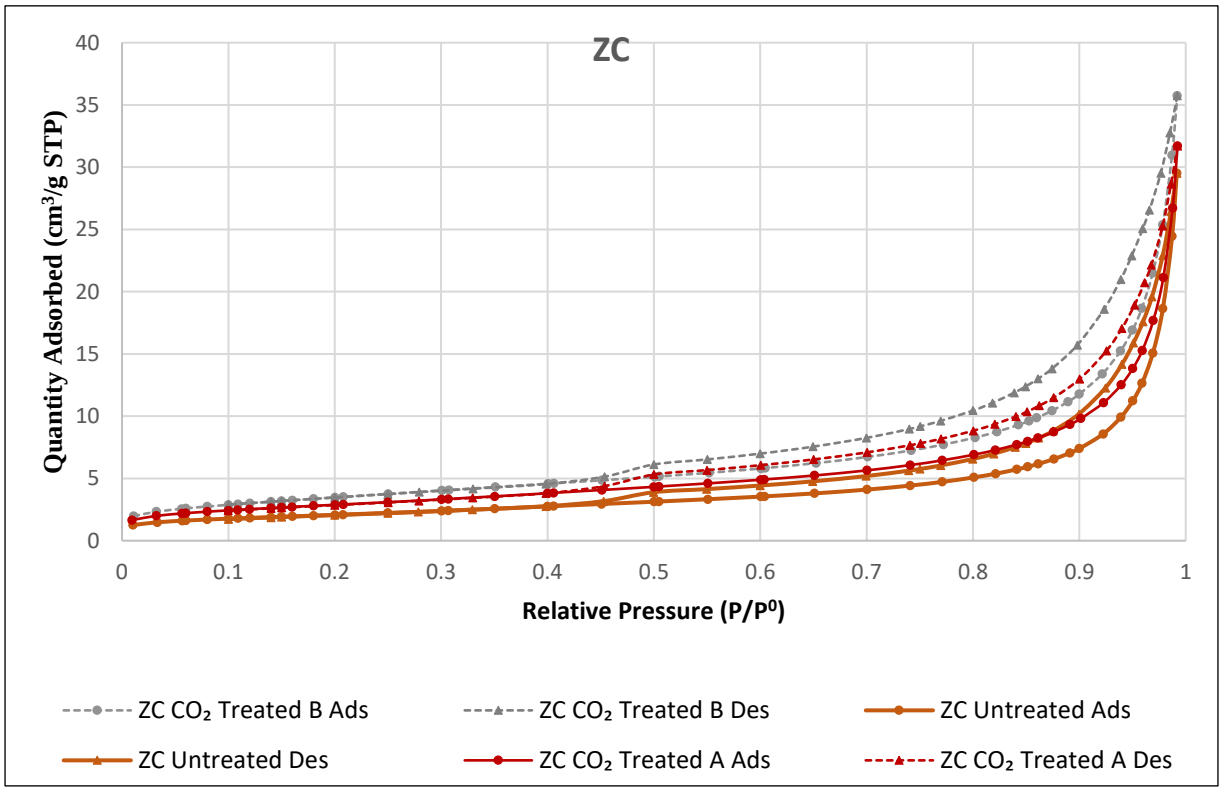

Figure 5.18: ZC untreated and CO_2 treated samples: N_2 Adsorption (Ads)-Desorption (Des) Isotherms.

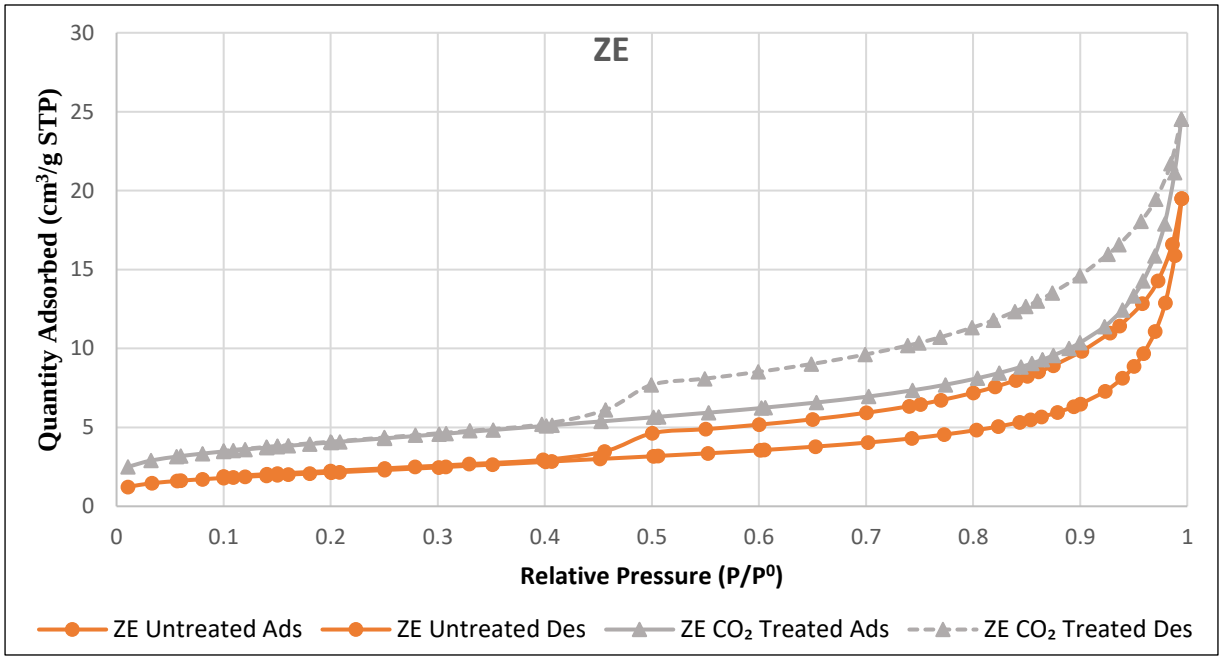

Figure 5.19 ZE untreated and CO_2 treated samples: N_2 Adsorption (Ads)-Desorption (Des) Isotherms.

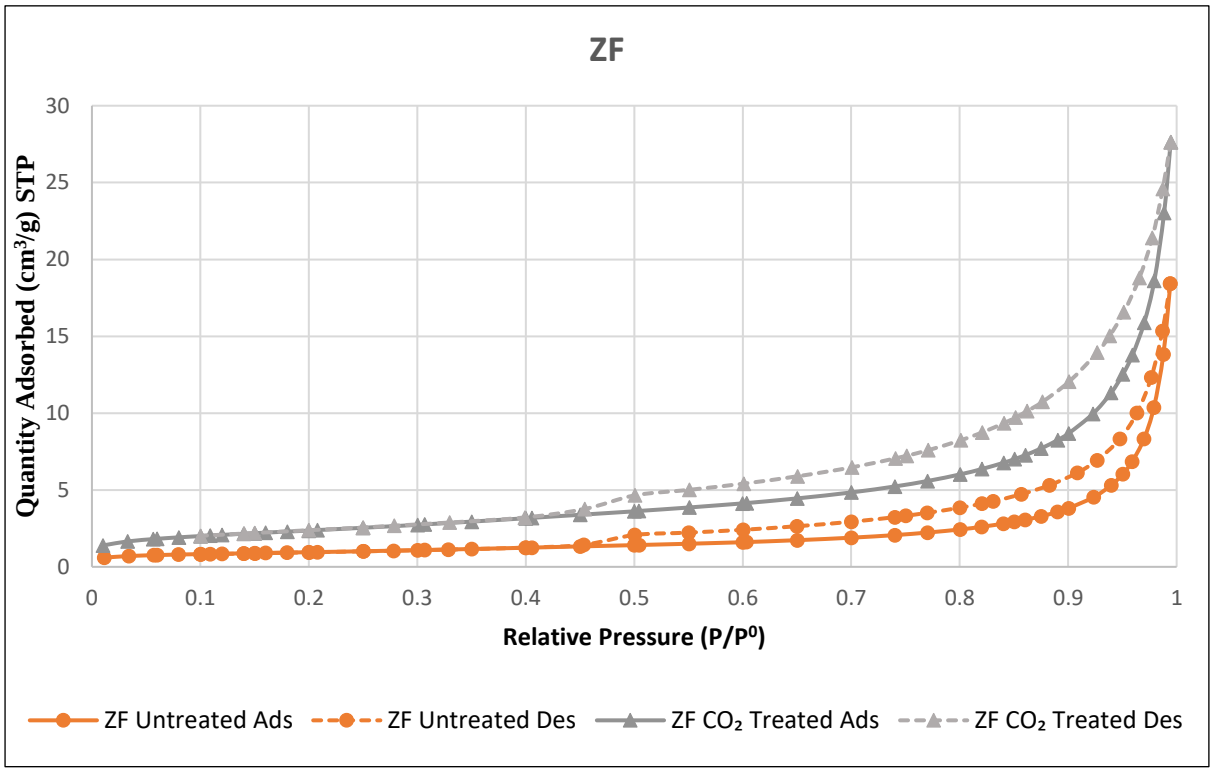

Figure 5.20: ZF untreated and CO_2 treated samples: N_2 Adsorption (Ads)-Desorption (Des) Isotherms.

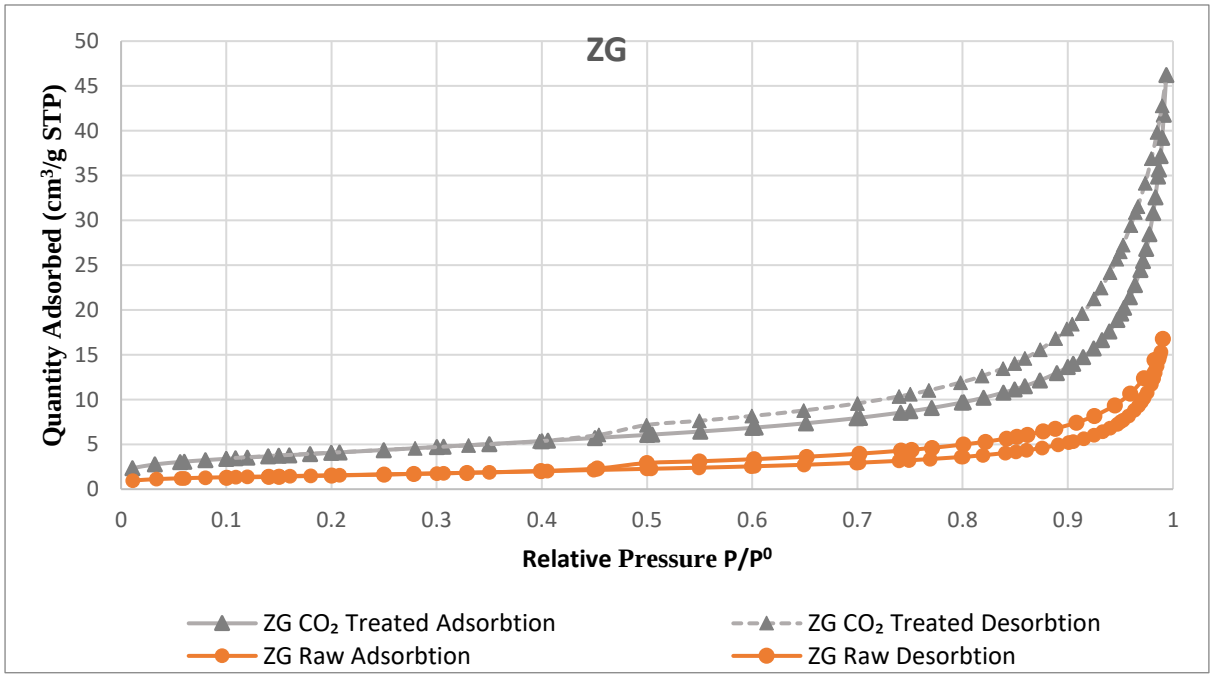

Figure 5.21: ZG untreated and CO_2 treated samples: N_2 Adsorption (Ads)-Desorption (Des) Isotherms.

The hysteresis loop describes the difference between the adsorption and desorption isotherms, its presence indicates slit shaped pores in the analysed samples (Clarkson *et al.*, 2012; Anovitz and Cole, 2015). The hysteresis loops presented by all the samples resemble a H3 hysteresis loops, implying "non-rigid aggregates of plate like particles "in the samples and the presence of macropores which are not entirely filled by pore condensate in the pore network (Thommes *et al.*, 2015; Mavhengere *et al.*, 2021). The tensile strength effect/forced closure phenomenon is also constantly observed at $P/P^0 = 0.45$ for all samples. This, according to Pan *et al.* (2018), is likely due to the hemispherical meniscus instability taking place in pores smaller than 4 nm (40 Å) during the desorption process.

Whilst the ZA sample displays a reduction by 14% in adsorption capacity after $_{sc}CO_2$ treatment, the rest of the samples display a contrary increase in adsorption capacity after treatment. The greatest increase in maximum adsorption capacity of 220% which is reported in the ZG sample, whilst the ZC sample shows the lowest increase of 12%. The highest adsorption capacity is observed in the ZG CO_2 treated sample at 46.21 cm^3/g at the maximum relative pressure. This may most likely be due to the reported calcite dissolution in the sample. This is followed by the ZC CO_2 treated sample at 35.74 cm^3/g. The ZF and ZF treated samples present the lowest adsorption capacities, at 18.42 cm^3/g and 19.50 cm^3/g, respectively. These samples therefore adsorb CO_2 at lower rate in comparison to the other samples. The adsorption profile for the 1 month treated sample (ZC treated A) is observed to lie in between the 2 months treated sample and the untreated sample, indicating progressive increase in adsorption capacity from the 1-month treatment period to two months.

Yin *et al.* (2016) describes the steep increase in adsorption capacity at the higher relative pressure values (0.9-1.0) as an implication of micro- and mesopore dominance. The shapes of the isotherms are not observed to change after treatment. Similar findings have been reported by Yin *et al.* (2016) after exposing shale samples to supercritical CO_2 .

The capillary condensation in the core sample mesopores is believed to produce the adsorption-desorption hysteresis loops observed on each of the samples, indicating the presence of open pores (Pan *et al.*, 2018). According to Sing *et al.* (1985), Chalmers *et al.* (2012), and Yin *et al.* (2016), the pore morphology may be evaluated using the shape of the hysteresis loop. It may therefore be inferred that $_{sc}CO_2$ -water treatment of the ZG core sample influenced changes the

shape of the meso- and macropores as it presents a slight hysteresis shape change after treatment.

5.3.2.2 Mesopore and Macropore Size Distribution Profiles

Unimodal profiles are observed in the N_2 PSD profiles of all samples determined by the application of the BJH model (Figure 5.22 to Figure 5.26). Similar observations were made by Shi *et al.* (2019) and Kuila and Prasad (2013) whilst studying sandstone pore structures using N_2 gas adsorption. Over 60% of the mesopore volume is accounted for in the 20 to 200 Å pore diameter range. The ZA sample shows a reduction in the pore volume peak between 18 and 28 Å. This reduction in pore volume in this range may be a result of the destabilization of dissolution pores during treatment with $_{sc}CO_2$ -water, as similarly observed by Shi *et al.* (2019) after treating rock samples with $_{sc}CO_2$ -brine mixtures. Shifts in the observed peaks to lower pore diameters are observed after $_{sc}CO_2$ -water treatment in the remaining core samples. The 2 month treated core samples (ZC, ZE, ZF and ZG) consistently show an increase in pore volume throughout the mesopore diameter profiles. The one month treated sample (ZC treated A), shows a correlation in pore volume with the untreated sample for pore diameters $\geq$ 450 Å. The increase in porosity at mesoscale due to $_{sc}CO_2$ -water treatment in rock formations have been observed by other researchers in the field (Rimmelé *et al.*, 2010; Goodman *et al.*, 2019; Shi *et al.*, 2019). This is mainly attributed to the formation of macropores and/ or micro fractures along grain boundaries where clays are dissolved (Shi *et al.*, 2019). According to Shi *et al.* (2019), the loss of clay minerals is likely to increase pore structure connectivity and weaken the strength of the sandstone.

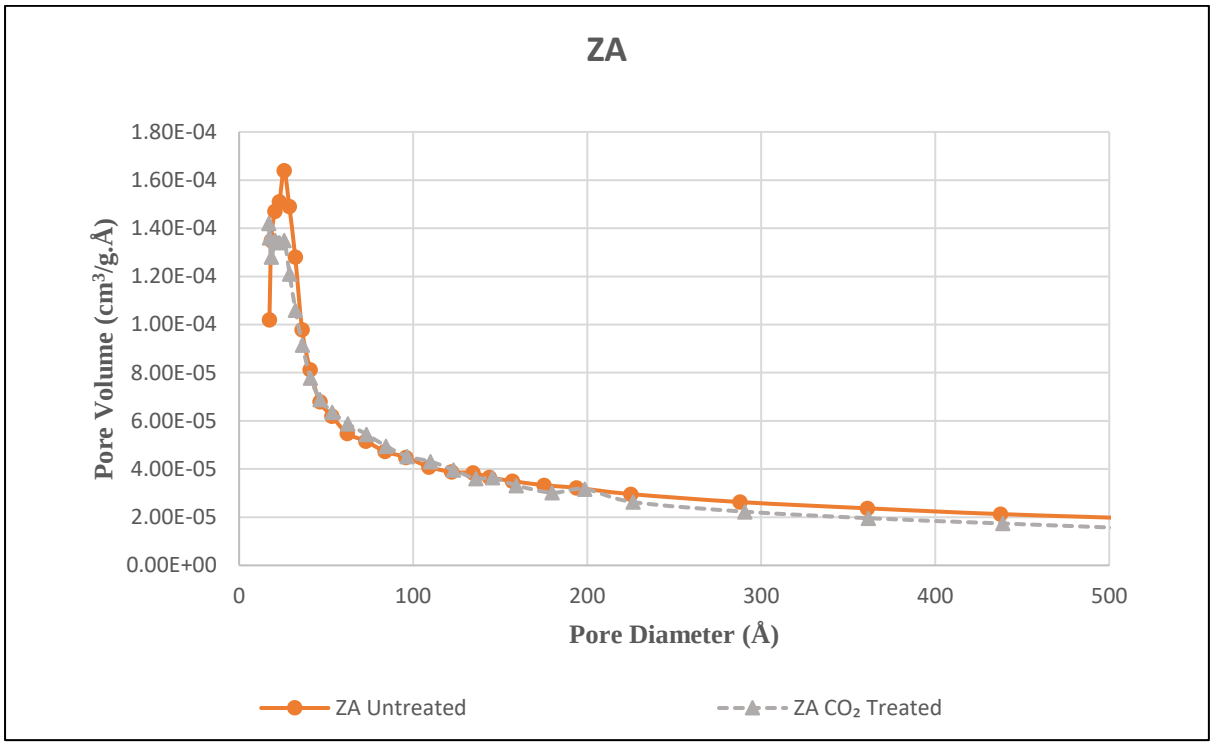

Figure 5.22: ZA untreated and CO_2 treated samples: N_2 mesopore PSD evaluated using the BJH model.

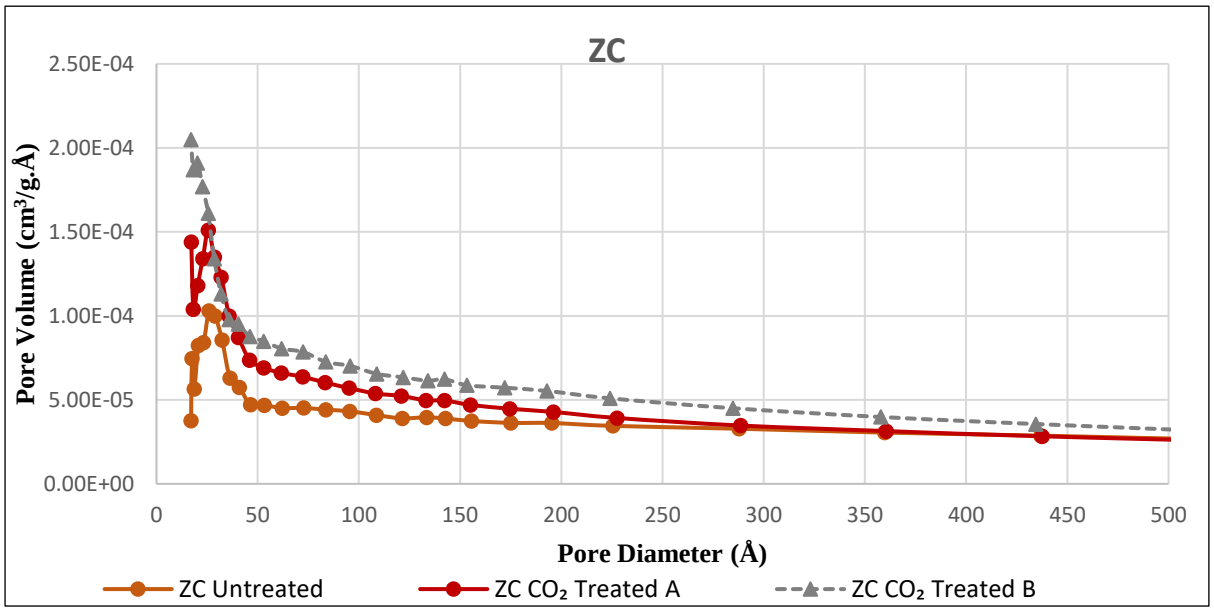

Figure 5.23: ZC untreated and CO_2 treated samples: N_2 mesopore PSD evaluated using the BJH model.

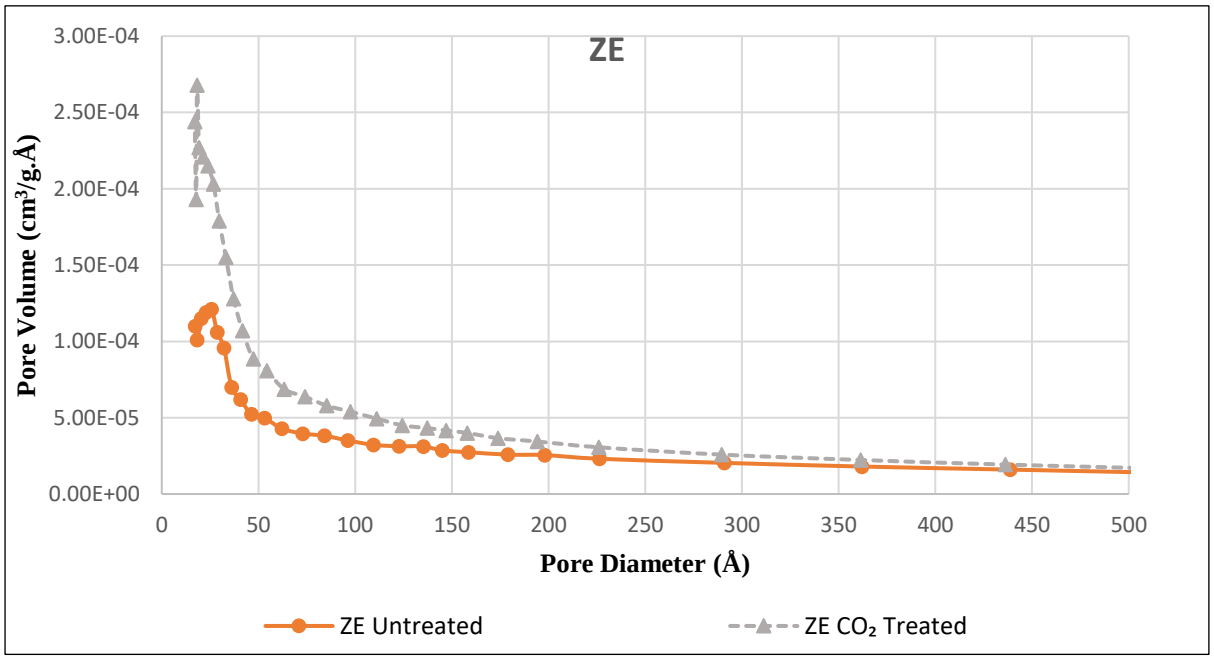

Figure 5.24: ZE untreated and CO_2 treated samples: N_2 mesopore PSD evaluated using the BJH model.

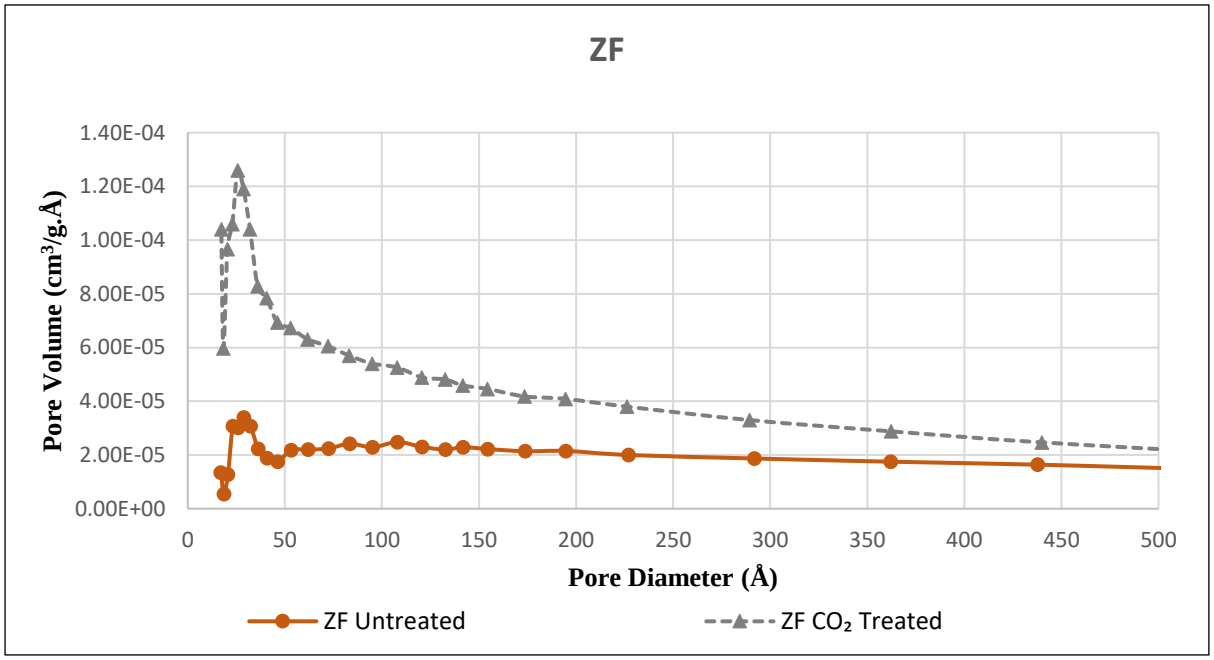

Figure 5.25: ZF untreated and CO_2 treated samples: N_2 mesopore PSD evaluated using the BJH model.

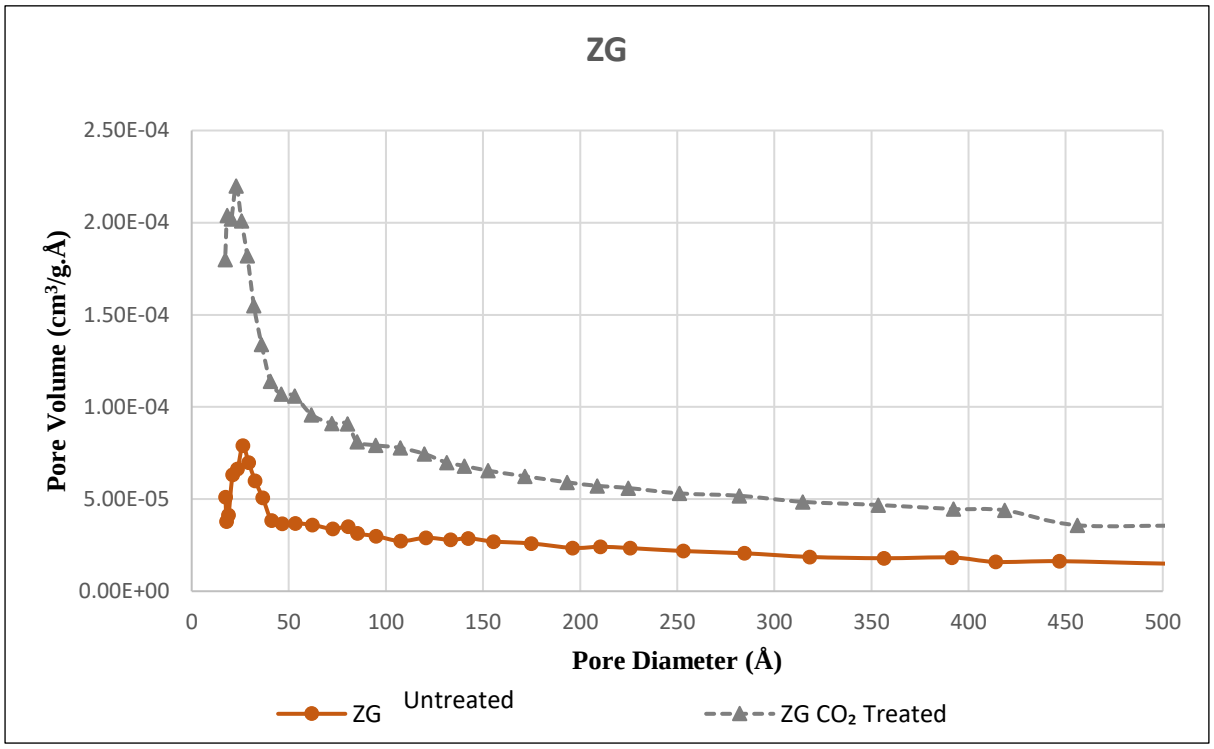

Figure 5.26: ZG untreated and CO_2 treated samples: N_2 mesopore PSD evaluated using the BJH model.

The pore volume profiles for the core samples at macropore diameter ranges of 500 Å to 1800 Å are presented in Figure 5.27 to Figure 5.31. A consistent low pore volume profile is observed for the ZA CO_2 treated and ZC CO_2 treated A sample post $_{sc}CO_2$ -water treatment. The ZC treated A and B samples and the ZE treated sample present higher PSD profiles of up to a certain pore size of 450, 950 and 1750 Å respectively. Higher PSD profiles are however observed for the ZF and ZG treated samples throughout the profile range in comparison to the respective untreated samples. This demonstrates a possible limitation of the influence of $_{sc}CO_2$ -water interactions on the sample macropore structure for these core samples. Similar findings are reported by Shi *et al.* (2019) after exposing sandstone samples to $_{sc}CO_2$ -brine mixtures.

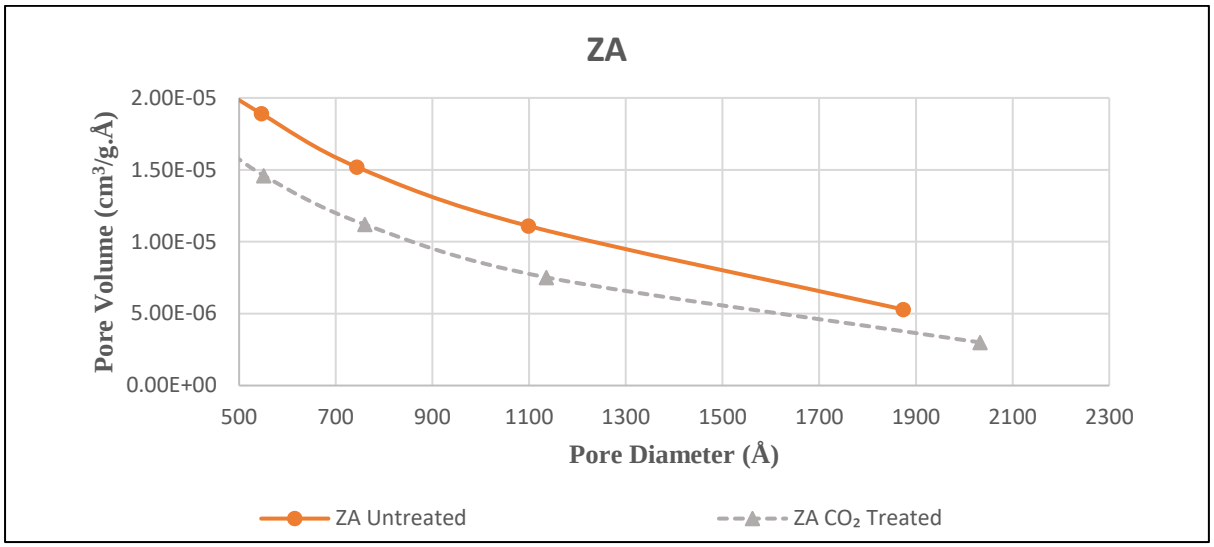

Figure 5.27: ZA untreated and CO_2 treated samples: N_2 macropore PSD evaluated using the BJH model.

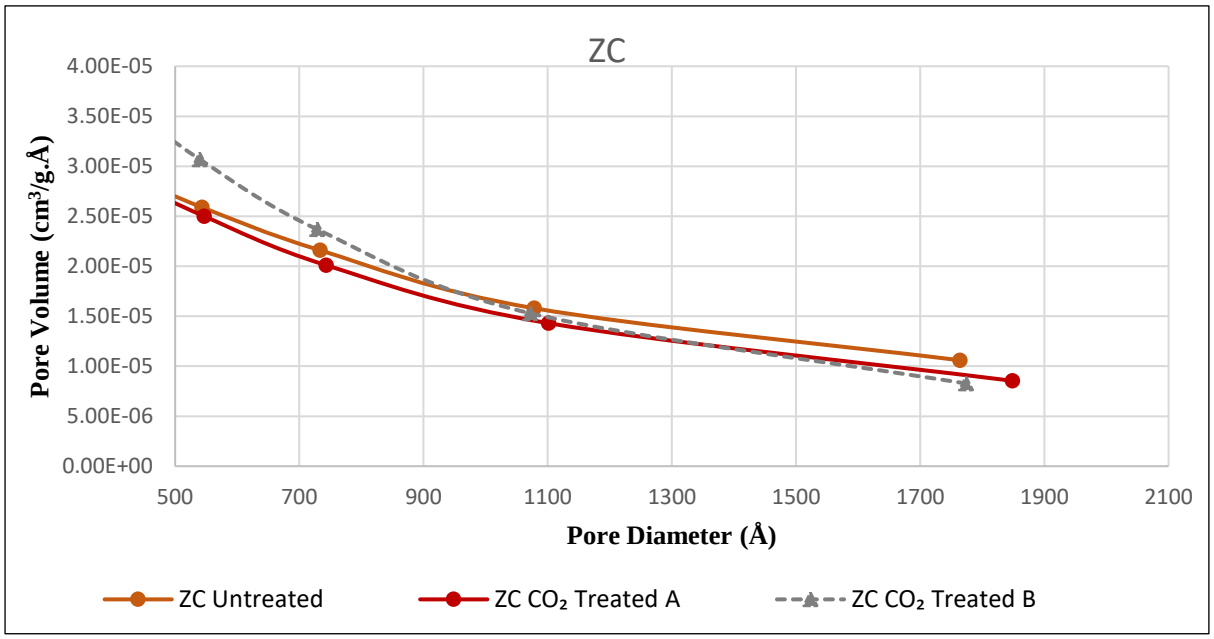

Figure 5.28: ZC untreated and CO_2 treated samples: N_2 macropore PSD evaluated using the BJH model.

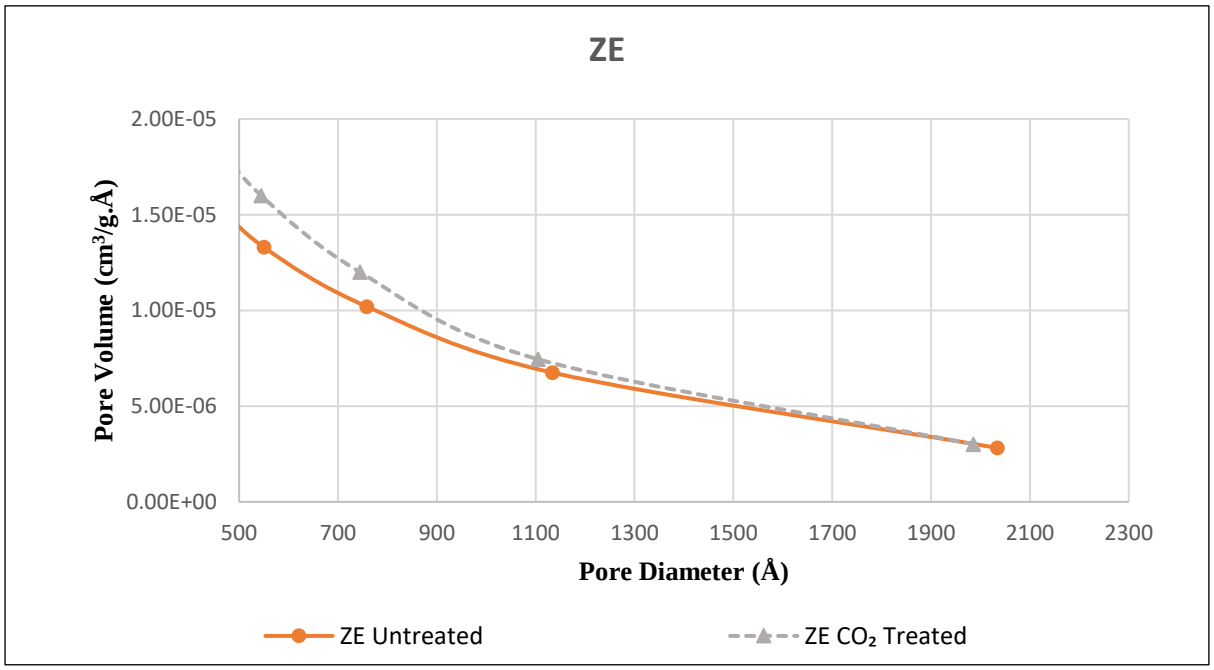

Figure 5.29: ZE untreated and CO_2 treated samples: N_2 macropore PSD evaluated using the BJH model.

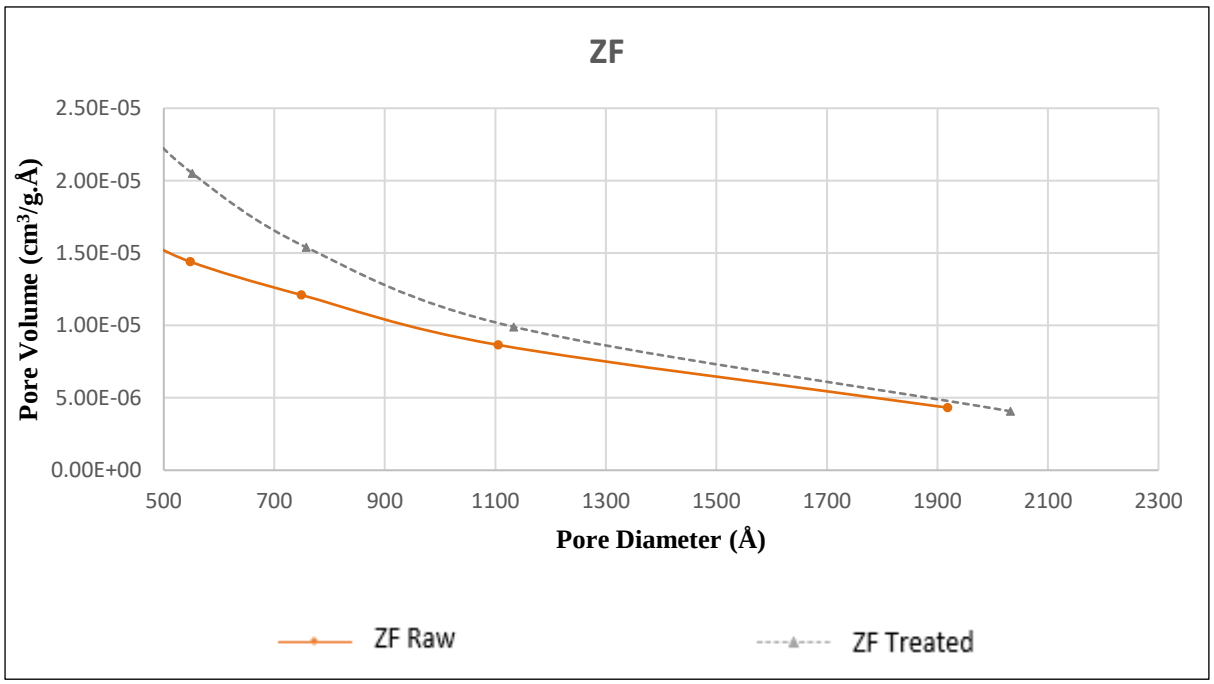

Figure 5.30: ZF untreated and CO_2 treated samples: N_2 macropore PSD evaluated using the BJH model.

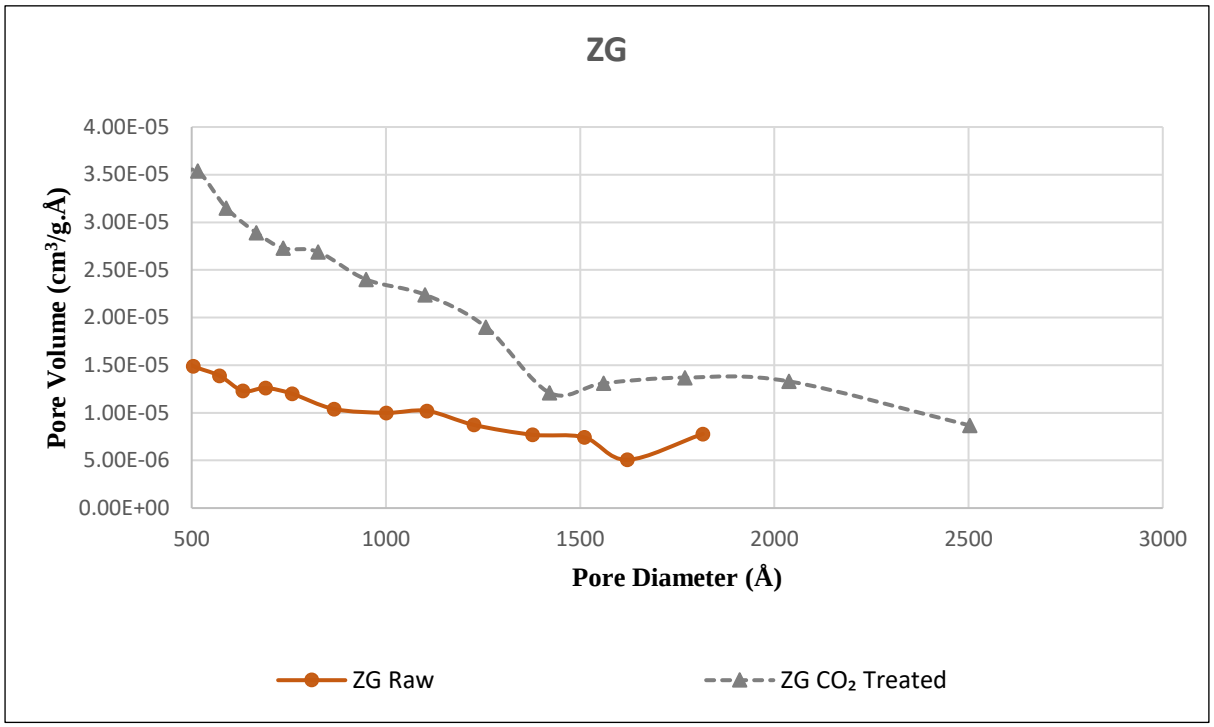

Figure 5.31: ZG untreated and CO_2 treated samples: N_2 macropore PSD evaluated using the BJH model.

5.3.2.3 Mesopore and Macropore Surface Area Parameters

The BET and Langmuir surface area data are outlined in Table 5.4. Both parameters present minor reduction of ≤9% in surface area after $_{sc}CO_2$ -water treatment of the ZA sample. Increases in the surface area of up to 180% are observed in the other samples after $_{sc}CO_2$ -water treatment. The ZC sample presents a 26% and 54% increase in BET surface area after 1 month and 2 months of $_{sc}CO_2$ treatment, respectively. A 49% and 72% increase are observed in the Langmuir surface area for the respective samples. The ZE sample displays a 55% increase in BET mesopore and macropore surface area along with an 83% increase in Langmuir mesopore and macropore surface area. A 115% and 150% increase in BET and Langmuir surface areas respectively is reported in the ZF sample. The highest increase in surface area is observed in the ZG sample at 155% for the BET surface area and 180% for the Langmuir surface area.

Table 5.4: N_2 BET and Langmuir Surface Areas

Sample	N_2 BET m^2/g	N_2 Langmuir m^2/g
ZA Untreated	3.40	14,72
ZA CO_2 treated	3.12	13.83
ZC Untreated	3,17	10,91
ZC CO_2 treated A	4,00	15,23
ZC CO_2 treated B	4,87	18,76
ZE Untreated	2,59	11,37
ZE CO_2 treated	4,03	20,87
ZF Untreated	1,63	5,04
ZF CO_2 treated	3,52	12,51
ZG Untreated	2,10	7,76
ZG CO_2 treated	5,42	21,70

5.4 Key Findings

5.4.1 Mineral Alterations due to $_{sc}CO_2$ -water Treatment

Mineral alterations were observed as determined by XRD analyses in line with other studies in the field such as (Dai *et al*. 2020; Gudbrandsson *et al.* 2014 and Wu *et al.* 2019). The dissolution

of clays and/or carbonates (smectite and calcite) was predominantly observed in all samples in line with findings reported by Credoz *et al.* (2009). Smectite and calcite dissolution was observed in the ZA sample, and the dissolution of plagioclase and precipitation of quartz was also reported. The ZC CO_2 treated A and B samples demonstrated slight calcite and plagioclase dissolution, and a slightly higher dissolution rate was observed on the ZC treated A sample than the ZC treated B sample. Smectite precipitation was found in the ZC CO_2 treated samples; more smectite was observed on the ZC CO_2 treated B sample than in the ZC CO_2 treated B sample. The ZE sample merely presents slight dissolution of smectite which is present in the sample in small composition (2,6%). Slight precipitation of plagioclase is also noted, whilst the rest of the minerals are insignificantly altered. The ZF sample presents complete calcite dissolution accompanied by slight smectite dissolution and negligible stilbite and diopside precipitation. The ZG sample presented notable smectite and orthoclase dissolution. This was accompanied by calcite, stilbite and plagioclase precipitation and minimal changes to the quartz content. The different alterations observed in the samples outline the complexity of the $_{sc}CO_2$ -water treatment influences on specific rock samples. Plagioclase and clay dissolution and precipitation in particular plays a significant role in geological sequestration (Zhang *et al.*, 2009).

5.4.2 **Effects on the Surface Chemistry**

The effect of $_{sc}CO_2$ -water treatment on the surface chemistry of the different rock samples through FTIR was investigated. The general overall observation is the reduction in peak intensity after $_{sc}CO_2$ -water treatment. The lower peak intensities were observed in similar studies on CO_2 treated samples such as Yin *et al.* (2016) and Goodman *et al.* (2019). All samples showed the presence of water, varying trace levels of organic matter, silica, and calcite. The ZA sample, complements the XRD results showed calcite dissolution after $_{sc}CO_2$ -water Treatment. The ZC samples did not present any significant changes in the surface functional groups, similar to XRD results, only subtle changes in peak intensities were observed. The ZC treated A sample presented stronger peak intensities as compared to the untreated and ZC treated B sample. No notable changes on the surface functional groups were observed on the ZE sample. The ZF sample presents multiple differences in the untreated and treated sample spectra. Organic matter C-H and C-N functional groups are not reported in the treated sample

despite being identified in the untreated sample, implying organic matter dissolution. The ZG sample presented minimal changes in surface chemistry. Applications of the FTIR technique has demonstrated its ability to satisfactorily characterise sediments such as those expected in the samples under study (Herbert *et al.*, 1992; Bishop *et al.*, 1996; Reig *et al.*, 2002; Theodosoglou *et al.*, 2017). According to Yin *et al.* (2016) and Lu *et al.* (2015), surface chemistry alterations may influence rock adsorption behaviour of CO_2 and other gases.

5.4.3 Effects on Textural Properties

Changes in micropore, mesopore and macropore structure properties are observed in the studied samples. The micropore structure was analysed through the application of low-pressure CO_2 adsorption on untreated and CO_2 treated samples. Different observations are reported for the five samples studied. The ZA sample demonstrates a reduction in CO_2 adsorption capacity, micropore volume and surface area following treatment. Contrary observations are reported for the remaining four core samples. The average pore size is observed to increase for the ZC and ZG samples whilst minor decreases are observed in the ZE and ZF samples. The increase in micropore average pore size is attributed to calcite and or smectite and orthoclase dissolution (Luo *et al.*, 2018; Wu *et al.*, 2019).

The mesopore and macropore structures were investigated by the application of N_2 gas adsorption. All samples presented Type IV isotherms, which are typical for mesoporous solids (Clarkson *et al.*, 2012). Increases in mesopore and macropore adsorption are observed in all samples except for the ZA sample. The influence of $_{sc}CO_2$ -water treatment on the samples is observed to vary within the five core samples. An increase in pore volume is observed throughout the pore diameter profiles (20-2300 Å) for the ZF and ZG samples, whilst for the ZC and ZE samples, the increase in pore volume is observed up to a certain pore diameter within the profile, thereafter, lower pore volumes are observed in the CO_2 treated samples in comparison to the respective untreated samples. A consistent increase in mesopore and macropore surface area is observed for all core samples except for the ZA sample, which reports a decrease in mesopore and macropore surface area after $_{sc}CO_2$ -water treatment. The trapping mechanisms at pore structure scale are reported to account for up to 97% of the residually trapped CO_2 during storage (Cui *et al.*, 2017; Mavhengere *et al.*, 2021). The flow pattern and storage capacity are particularly vulnerable to pore structure changes (Dai *et al.*,

2020). Since the pore volume is defined as a measure of its storage capacity (Krohn, 1988), for the same sample a higher storage capacity is obtained with a larger pore volume (Moosavi *et al.*, 2014; Campos *et al.*, 2015; Mavhengere *et al.*, 2021). An increase in storage capacity in the samples studied as a result of $_{sc}CO_2$ treatment except for the ZA sample is therefore implied.

Variations in the PSD profile peaks were observed in the untreated and treated samples, indicating pore structure changes which are similarly attributed to clay and carbonate mineral dissolution (Rimmelé *et al.*, 2010; Pan *et al.*, 2018; Goodman *et al.*, 2019; Shi *et al.*, 2019).

6 CHAPTER 6: EFFECTS OF $_{sc}CO_2$ - SO_2 -WATER TREATMENT

The current chapter outlines the results of the characterisation tests conducted on the Zululand Basin ZC and ZG samples following treatment and seeks to determine the effects of SO_2 in the gas stream during the experiments. Simulated CO_2 storage experiments were conducted on the ZC and ZG core samples using a 99% CO_2 and 1% SO_2 gas mixture. A water-rock ratio of 23:1 as used previously was used at the typical reservoir conditions of 180 bar and 70 ºC for the ZC sample, and 120 bar and 43 ºC for the ZG sample. Both samples were treated for a duration of 2 months. An attempt to conduct the same experiment was made on the ZF sample. However, the mixture was observed to be unstable at the experimental conditions, leading to reactor rapture disc failure due to the over pressurisation of the reactor which occurred prematurely at 1 week. Due to equipment failure, this particular test could not be repeated on the rest of the samples.

6.1 Mineral Alterations as determined by XRD.

The introduction of SO_2 is expected to lead to the generation of stronger sulphuric acid in the gas-water medium stream. This in turn is expected to influence the chemical reactions taking place during treatment/ CO_2 storage tests. Mineral alterations in sandstone samples after treatment with SO_2 contaminated streams has been studied by researchers in the field through the application of XRD (Xu and Van Deventer, 2002; Wollenweber *et al.*, 2010; Pearce *et al.*, 2015, 2015; Yin *et al.*, 2016). Dawson *et al.* (2015) studied the dissolution of Berea sandstone in CO_2 -SO_2 -brine water mixtures by evaluating the changes in the XRD results before and after treatment. Pearce *et al.* (2015) used XRD to determine mineral alterations after exposing sandstone samples to $_{sc}CO_2$-SO_2-water mixtures.

The XRD results for the ZC and ZG samples present different mineralogical alterations after $_{sc}CO_2$ -SO_2 -water treatment as shown in

Table 6.1. An increase in quartz composition after the sandstone samples were exposed to $_{sc}CO_2$ -SO_2 - water is observed. Plagioclase composition is observed to decrease in the ZC sample whilst an observation of an increase of the same mineral in the ZG sample post $_{sc}CO_2$ -SO_2 - water treatment is seen. Smectite composition is observed to increase in the ZC sample. The same mineral is observed to decrease in the ZG sample post $_{sc}CO_2$ -SO_2 -water treatment. The calcite dissolution is reported in the ZC sample, whilst its precipitation is observed in the ZG

sample. The ZC sample also demonstrates gypsum precipitation after CO_2 -SO_2 treatment. Orthoclase is found to decrease in the ZG CO_2 - and CO_2 -SO_2 treated samples, the decrease in orthoclase is less in the latter. The effective changes in mineral composition are further analysed in Sections 6.1.1 to 6.1.2.

Table 6.1: ZC and ZG core sample XRD results pre and post $_{sc}CO_2$ -SO_2 -water treatment with comparison to CO_2 treated samples.

Sample	Quartz (wt.%)	Plagioclase (wt.%)	Smectite (wt.%)	Calcite (wt.%)	Pyrite (wt.%)	Stilbite (wt.%)	Diopside (wt.%)	Gypsum (wt.%)	Orthoclase (wt.%)
ZC Untreated	44,1	44,7	1,0	3,5	0,4	3,6	2,7	0,0	0,0
ZC CO_2 treated A	47,1	40,8	1,3	2,8	0,4	4,6	3,1	0,0	0,0
ZC CO_2 treated B	47,5	42,5	2,5	1,7	0,4	2,7	2,8	0,0	0,0
ZC CO_2 -SO_2 treated	49,1	28,6	11,8	0,0	0,8	4,9	2,3	2,5	0,0
ZG Untreated	21,5	46,0	22,2	0,0	0,0	2,0	0,0	0,0	8,3
ZG CO_2 treated	22,3	50,5	16,3	2,9	0,0	4,8	0,0	0,0	3,2
ZG CO_2 -SO_2 treated	26,1	53,4	12,1	2,3	0,0	0,0	0,0	0,0	6,2

6.1.1 **ZC**

The ZC CO_2 -SO_2 treated sample is compared to the untreated sample (apparent variation) and the CO_2 treated B sample to determine the mineral alterations arising from the introduction of SO_2 into the CO_2 stream. The effective variation is also evaluated using Equation (8) to eliminate the effect of calcite dissolution on the resulting apparent concentrations. The XRD composition variations are summarised Figure 6.1. The apparent effects of $_{sc}CO_2$ -SO_2 – water treatment indicate a precipitation of quartz and smectite at 11% for each mineral. Dissolution of plagioclase is observed at 36% and calcite at 100%. Formation of gypsum is observed in the

ZC CO_2 -SO_2 treated sample. Precipitation of gypsum after calcite dissolution is reported in literature (Bouchelaghem, 2010; Wilke, 2012; Farquhar *et al.*, 2015; Pearce *et al.*, 2015, 2015, 2015; Melliti, 2021; Alimi *et al.*, n.d.; Booth *et al.*, n.d.; Wilkins *et al.*, n.d.). SO_2 dissolution in water results in the formation of sulphurous acid which in turn could react with oxygen to form sulphuric acid (Equation (10)).

$$SO_2 + H_2O \leftrightarrow H_2SO_3 + \frac{1}{2}O_2 \rightleftarrows H_2SO_4 \rightleftarrows 2H^+(aq) + SO_4^{2-}\ (aq) \qquad (10)$$

Calcite ions produced through dissolution in acidic environments upon treatment to sulphuric acid may lead to the rapid precipitation of gypsum as outlined by Equation 11 (Pearce *et al.*, 2015).

$$Ca^{2+} + SO_4^{2-} + 2H_2O \rightarrow CaSO_4.2H_2O \qquad (11)$$

Traces of pyrite precipitation are noted after CO_2 -SO_2 treatment. Comparable results were observed by Pearce *et al.* (2015) studying alterations in ferroan carbonates after treatment to SO_2 -CO_2 mixtures under CO_2 sequestration conditions.

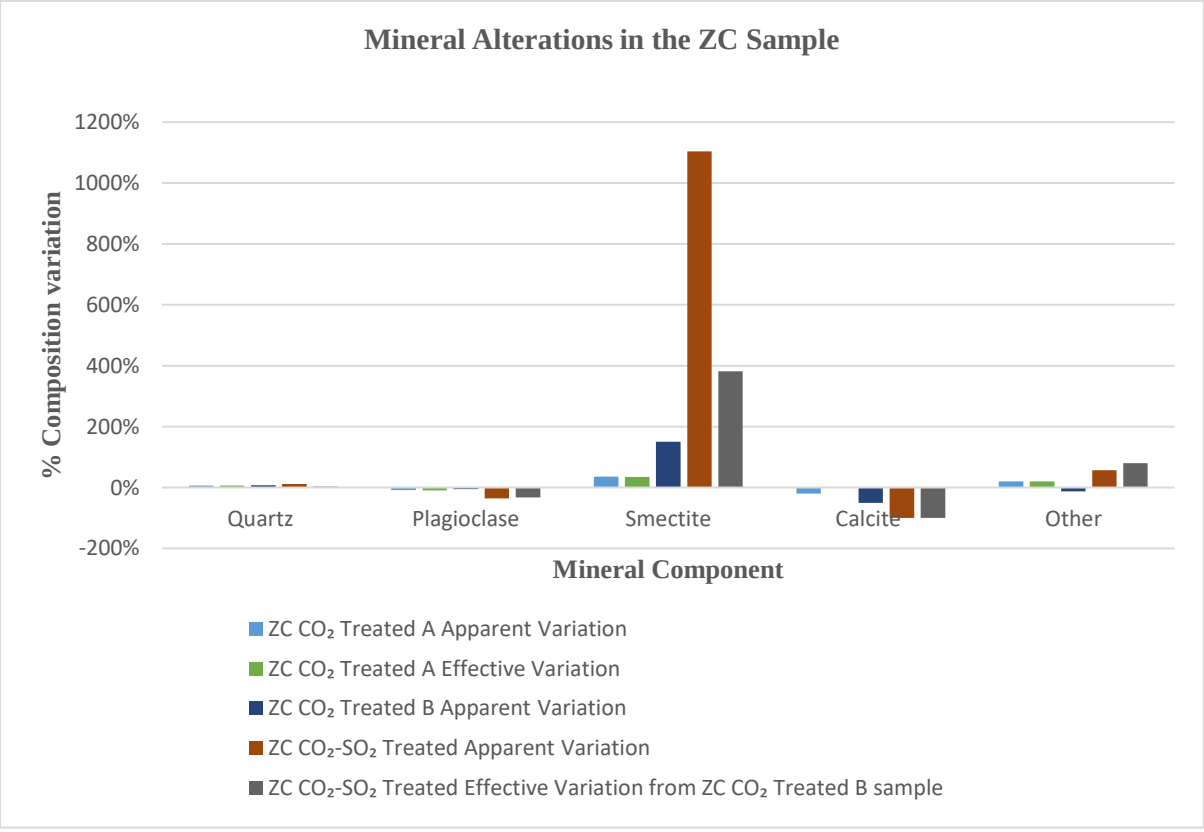

Figure 6.1: ZC and ZG mineral alterations as evaluated by XRD.

When compared to the ZC treated B sample, the ZC CO_2-SO_2 treated sample presents an additional 3% increase in quartz precipitation, whilst smectite precipitation increases by a significant 382%. Dissolution of plagioclase is higher by 33% in comparison to the CO_2 treated B sample, and an 80% increase in the precipitation of other minor minerals is demonstrated mostly due to the precipitation of gypsum. Water/rock interactions simulated by the conversion of calcium to gypsum is reported to impact negatively impact the pore structure by decreasing sample porosity (Knauss *et al.*, 2005; Pearce *et al.*, 2015). Upon considering the effect of calcium dissolution in the sample, a 4 % increase in the dissolution rate is observed for the plagioclase whilst a 4% decrease in the precipitation rate is observed in the other minerals. As observed in Chapter 5, mineral dissolution and precipitation leads to pore structure changes in agreement with Farquhar *et al.*, 2015 and Wu *et al.*, 2019. Pearce *et al.* (2015) also observed plagioclase dissolution in rock samples after treatment to CO_2 -SO_2 -water-rock mixtures. Mavhengere *et al.* (2021) and Gudbrandsson *et al.* (2014) acknowledged the rising interest in plagioclase dissolution due to its potential role in CO_2 storage. Yin *et al.*(2016), reports that Ca, Mg and Al rich silicates such as plagioclase are expected to have a huge potential for mineralization trapping due to their dissolution capacity in carbonic acid.

According to Dawson *et al.* (2016), plagioclase (albite) dissolves into solution after SO_2 introduction due to the resulting lower pH values of 1-3. The dissolution of silicates is enhanced at the lower pH values (Wilke *et al.*, 2012; Dawson *et al.*, 2015). It may be implied that the introduction of SO_2 into the CO_2 stream could increase the rock's dissolution capacity due to the formation of lower pH in the formation water.

6.1.2 **ZG**

Precipitation of quartz is observed in the ZG sample at 21% apparent variation from the untreated sample (Figure 6.2). A 16% increase in plagioclase is observed after CO_2 -SO_2 treatment. The increases in quartz and plagioclase are notably higher than the alterations reported in the CO_2 treated sample by 17% and 6%, respectively. Smectite is observed to dissolve during CO_2 treatment. The rate of dissolution is increased by a further 26% upon the introduction of SO_2. Calcite precipitation is observed likely as a result of the dissolution of smectite. Other minor minerals such as orthoclase and stilbite are shown to further reduce by 23% in composition after $_{sc}CO_2$ -SO_2 -water treatment.

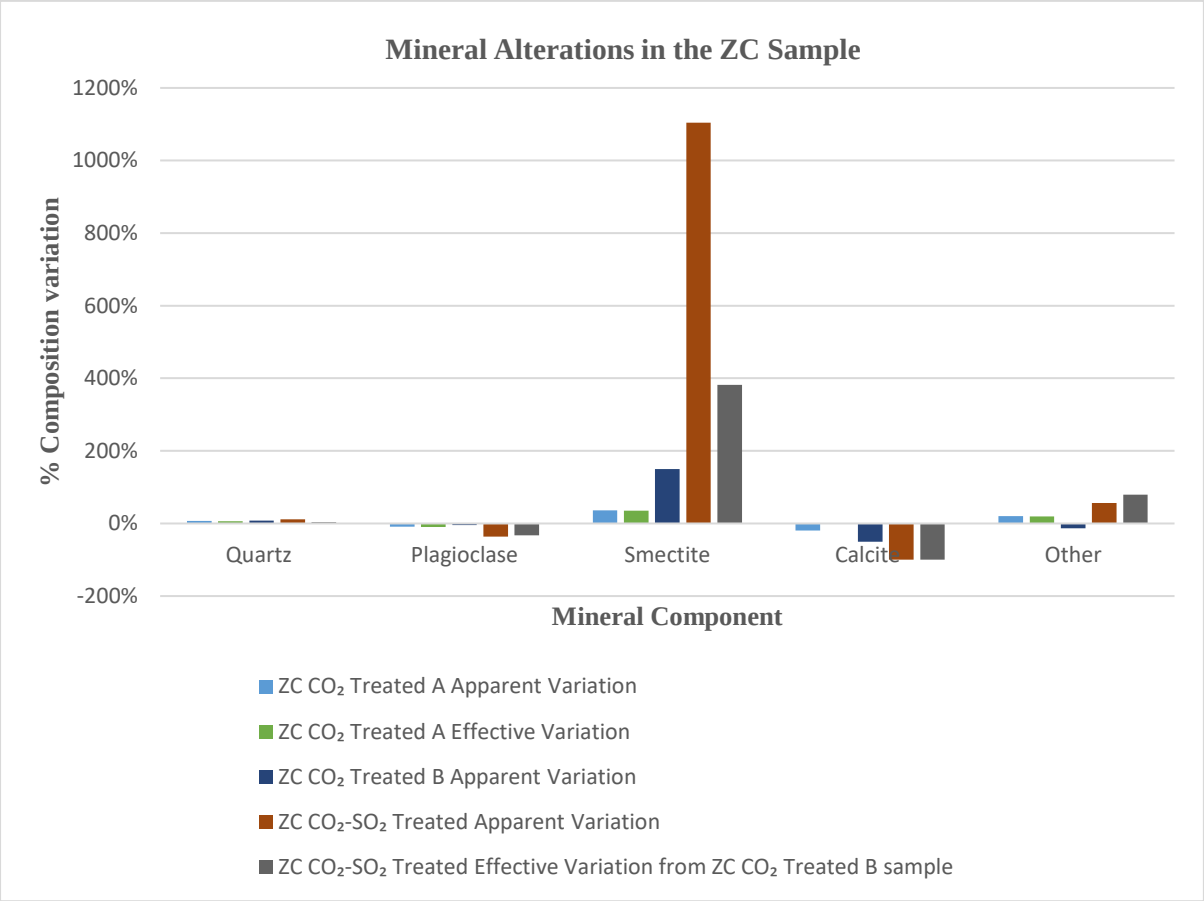

Figure 6.2: ZC mineral alterations as evaluated by XRD.

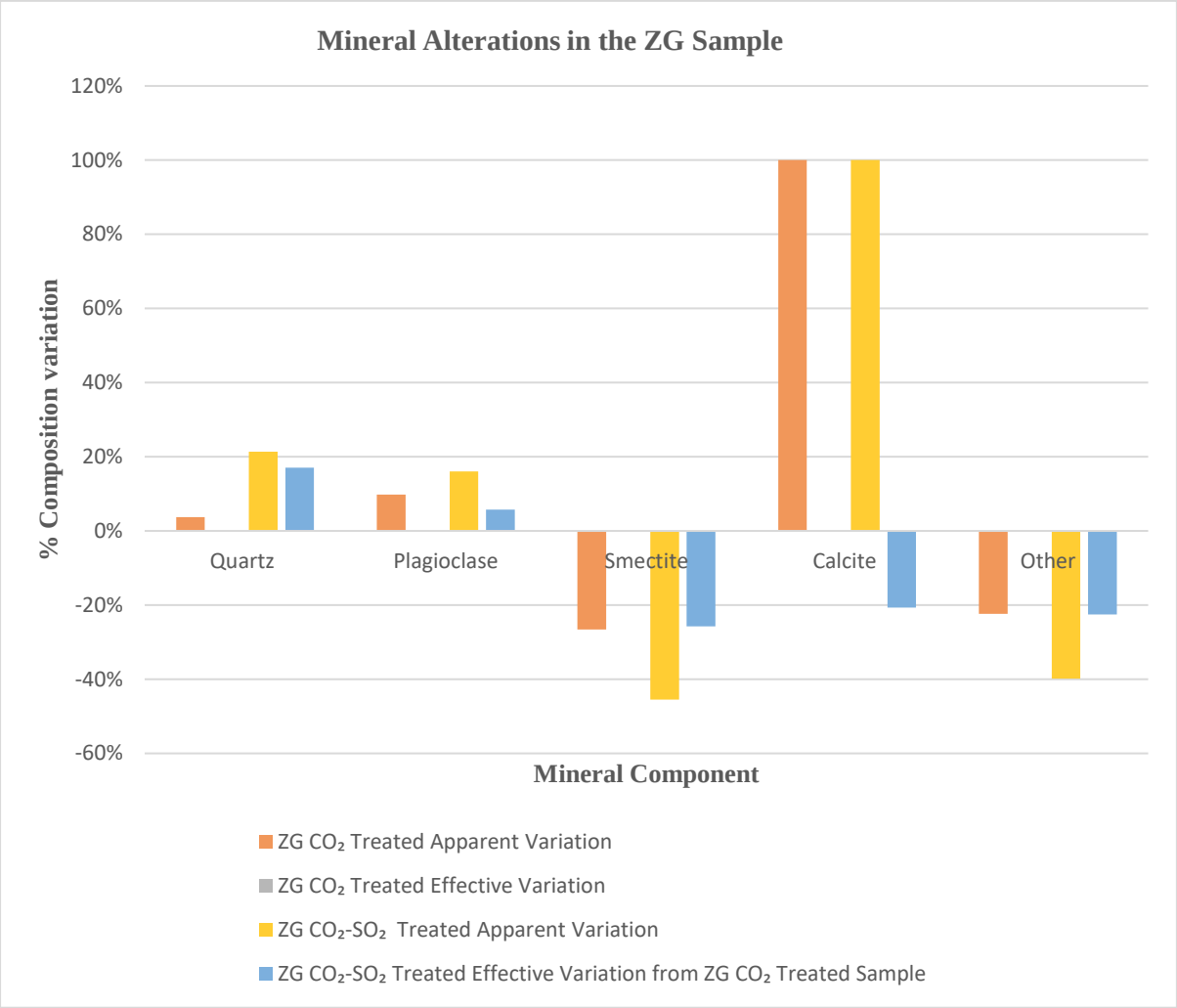

Figure 6.3: ZG mineral alterations as evaluated by XRD**.**

It may be suggested that the resulting increase in plagioclase increases the potential for mineralisation trapping in the sandstone core sample, attributing to an increased CO_2 adsorption capacity of the rock in the long term. Secondary precipitation of quartz is reported in literature after rock treatment to sequestration conditions (Koenen *et al.*, 2011; Zhang *et al.*, 2020; Mavhengere *et al.*, 2021). This is mainly as a result of the dissolution of silicate minerals in both samples (Dai *et al.*, 2020; Zhang *et al.*, 2020). The dissolution of stilbite is observed in the ZG CO_2-SO_2 treated sample; this differs from the ZG CO_2 treated sample results that indicates precipitation. The dissolution of stilbite is reported in literature under similar conditions (Xu and Van Deventer, 2002; Rosenbauer *et al.*, 2005).

6.2 Effects on Surface Chemistry using FTIR.

Studies such as those conducted by Glezakou *et al.* (2012) have demonstrated successful application of FTIR analyses in evaluating the interactions of SO_2 with mineral samples under sequestration conditions. This approach is applied in this study to evaluate the effects of SO_2 introduction into the CO_2 stream. Changes in chemical functional groups as a result of the introduction of 1% SO_2 in the CO_2 stream are outlined in this section. FTIR spectra are reported in Figure 6.4 and Figure 6.5, the variations in the spectra are summarised in Table 6.2. Sections 6.2.1 and 6.2.2 report on the results and observations obtained.

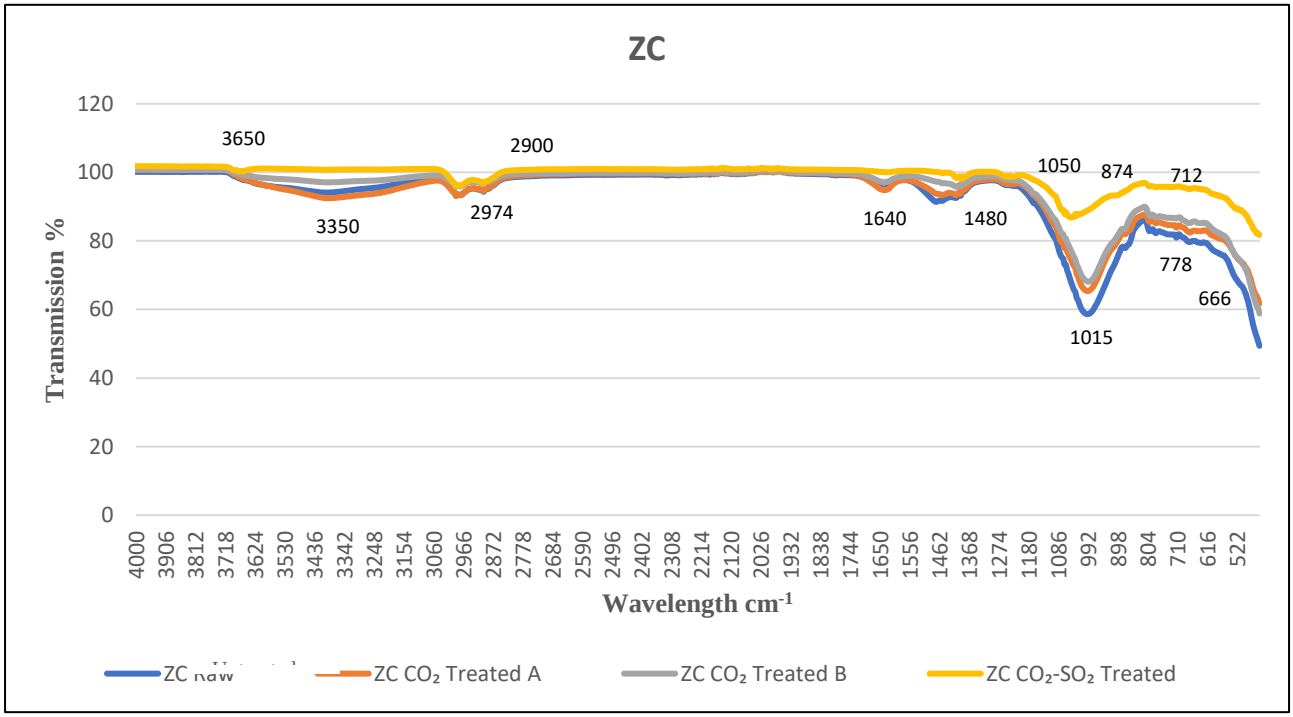

Figure 6.4: Functional Group Changes as evaluated by FTIR in ZC.

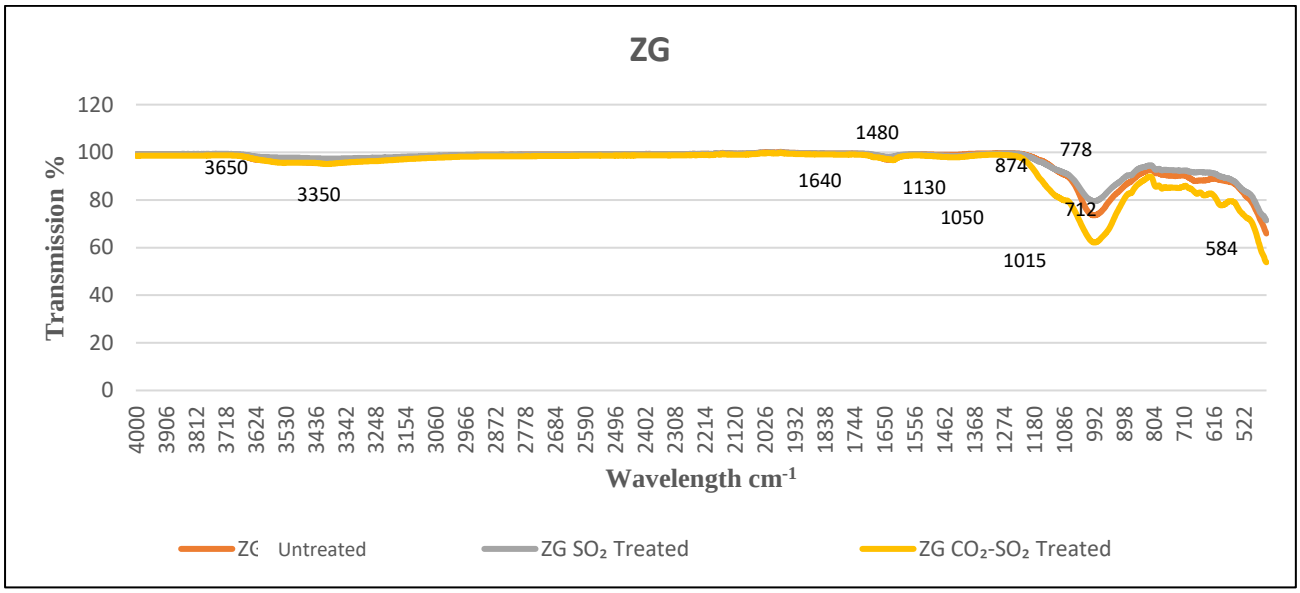

Figure 6.5: Functional Group Changes as evaluated by FTIR in ZG.

6.2.1 **ZC**

The ZC sample shows a reduction in peak intensity throughout the spectra profile after $_{sc}CO_2$ - SO_2 -water treatment (Figure 6.4). An elimination of the 3350 and 1640 peaks from the CO_2 SO_2 treated sample spectra is observed. This represents the absence of the OH functional group stretching and deformation vibrations. The calcite peak at 712 cm^{-1} and 874 cm^{-1} is eliminated in line with the XRD results. The SiO stretching bond at 1015 cm^{-1} is observed to significantly reduce in intensity with a more prominent peak being observed at 1050 cm^{-1}. A more distinct variation in the spectra is observed after CO_2 -SO_2 treatment as compared to CO_2 treatment.

Table 6.2: FTIR Peak Assignments.

Wave-number cm-1	ZC			ZG			Functional group assignments
	Untreated	CO_2 treated B	CO_2 - SO_2 treated	Untreated	CO_2 treated	CO_2-SO_2 treated	
3650	X	X		X	X	X	OH, stretching for water
3350	X	X	X	X	X	X	
2974	X	X	X				C-H stretching of aliphatic bonds (aldehydes and alkanes)
2900	X	X	X				
2000				X	X		
1640	X	X		X	X	X	OH, deformation of water
1480	X	X	X	X	X	X	CH deformation
1424	X	X	X				COH bending vibrations
1224	X	X	X				C-N bond vibrations
1130				X	X		C-C stretching modes/ Si-O stretching Vibrations in silicates
1050			X				C-O stretching modes in organic compounds/ Si (Al)-O stretching vibrations in feldspars
1000-1015	X	X	X	X	X	X	Si (Al)-O stretching vibrations
874	X	X			X	X	Calcite bending (Out of Plane)
778	X	X	X	X	X	X	SiO stretching for quartz
712	X	X			X	X	Calcite Bending (In plane)
666	X	X	X	X	X	X	SiO (perpendicular mode for quartz)
580-600						X	FeO/ O-Si (Al)-O bond vibrations for example in feldspars

Sources:(Allen *et al.*, 1994; Jiang and Xu, 1995; Nakamura *et al.*, 1996; McCarthy *et al.*, 1997; Reig *et al.*, 2002; Kloprogge and Frost, 2004; Lane, 2007; Schuttlefield *et al.*, 2007; Rubasinghege and Grassian, 2013; Thompson *et al.*, 2013; Loring *et al.*, 2015; Theodosoglou *et al.*, 2017; Goodman *et al.*, 2019; Yuvashree and Balavijayalakshmi, 2019; Kutchko *et al.*, 2020; Klima *et al.*, n.d.)

6.2.2 **ZG**

The ZG sample presents a more intense FTIR profile after $_{sc}CO_2$ -SO_2 treatment (Figure 6.5). More peaks are demonstrated after $_{sc}CO_2$ -SO_2 treatment at 1050 cm^{-1} and 584 cm^{-1}. The peak at 1050 cm^{-1} represents the presence of Si (Al)-O functional groups in silicates, and the more pronounced peak is likely due to the increased precipitation of plagioclase in the sample. The peak observed at 584 cm^{-1} indicates the presence of O-Si (Al)-O bond functional groups in in feldspars and may be due to the higher content of plagioclase and orthoclase in the sample in comparison to the untreated and $_{sc}CO_2$ treated samples. The calcite peak is observed only in the ZG CO_2 treated and ZG CO_2 -SO_2 treated samples as indicated by the mineral alterations discussed in Chapter 5.

6.3 Effects on Physical Characteristics though LPGA

The physical properties of the two core samples were similarly evaluated by the application of LPGA technique. This section outlines the pore structure changes observed in the CO_2 -SO_2 -water treated samples.

6.3.1 **ZC Low Pressure CO_2 Adsorption**

A notable increase in CO_2 adsorption capacity after $_{sc}CO_2$ -SO_2 -water treatment was observed in the ZC sample as indicated by the adsorption isotherm (Figure 6.6). A 12% increase in the maximum quantity adsorbed is reported after $_{sc}CO_2$ -water treatment and a 40% increase is observed in the $_{sc}CO_2$ -SO_2 -water treated sample at P/P^0=0.03. The PSD profile reported is similar to the one observed after CO_2 treatment for 2 months (Figure 6.7). The $_{sc}CO_2$ -SO_2 treated sample merely shows a higher pore volume in the 3-5 Å range. It is important to note that the shift in PSD peaks from 4.24 Å in the untreated and CO_2 treated A sample to 4.18 Å in the CO_2 treated B sample is also maintained in the CO_2 -SO_2 treated sample. This indicates similar pore structure changes in both samples despite the addition of SO_2 into the CO_2 stream for treatment. The D-R and BET micropore surface areas show notable increases of 31% and 20%, respectively in the ZC CO_2 -SO_2 treated sample, as noted in Table 6.3, compared to both the ZC untreated and CO_2 treated B samples. The micropore volume is observed to remain constant whilst the average pore size increases by 16%. Changes in the micropore structure of sandstones is likely due to carbonate and clay dissolution as indicated by the FTIR and XRD

analyses, in agreement with other researchers in the field (Yin *et al.*, 2016; Luo *et al.*, 2018; Zhu *et al.*, 2018; Dai *et al.*, 2020).

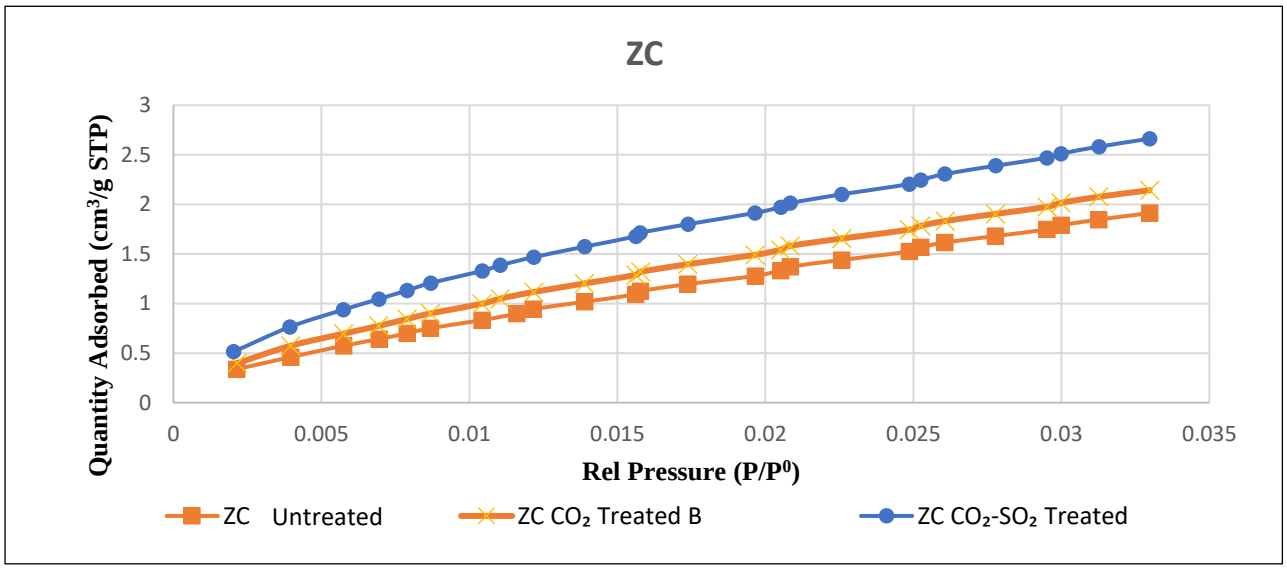

Figure 6.6: ZC untreated, CO_2 treated and CO_2 -SO_2 treated samples: CO_2 adsorption isotherms.

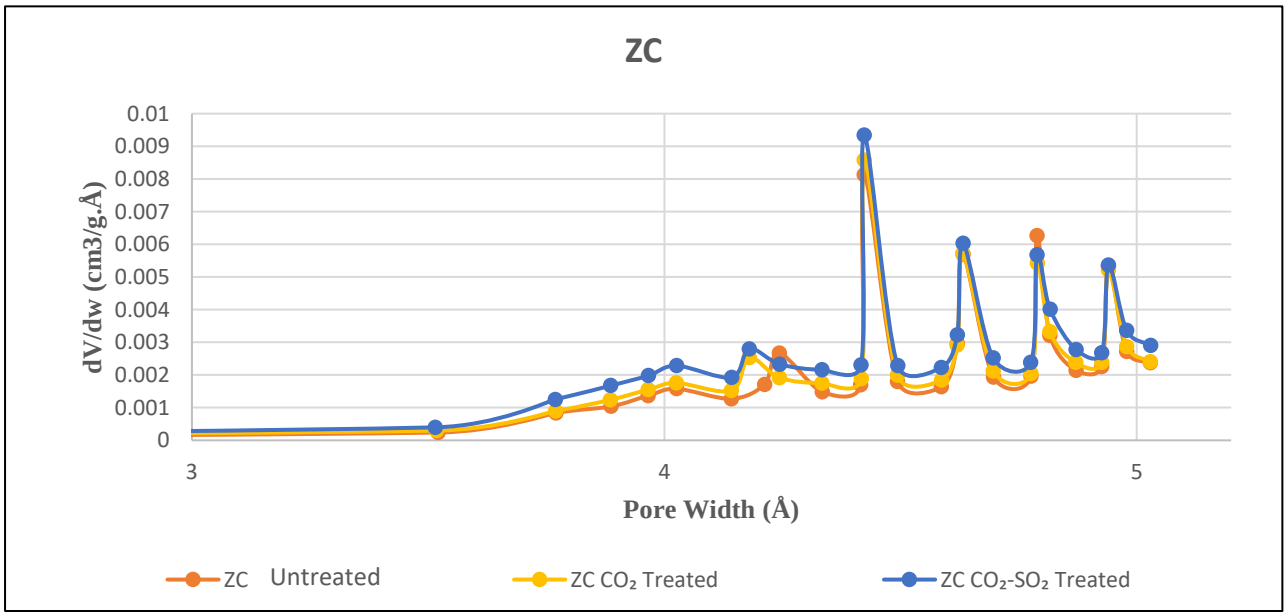

Figure 6.7: ZC untreated, CO_2 treated and CO_2 -SO_2 treated sample: H-K micropore PSD Profiles.

Table 6.3: ZC CO_2 Adsorption Pore Parameters

Sample	**CO_2 Dubinin-Radushkecich Micropore SA (m^2/g)**	**CO_2 Dubinin-Astakhov Limiting Micropore Volume (cm^3/g)**	**CO_2 BET S/A (m^2/g)**	**Ave Pore size(Å)**
ZC Untreated	18,05	0,040	14,23	9,84
ZC CO_2 treated A	20,61	0,03894	15,46	10,34
ZC CO_2 treated B	19,83	0,037	14,79	10,60
ZC CO_2 -SO_2 treated	23,82	0.037	17,14	11,37

6.3.2 ZC Low Pressure N_2 Adsorption

The N_2 adsorption and desorption isotherm profiles present minimal changes to the mesopore and macropore structure of the ZC sample following $_{sc}CO_2$ -SO_2 -water treatment (Figure 6.8). The adsorption and desorption profiles of the ZC CO_2 -SO_2 treated sample closely mimic those of the ZC untreated sample. A 19% decrease in the maximum quantity adsorbed is observed after $_{sc}CO_2$ -SO_2 -water treatment at P/P^0 =1. The hysteresis shape is maintained throughout most of the adsorption and desorption profile, only a minor shape changes is observed at a relative pressure of 0,96 - 1, indicating minor morphological changes on the sample.

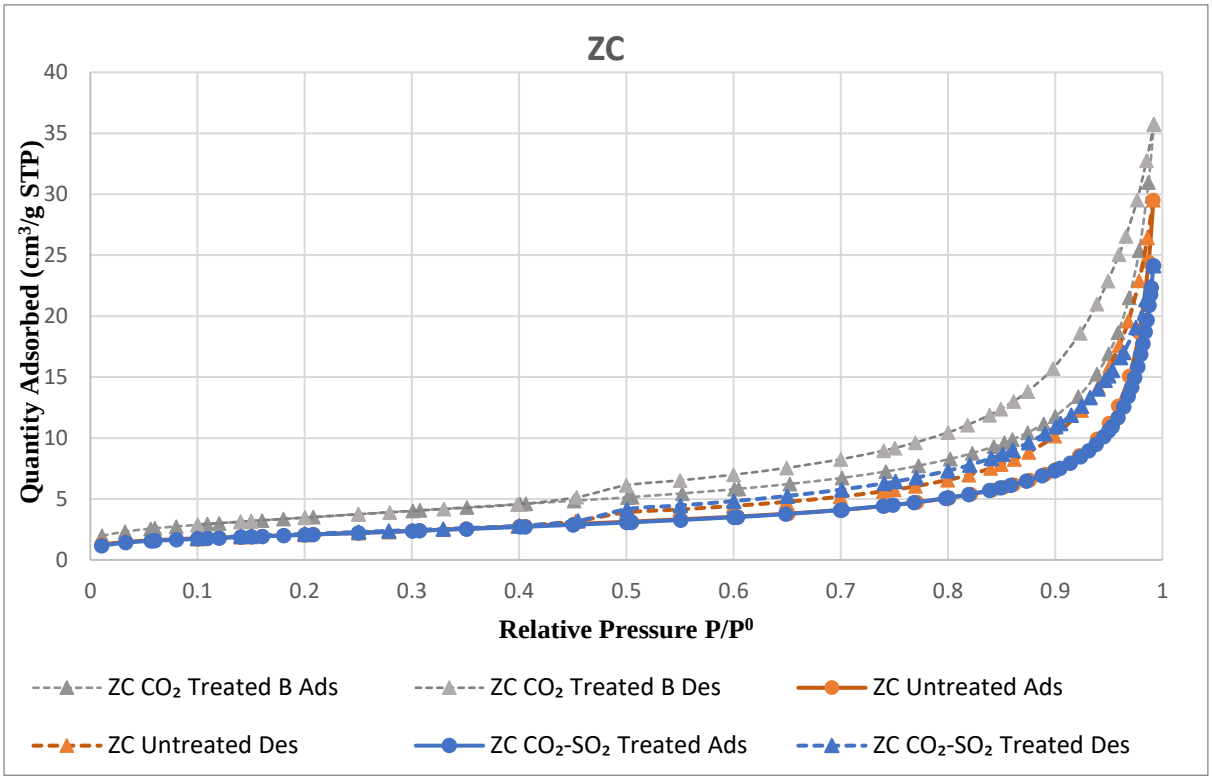

Figure 6.8: ZC untreated, CO_2 treated and CO_2 -SO_2 treated samples: N_2 BJH adsorption - desorption isotherms.

The mesopore PSD profiles of the CO_2-SO_2 treated sample similarly present a lower pore volume profile in comparison to the ZC CO_2 treated B sample (Figure 6.9). The ZC CO_2 -SO_2 treated sample PSD profile closely follows the untreated sample profile presenting only minor variations within the 0-100 Å range, where a peak shift is observed. A slightly lower pore volume profile is also observed from 200-2100 Å (Figure 6.10). These observations confirm the changes to the meso and macropore structure after CO_2 -SO_2 treatment with minor unique changes observed after the introduction of SO_2 into the CO_2 stream. The overall effect demonstrates lower mesopore and macropore volume. The N_2 BET surface area shows a 6% decrease after $_{sc}CO_2$ -SO_2 -water treatment whereas the Langmuir surface area remains the same. This reduction in the meso and macropore adsorption capacity, volume and surface area are likely due to pore clogging as a result of gypsum and smectite precipitation (Farquhar *et al.*, 2015; Pearce *et al.*, 2015).

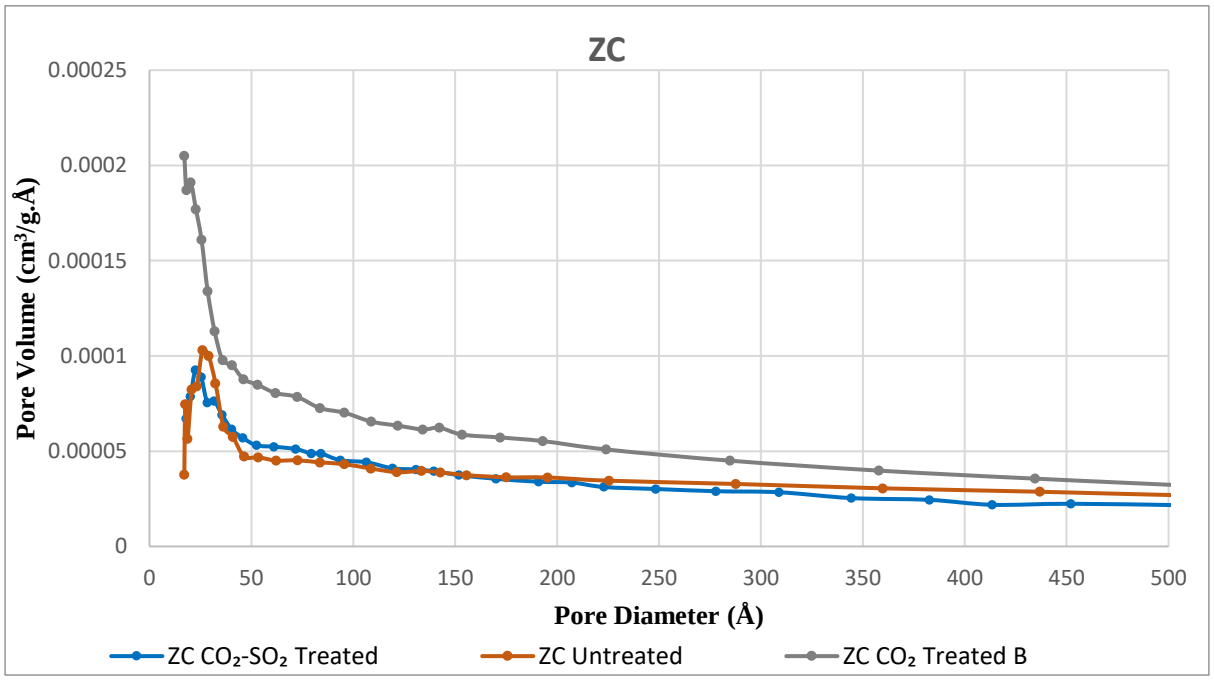

Figure 6.9: ZC untreated, CO_2 treated and CO_2 -SO_2 treated samples: BJH mesopore PSD profiles.

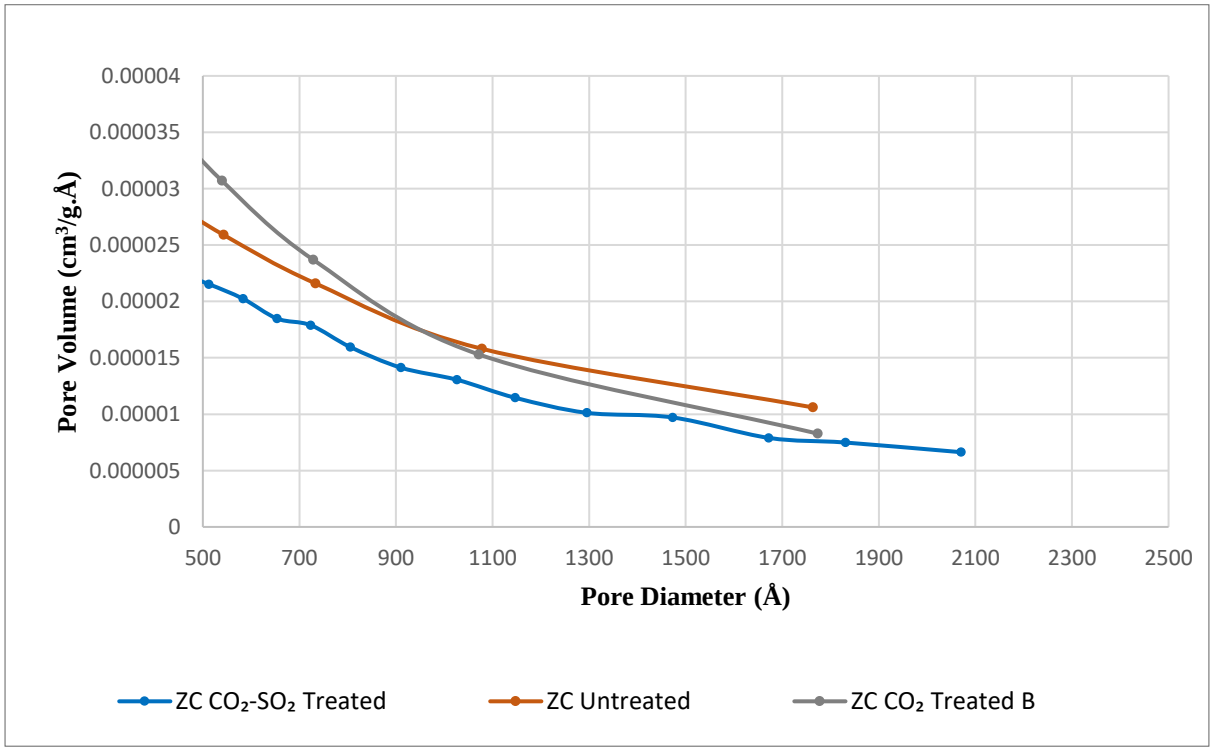

Figure 6.10: ZC untreated, CO_2 treated and CO_2 -SO_2 treated samples: BJH macropore PSD profiles.

Table 6.4: ZC N_2 Adsorption Surface Area Parameters

Sample	**N_2 BET m^2/g**	**N_2 Langmuir m^2/g**
ZC Untreated	3,17	10,91
ZC CO_2 treated A	4,00	15,23
ZC CO_2 treated B	4,87	18,76
ZC CO_2 -SO_2 treated	2.97	10.93

6.3.3 **ZG Low Pressure CO_2 Adsorption**

The ZG CO_2 -SO_2 treated sample micropore adsorption isotherm in Figure 6.11 shows a lower magnitude of increase in adsorption capacity as compared to that reported after CO_2 -water treatment. The ZG CO_2 -SO_2 treated sample micropore PSD profile in Figure 6.12 also demonstrates a close correlation with the untreated sample as observed by the peak shift from the ~4.24 Å pore width in the untreated sample to ~4.18 Å pore width in the ZC CO_2 -SO_2 treated sample. This particular peak appears to shift slightly to ~4.21 Å pore width in the ZC CO_2 treated B sample. It is likely that the lower increase in micropore adsorption capacity and volume is attributed to the reduced dissolution of orthoclase as indicated by the mineral alterations outlined in Table 6.1.

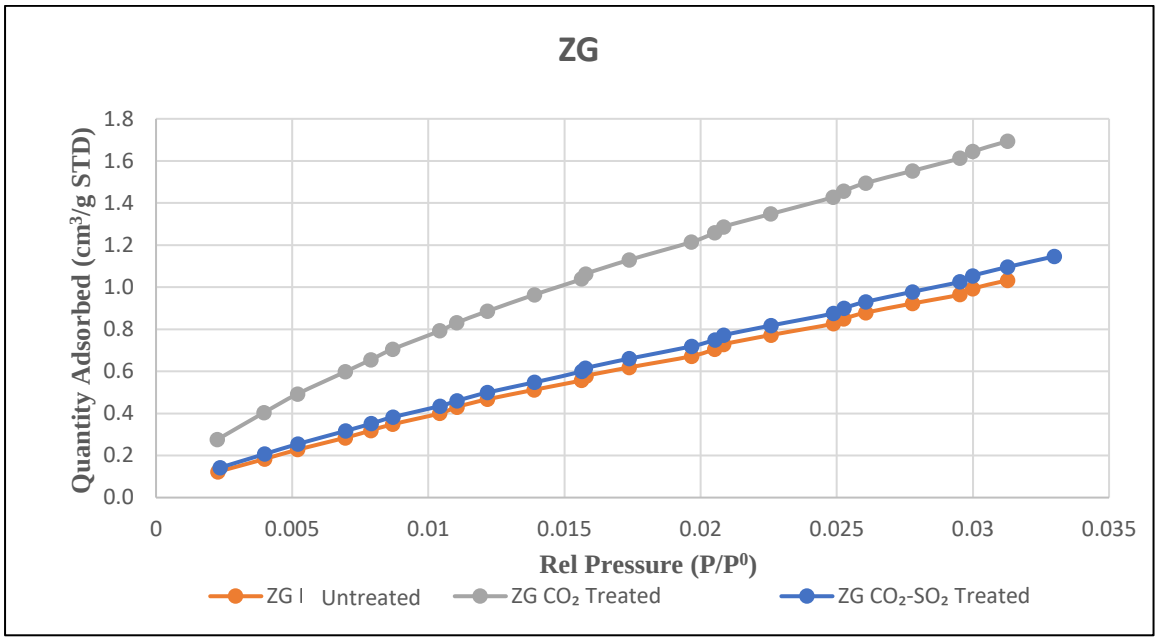

Figure 6.11: ZG untreated, CO_2 treated and CO_2 -SO_2 treated samples: CO_2 adsorption isotherms.

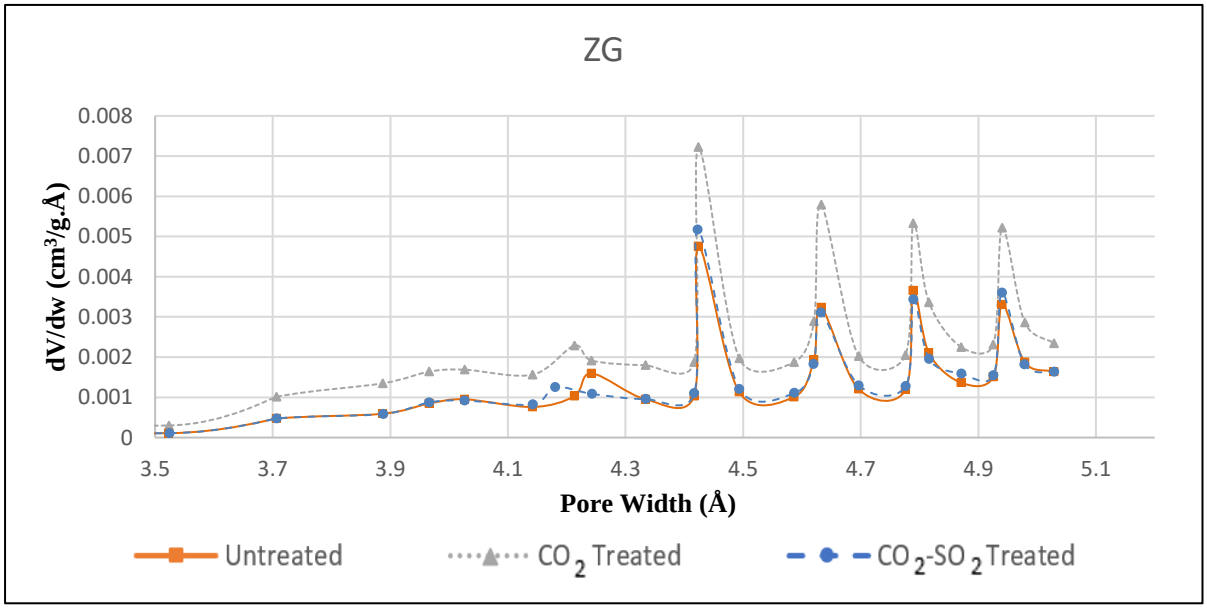

Figure 6.12: ZG untreated, CO_2 treated and CO_2 -SO_2 treated sample: H-K micropore PSD Profiles.

6.3.4 ZG Low Pressure N_2 Adsorption

The N_2 adsorption-desorption isotherms demonstrate a slight improvement in adsorption capacity throughout the relative pressure range as shown in Figure 6.13. An increase in the size

of the hysteresis loop is observed after treatment. The adsorption capacity at P/P^0=0.03 remains constant after treatment for the CO_2 -SO_2 treated sample. The ZG CO_2 -SO_2 treated mesopore PSD profile closely follows that of the untreated sample (Figure 6.14), with minor peak magnitude variations observed below the pore diameter of 26 Å. A slight variation and improvement in the PSD profile is observed in the ZG CO_2 -SO_2 treated sample up to ~350 Å pore diameter. This effect varies from the ZG CO_2 treated sample results which shows a significant improvement in pore volume throughout the profile. The ZG macropore profiles in Figure 6.15 demonstrates negligible improvements in macropore volume after CO_2 -SO_2 -water treatment. Subtle peaks are also observed at ~723 Å and ~1295 Å in the ZG CO_2 -SO_2 treated sample, these peaks are not observed in the ZC CO_2 treated and ZC Untreated PSD profiles. The reported observations indicate a change in the macropore structure of the sample that are unique to the introduction of SO_2 into the CO_2 stream during treatment.

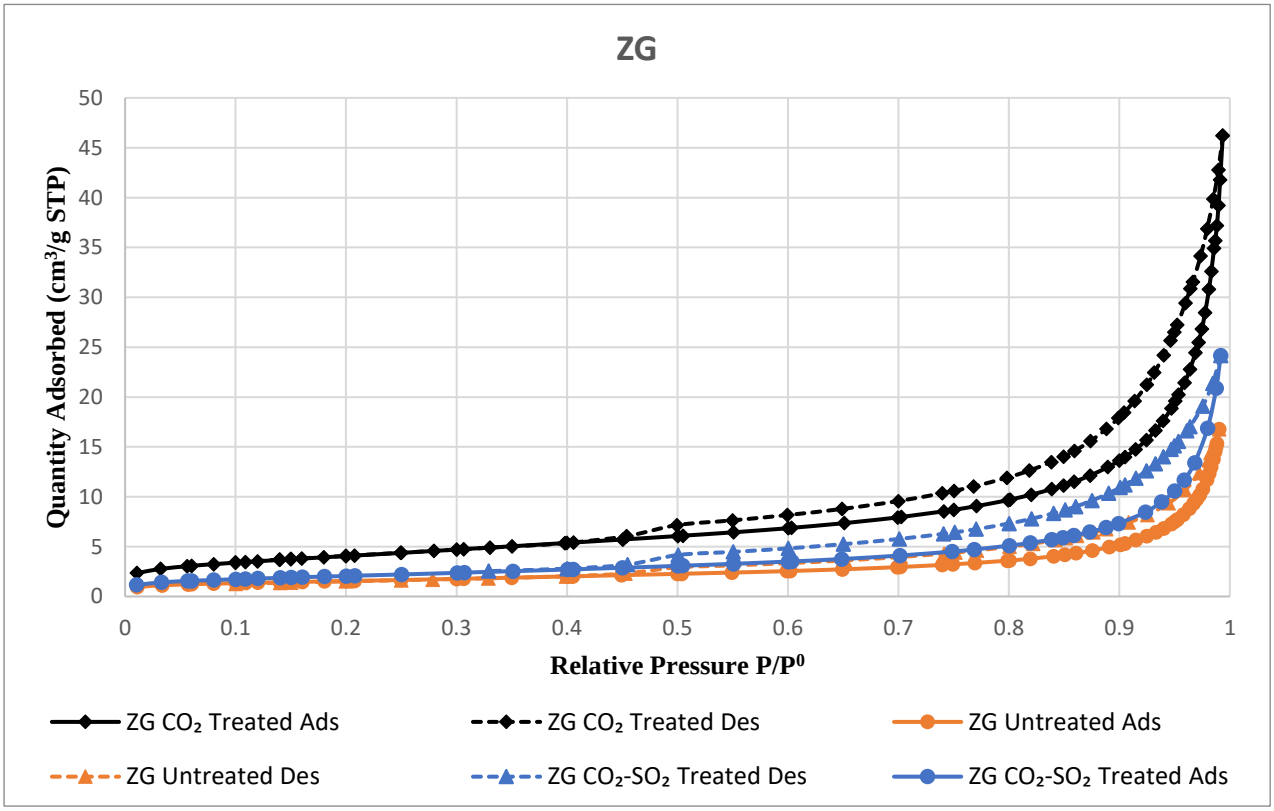

Figure 6.13: ZG untreated, CO_2 treated and CO_2 -SO_2 treated samples: N_2 BJH adsorption - desorption isotherms.

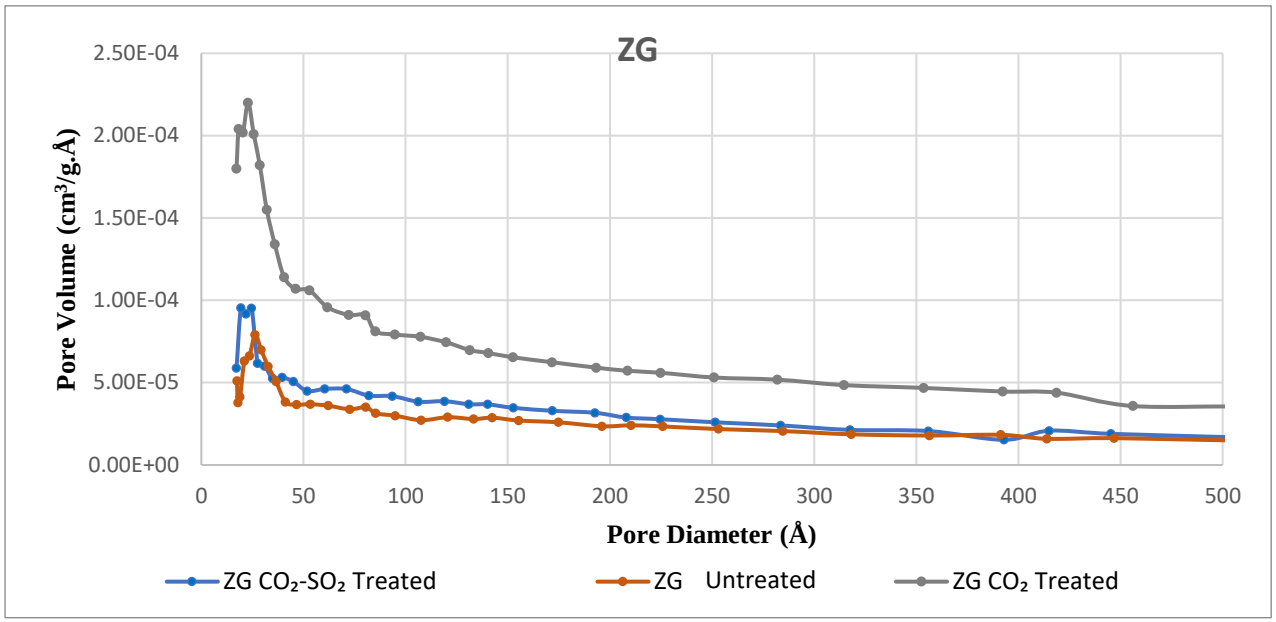

Figure 6.14: ZG untreated, CO_2 treated and CO_2 -SO_2 treated samples: BJH mesopore PSD profiles.

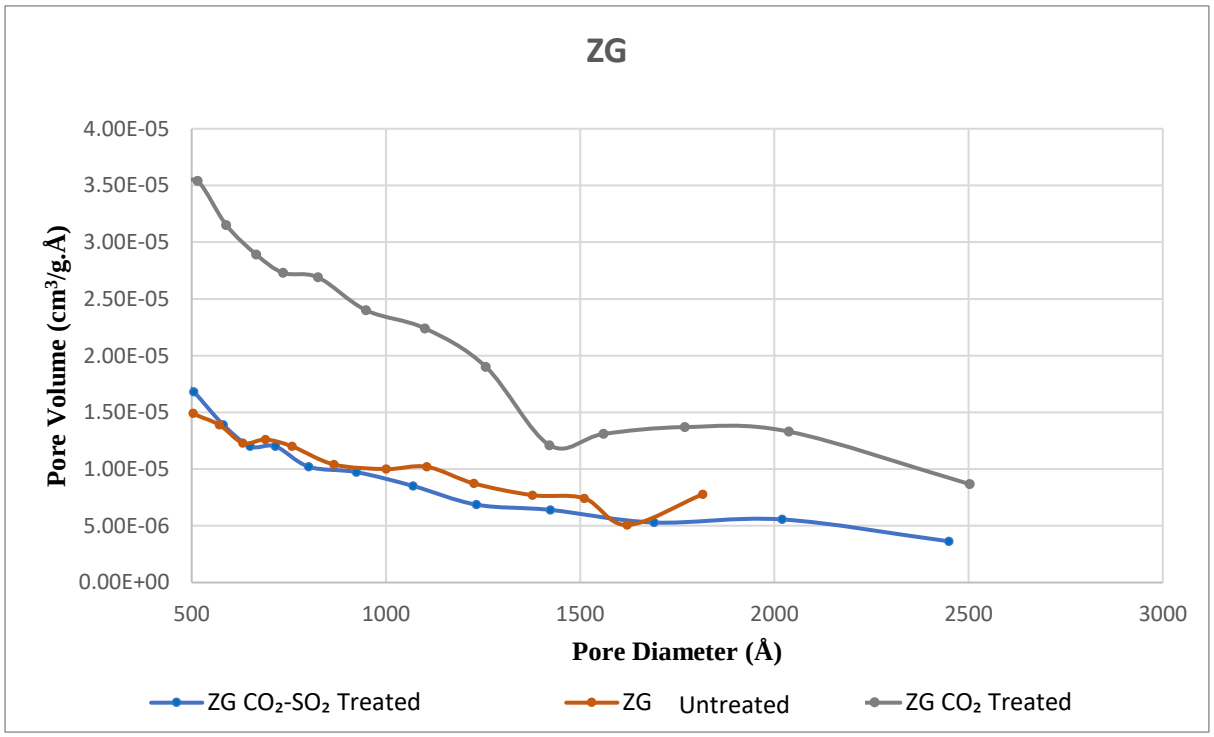

Figure 6.15: ZG untreated, CO_2 treated and CO_2 -SO_2 treated samples: BJH macropore PSD profiles.

Similar surface area values are determined for the ZG CO_2 -SO_2 treated sample as compared to the ZG untreated sample (Table 6.5). A slight increase at 2% is observed in the D-R surface area is reported in Table 6.6. Surface area improvements of 21% and 24% in BET and Langmuir models are reported at mesopore and macropore scale. These changes confirm a reduction in surface area in the ZG CO_2-SO_2 treated sample as compared to the ZG CO_2 treated sample. The resulting decrease in the adsorption capacity, pore volume and surface area are attributed to the notable precipitation of plagioclase and calcite in the CO_2 -SO_2 treated sample (Table 6.1). All the identified pore structure variations could be linked to mineral alterations during treatment. The influence of mineral alterations is therefore shown to affect the resulting pore structures (Wu *et al.*, 2019).

Table 6.5: ZG CO_2 Adsorption Pore Parameters

Sample	**CO_2 Dubinin-Radushkecich Micropore SA (m^2/g)**	**CO_2 Dubinin-Astakhov Limiting Micropore Volume (cm^3/g)**	**Ave Pore size (Å)**
ZG Untreated	12,70	0,032	6,36
ZG CO_2 treated	19,80	0,034	9,62
ZG CO_2 -SO_2 treated	12,97	0.035	7,06

Table 6.6: ZG N_2 Adsorption Surface Area Parameters

Sample	**N_2 BET m^2/g**	**N_2 Langmuir m^2/g**
ZG Untreated	2,10	7,76
ZG CO_2 treated	5,42	21,70
ZG CO_2 -SO_2 treated	2,55	9,69

6.4 Key Findings

6.4.1 Mineral Alterations

The mineral alterations in the ZC and ZG sample after treatment to a 99% CO_2 and 1% SO_2 gas-water mixture were assessed. The ZC sample predominantly displays plagioclase and calcite dissolution associated with quartz, smectite and gypsum precipitation. The introduction of SO_2 introduces calcite conversion into gypsum, which is expected to present porosity decreases in the sample, in agreement with Farquhar *et al.* (2015) and Pearce *et al.* (2015).

The ZG sample indicates the precipitation of plagioclase, quartz, calcite, and smectite. Stilbite and orthoclase are observed to decrease at a higher rate after CO_2 -SO_2 treatment. The different mineral alterations in the two samples are attributed to the varying mineral compositions, further justifying the need for and importance of reservoir specific experimental analyses for the determination of CO_2 sequestration implications.

6.4.1 Effects on the Surface Chemistry

The FTIR spectra reports changes in the functional groups that are in line with the XRD results findings. The surface chemistry changes in the ZC sample indicate a reduction in the OH functional group bond vibrations and the elimination of calcite after CO_2 -SO_2 treatment. A reduction in the peak intensities is observed after CO_2 -SO_2 treatment along with the formation of Si (Al)-O functional groups from precipitated plagioclase. The reduction in peak intensities is similarly reported after CO_2 treatment and has also been reported in literature (Yin *et al.*,

2016; Goodman *et al.,* 2019). This has been shown to indicate an increase in sample micro heterogeneity in the CO_2 treated samples as compared to the untreated samples (Mayerhöfer, 2004).

The ZG sample presents a higher intensity FTIR spectrum after CO_2 -SO_2 treatment compared to the untreated and CO_2 treated samples. Calcite functional groups are also detected along with O-Si (Al)-O, indicating the higher compositions of the orthoclase and precipitated plagioclase after CO_2 -SO_2 treatment. It is interesting to note the different reactions that take place in the two rock samples after treatment. The formation of gypsum in the ZC lateral seal core sample is facilitated by the presence of calcite in the untreated sample and may serve to enhance its sealing properties.

6.4.2 **Effects on Textural Properties**

An increase in micropore adsorption capacity, surface area and volume were observed in the ZC sample after CO_2 -SO_2 treatment. Variations in the PSD profile peaks were also observed indicating a change in the pore size distribution profiles. The peak changes observed were found to be similar to those observed after CO_2 treatment, indicating similar changes in certain elements of the pore structure despite the introduction of SO_2 into the CO_2 stream. These changes in the ZC sample micropore structure are attributed to the calcite dissolution observed in the XRD and FTIR results and are in line with findings reported in similar studies (Yin *et al.*, 2016; Luo *et al.*, 2018; Zhu *et al.*, 2018; Dai *et al.*, 2020). The meso and macropore structures presented minimal property changes. Minor changes in the hysteresis loop were observed in the CO_2 -SO_2 treated sample, implying possible pore morphology changes (Ã *et al.*, 2015; Yin *et al.*, 2016; Mavhengere *et al.*, 2021). Lower pore volumes and surface area were presented post CO_2 -SO_2 treatment that after CO_2 treatment due to gypsum precipitation in during CO_2 -SO_2 treatment (Farquhar *et al.*, 2015; Pearce *et al.*, 2015).

The ZG sample presented only minor improvements in the micropore adsorption capacity, volume, and surface area following treatment. This is likely due to the lower dissolution rates observed in the sample (Zhu *et al.*, 2018). A slight improvement in the meso and macropore adsorption capacity and pore volume is observed in comparison to the untreated sample. This however presented a reduction in the same parameters when compared to the ZG CO_2 treated

sample. These property changes could be attributed to the increased rate of plagioclase dissolution observed during CO_2 -SO_2 treatment. The mineral alterations in the sandstone sample were observed to lead to notable changes in the physical pore structures. These correlations and their effects on long term CO_2 storage are detailed further in Chapter 7.

7 CHAPTER 7: SUMMARY, CONCLUSIONS AND RECOMMENDATIONS

7.1 Summary

A novel approach in considering the effects of CO_2 and CO_2-SO_2 gas mixture influence on South Africa's Zululand Core samples under sequestration conditions has been considered. The study outlines mineral alterations, chemical structure influences, as well as the micropore, mesopore and macropore structure variations after experimental treatment. The experimental treatment of the samples was designed to facilitate CO_2 sequestration conditions for elongated time periods (of up to two months). The experimentation was conducted in stainless steel teflon lined reactors designed to ensure the following:

i. Maintenance of constant high pressures of up to 175 bars throughout the treatment duration.
ii. Maintenance of constant temperatures up to 73 ºC using temperature control units.
iii. Acid resistance reactor surface to prevent reactions with the reactor itself particularly upon the introduction of water and impurity gases such as SO_2.

This novel method of simulating CO_2 sequestration in core samples facilitates the evaluation of mineralogical, textural, and surface chemistry changes that could arise due to CO_2 sequestration in sedimentary basins. The current set up, which was designed and procured as part of this study allows for further world class experimental assessments of geological formations with respect to CO_2 sequestration in South Africa. The reservoir rock properties and composition are known to influence CO_2 storage capability. Reservoir CO_2 trapping capacity is known to primarily depend on the mineral rock composition (Xu *et al.*, 2005). Xu *et al.* (2017) after conducting CO_2 injection simulations showed that mineral dissolution affects capillary pressure and relative permeability in the rock. Mineral alterations were indicated to affect the pore structure and wettability in porous media, in turn changing the multiphase flow in the sample (Xu *et al.*, 2017). The mineral composition of the rock sample therefore plays a key role in evaluating the CO_2 trapping capacity in the reservoir. Changes evaluated after CO_2 exposure provide insight into the typical trapping mechanisms that could be at play during sequestration in the current study. Different mineral alterations were

observed in the studied samples; these were dependent on the untreated sample compositions. The mineral alterations reported varied upon changing the duration of treatment and the composition of the treatment gas as observed in the ZC and ZG samples. The FTIR analyses demonstrated a reduction in peak intensity after CO_2 treatment for all samples. This has been shown to indicate micro heterogeneity in the CO_2 treated samples as compared to the untreated samples (Mayerhöfer, 2004). And indicates mineral migration throughout the sample during treatment, leading to a less homogenous sample mixture. The presence of water, varying trace levels of organic matter, silica and calcite was confirmed in the samples. The reduction in peaks was also observed after CO_2-SO_2 treatment in the ZG sample, this was not shown after treatment of the ZC sample, implying the treated sample presented higher micro-homogeneity.

Changes in micropore, mesopore and macropore textural properties were observed in the studied samples. The pore structure was analysed through the application of low-pressure CO_2 and N_2 adsorption on untreated and CO_2 treated samples. All samples presented Type IV isotherms in line with isotherms for typical mesoporous solids (Clarkson *et al.*, 2012). Different observations were reported for the five samples studied. Xiao *et al.* (2017) classified pores under (0.5 μm) 5000 Å as nanopores in tight sandstones. These were described as consisting of clay associated pores and intraparticle dissolution pores which contribute both to reservoir storage and percolation, especially to the sample surface area. Qiao *et al.* (2020) studied deeply buried sandstones and reported that up to 70% of the pore size distribution of the sandstones was made up of pores under 1 μm. The present study covers a sizeable portion of the pores that contribute to storage capacity and percolation characteristics in sandstone reservoirs. The findings pertinent to each of the samples studied are outlined in the sections below. The investigated characteristics and properties are discussed and related to reservoir CO_2 storage mechanisms and effects.

7.2 CO_2 Treatment

The findings reported for each of the samples after CO_2 treatment are discussed in this chapter. Conclusions are also discussed on the indicated effects on sample, the potential impacts on the reservoir rock properties and storage capacity.

7.2.1 **ZA**

The ZA sample is composed of silicate and clay minerals (52%). These minerals have been shown to present mineral sequestration capacity (Xu *et al.*, 2004). Although sequestration conditions determine actual sequestration capacity, it can be concluded that the sample presents potential sequestration capacity when exposed to CO_2 and water over time. Post CO_2 treatment, the ZA sample displayed that CO_2 trapping mechanisms took place leading to the alteration (reduction) of the plagioclase silicate, calcite and smectite, confirming the findings reported in literature. It is therefore implied that the ZA sample presents storage capacity in the reservoir through reactive trapping mechanisms. It is noted that the sample presents the highest quartz precipitation rate, which could in turn negatively affect the pore structure and limit further CO_2 mineral alterations. Surface chemistry evaluations through FTIR analyses confirmed the dissolution of calcite in the sample and general mineral migration during treatment. No other notable variations in the surface chemistry of the sample were observed.

The mineral alterations reported during the CO_2 trapping process were shown to influence the pore and chemical surface structures of the sample. The ZA sample demonstrated a reduction in CO_2 adsorption capacity, micropore, mesopore and macropore volume and surface area following treatment. This is likely attributed to the quartz precipitation observed in the sample during treatment. Since mineral migration has been confirmed in the sample, it is likely that quartz precipitation led to the clogging of pores during treatment (Xu *et al.*, 2017). The reduction of sample porosity implies a resulting reduction in storage capacity.

7.2.2 **ZC**

The ZC sample represented the Zululand core sample's lateral seal. It was therefore anticipated that the reactions observed in this sample would improve the sealing abilities of the reservoir. The sample also presented a high concentration of silicate and clay minerals (56%), all of which may be prone to CO_2 trapping mechanisms (Xu *et al.*, 2004). Alterations to these mineral groups were observed during CO_2 treatment. The changes in the plagioclase content were observed to be minimal when compared to those observed in the ZA sample. The ZA sample contained a similar composition of plagioclase and demonstrated a 25% dissolution rate compared to the 10% observed in the ZC treated B sample (which was similarly treated for 2

months) after similar treatment. This could be caused by varying accessibility of the reactive mineral components in the two samples. The difference in dissolution rates could also be caused by the different forms of plagioclase available in the mineral as the dissolution behaviour of plagioclase is known to dependent on their structure/composition (Gudbrandsson *et al.*, 2014). Gudbrandsson *et al.* (2014) describes microscale exsolution of plagioclases as a common process that leads to fine albite rich and anorthite rich intergrowths, which in turn influence the dissolution kinetics of the plagioclases. Oxburgh *et al.* (1994) further explains that this could lead to varying dissolution rates in samples with similar bulk compositions. A lower dissolution rate as a result of albite rich plagioclase mineral content would be beneficial to the ZC rock as it indicates lower trapping capacity potential and higher sealing capability. Only 49% of the calcite observed in the ZC sample was observed to dissolve during CO_2 treatment, and smectite was observed to precipitate. It is interesting to see that the ZC treated A sample presented a higher intensity profile than the ZC treated B sample. This implies that the sample treated for 2 months presented a more heterogenous microstructure that the one treated for one month.

The average pore size, and micropore surface area was shown to increase after CO_2 treatment. This is likely as a result of the dissolution of calcite and plagioclase in the sample (Luo *et al.*, 2018; Wu *et al.*, 2019). The dissolution pores arising from the mineral alterations could pose a threat in the capability of the lateral seal to contain CO_2 within the reservoir. Further investigations into the implications of these mineral alterations on the mechanical integrity of the rock are therefore prompted.

7.2.3 **ZE**

The ZE sample has the lowest composition of potentially reactive minerals compared to the other samples (32,5%). As expected, limited mineral alterations were observed in this sample. Only slight smectite dissolution as reported after CO_2 treatment, along with little precipitation of plagioclase, was observed. No notable changes on the surface functional groups were observed, except for the reduction in peak intensity after treatment. The ZE sample reported minor increases in micropore, mesopore and macropore adsorption capacity, surface area and volume. It is therefore inferred that the ZE core sample indicates lower CO_2 adsorption capacity within the reservoir. The ZE sample therefore presents a much slower rate of mineral trapping

of CO_2 during injection. The high percentage of quartz contained in the sample implies lower probability of mechanical failures due to rapid calcite and clay dissolution during injection (Hangx *et al.*, 2013).

7.2.4 **ZF**

The ZF sample presents a relatively high composition of high potential CO_2 sequestration minerals at 66%. Complete dissolution of calcite and slight dissolution of smectite is reported for this sample; close to 17% of the total sample weight is observed to dissolve. The presence of carbonates in the sample is known to enhance solubility trapping of CO_2 (Xu *et al.*, 2004). In this particular sample, the calcite at 10% of the total composition is observed to completely dissolve and lead to the precipitation of plagioclase which is likely to facilitate mineral CO_2 sequestration over time (Bachu *et al.*, 1994; Xu *et al.*, 2004; Mavhengere *et al.*, 2021). Organic matter dissolution is implied in the ZF CO_2 treated sample spectra. This is expected to add to the formation of micropores in the sample. Limited overall increases in micropore, mesopore and macropore volume were observed for the ZE sample after treatment. The ZF sample therefore presents high capacity for CO_2 sequestration via mineral trapping.

7.2.5 **ZG**

The ZG sample presented the highest concentration of minerals presenting CO_2 sequestration capacity (78%). Due to the lack of carbonates in the sample, notable dissolution of clays and silicates (14%) was observed. This was accompanied by the formation of plagioclase, calcite, and stilbite. The different alterations observed in the samples outline the complexity of the $_{sc}CO_2$ -water treatment influences on specific rock samples. Plagioclase and clay dissolution and precipitation in particular plays a significant role in geological sequestration (Zhang *et al.*, 2009). It can be concluded that the ZG sample from the Zululand Cenomanian Basin presents the highest CO_2 mineral trapping capacity. The surface chemistry investigation confirmed calcite precipitation and mineral migration in the sample during CO_2 treatment. The LPGA demonstrated the highest increase in the micropore, mesopore and macropore volume, adsorption, and surface area. The high mineral trapping rate presented by the ZG sample prompts the need for further investigation to determine possibility of mechanical failures caused by clay dissolution in the rock (Hangx *et al.*, 2013). According to Xu *et al.* (2017),

calcite precipitation may facilitate reservoir self-sealing, in turn reducing the risk of CO_2 leakages into the surrounding rock and environment.

7.3 CO_2-SO_2 Treatment

The ZC and ZG samples were treated with a 99% CO_2 and 1% SO_2 gas mixture under the similar pressure and temperature conditions. Different effects of this treatment were determined on the two sandstone samples.

7.3.1 **ZC**

The introduction of SO_2 into the CO_2 stream resulted in the conversion of calcite to gypsum in the ZC sample. The ZC sample demonstrates further reductions in the peak intensities after treatment, indicating additional sample migration and microstructure heterogeneity after CO_2-SO_2 treatment (Mayerhöfer, 2004). Increased micropore, adsorption capacity, surface area and volume were also observed, whilst the mesopore and macropore changes remain minimal. Changes in the PSD profile peaks were also noted, similar to those observed after CO_2 treatment. It is clear that a higher level of mineral alterations was observed after CO_2-SO_2 treatment than after CO_2 treatment.

The higher dissolution rate in the sample is the likely reason for the increase in micropore volume and surface area. This dissolution was probable countered by the precipitation of gypsum leading to the clogging of the larger mesopores and macropores (Farquhar *et al.*, 2015; Pearce *et al.*, 2015; Yin *et al.*, 2016; Luo *et al.*, 2018; Zhu *et al.*, 2018; Dai *et al.*, 2020). Minor changes in the hysteresis loop were observed in the CO_2 -SO_2 treated sample, implying possible pore morphology changes (Ã *et al.*, 2015; Yin *et al.*, 2016; Mavhengere *et al.*, 2021).

7.3.2 **ZG**

Higher smectite, stilbite and orthoclase dissolution rates were reported after CO_2-SO_2 treatment of the ZG sample. The precipitation of quartz, plagioclase and calcite was also observed to increase in comparison to the CO_2 treated sample results. Interestingly, a higher intensity FTIR spectra profile was presented for the ZG sample after CO_2-SO_2 treatment. This implies that the resulting sample was more homogenous than the untreated and CO_2 treated samples. Calcite functional groups are also detected along with O-Si (Al)-O indicating possible higher

compositions of the precipitated plagioclase after CO_2 -SO_2 treatment as indicated by the XRD results. The ZG sample shows minimal improvements in the micropore, mesopore and macropore adsorption capacity, volume, and surface areas. Following the FTIR results, the ZG sample portrays less mineral migration during CO_2-SO_2 treatment, as compared to CO_2 treatment. It is also however noted that, although a higher smectite dissolution rate is reported, a lower orthoclase dissolution rate is reported in the sample, in line with higher plagioclase and quartz precipitation; these two processes counteracting each other could also lead to less pore structure changes (Zhu *et al.*, 2018). Stilbite dissolution was also reported in this sample after CO_2-SO_2 treatment despite precipitation of the same mineral being observed post CO_2 treatment. The reason for improved sample heterogeneity in the ZG is likely linked to the reduction in the mineral groups in the CO_2-SO_2 treated sample.

7.4 Conclusions on the Effects of CO_2 treatment on Zululand Samples

The trapping mechanisms at the pore structure scale are reported to account for up to 97% of the residually trapped CO_2 during storage (Cui *et al.*, 2017; Mavhengere *et al.*, 2021). It must be noted that the mineral alterations in the samples ultimately led to mineral migration and pore structure alterations, hence it may be concluded that the storage capacity of the reservoir is highly dependent on the mineral alterations taking place over time. These mineral alterations are expedited in experimental conditions due to manipulated particle sizes and rock: water ratios. This information serves as a crucial foundation for the extrapolation of the effects of CO_2 injection in the respective reservoirs. The following conclusions could be made from the observed findings:

1. Mineral alterations were observed in all sample studied. These were influenced by the inherent sample mineral compositions. The higher the composition of high potential CO_2 sequestration minerals, the higher the potential CO_2 trapping capacity in the sample. The sample that presented the highest quartz content was observed to display minimal mineral alterations during treatment (ZE). The ZG sample presented the highest mineral trapping rates and pore structure alterations; implying high suitability for CO_2 sequestration in the Cenomanian middle sandstone Basin and relatively higher storage capacity as compared to the rest of the core samples

2. Surface chemistry changes were influenced by mineral migration through the samples. This led to changes in the microstructure homogeneity.
3. Pore structure changes were observed to be influenced by mineral alterations in the samples and were observed to lead to pore structure changes. The ZA sample that displayed the highest precipitation rates of quartz presented overall reductions in gas adsorption capacities, pore volumes and surface areas. The samples that demonstrated higher levels of mineral dissolution showed overall improvement in adsorption capacities, pore surface area and volume.
4. The ZA and ZE core samples demonstrated the least suitability for CO_2 injection tests due to the indicated lower storage capacities. The reactivity of the ZC sample implies a potential compromise in the lateral seal of the Zululand Basin during injection with pure CO_2. Further studies are required to verify the effectiveness of the lateral seal through numerical modelling.

7.5 Conclusions on the Effects of CO_2-SO_2 Treatment on the ZC and ZG Zululand Core samples.

The following conclusions were made from the treatment of the ZC and ZG samples with 99% CO_2-1% SO_2 gas mixture under typical CO_2 sequestration conditions:

1. Differences in the extent of mineral alterations were observed after CO_2-SO_2 treatment compared to post CO_2 treatment of the same samples. Depending on the untreated sample composition, a new reaction (gypsum formation) was introduced as a result of the introduction of SO_2 in the CO_2 stream.
2. Increased microstructure heterogeneity was implied by the FTIR analyses, indicating higher mineral migration in the ZC sample. The microstructure heterogeneity in the ZG sample was observed to decrease, implying reduced mineral migration.
3. Increments in the micropore structure surface area and adsorption capacity were reported in line with the increased dissolution rates in the ZC sample. Minimal changes in the mesopore and macropore structure were observed and attributed to the precipitation of gypsum. Minimal changes in the ZG pore structure were attributed to the increased smectite dissolution countered by quartz and plagioclase precipitation.

The mineral alterations were also shown to significantly influence the pore structure changes.

The introduction of SO_2 into the CO_2 stream led to differences in the mineral alterations, surface chemistry changes and physical characteristics taking place during CO_2 treatment. A significant reduction in the ZG sample mineral alterations and pore structure changes was reported after CO_2-SO_2 treatment in comparison to the changes observed after CO_2 treatment. It may be implied that the presence of SO_2 limited the CO_2-rock-water interactions during treatment. Contrary results were observed in the ZC sample. The presence of SO_2 in the CO_2 stream was observed to potentially enhance the self-sealing capacity of the ZC lateral seal core sample through the facilitation of gypsum precipitation. The reactions taking place in the two samples are a function of the inherent sample mineral compositions. Whilst the ZC sample contained calcite and negligible smectite clay, the ZG sample presented relatively high smectite composition and no mineral carbonates

7.6 Overall Findings

This study aimed to investigate the long-term effects of CO_2 and CO_2-SO_2 gas mixtures on the structure and properties of the sandstone samples at supercritical pressures, providing more insight into the crucial rock-gas interactions relative to CO_2 storage. This aim was fulfilled by addressing the following research questions out lined in Section 1.5.

7.6.1 Q1. Are the physical and chemical properties of the Zululand Basin sandstone core samples affected by the exposure to typical sequestration conditions using CO_2 and CO_2-SO_2 gas mixtures?

The physical and chemical properties of the five Zululand Basin sandstones were variably affected by exposure to typical CO_2 sequestration conditions. The physical and chemical alterations are summarised on Section 7.2 of this study. The two Zululand Basin core samples that were further exposed to CO_2-SO_2 gas mixture demonstrated notable changes in mineral composition and minimal changes in the physical microstructure characteristics. These physical and chemical property changes are summarised in Section 7.3 of this study.

7.6.2 Q2. What are the physical and chemical interactions taking place between the pure and mixed gas streams and the geological materials under CO_2 sequestration conditions?

Chapter 5 and 6 outlines the physical and chemical interactions observed after CO_2 and CO_2-SO_2 treatment. The chemical interactions observed were various mineral dissolution and precipitation reactions observed in all five samples. Reactions with the gas phases were reported in the indirect reaction of calcium silicates with CO_2 to produce calcite in the ZG sample. The indirect reaction of SO_2 with calcite to for gypsum was also reported on in the ZC sample after CO_2-SO_2 treatment. These chemical changes were observed to influence physical changes in the rocks' pore structures, leading to pore clogging as a result of mineral precipitation and the formation of dissolution pores.

7.6.3 Q3. What are the differences in the physical and chemical interactions taking place in each of the samples as a function of their sample composition and gas mixtures used for treatment?

The various physical and chemical interactions reported were shown to be dependent on the sample's inherent mineral composition. The chemical changes were observed to drive the physical changes in the sample. Samples such as the ZE sample presented minimal chemical reactions as a function of the high quartz content observed in the sample, in turn limiting the physical changes observed. The ZF sample on the other hand, containing 78% of the reactive mineral groups, presented the most significant changes in the mineral composition and pore structure. Increases in sample porosity were indicated through increases in micro pore, mesopore and macropore adsorption capacity, surface area and pore volume. A detailed summary of these differences is outlined in this study.

7.6.4 Q4. What implications do these interactions infer on the long-term storage of such gas streams in the target storage locations?

The interactions observed indicate the suitability of some of the cores for CO_2 sequestration mainly through mineral trapping. The ZA and ZF samples present potential for CO_2 sequestration through mineral trapping. Although lower rates of mineral alterations were reported, the samples presented relatively high quartz content, indicating lover probability of

mechanical failures during injection. This is more for the ZA sample which demonstrates pore clogging through the reduction in pore surface area, and volume, indicating potential reduction in permeability over time. Although this may improve the mechanical integrity of the ZA rock, it could also limit CO_2 mobility during injection.

The ZE sample showed minimal mineral interactions leading to minor pore structure changes. This implies lower capacity for CO_2 sequestration through mineral trapping in this particular sample.

The ZC lateral seal sample demonstrates mineral trapping reactions that lead to increased pore volume. A lower plagioclase dissolution rate was however reported on the ZC sample. The dissolution pores observed after CO_2 treatment pose a threat of increasing the porosity and permeability of the lateral seal. The formation of gypsum during CO_2-SO_2 treatment facilitates minimal mesopore and macropore volume and surface area in the sample, indicating possible improvement in permeability and therefore seal integrity.

The ZG sample was observed to present the highest capacity for CO_2 sequestration through mineral trapping. Due to the notable increases in pore volume and surface area, there is need for further studies to evaluate the risk of rock fracture in this core sample. The results present novel and valuable information on the evolution of mineral and microstructure changes in the South African Zululand core samples after treatment with CO_2 and CO_2-SO_2 gas mixtures under wet conditions. Such a study has not been conducted on Zululand Basin core samples. The current study forms a foundation for understanding the Zululand Basin's rock composition and interaction with CO_2 gas streams. It also further facilitates the prediction of long-term implications of CO_2 sequestration.

7.7 Recommendations

The following recommendations are made to further extend this study in preparation for the SACCCS Pilot Scale Injection Project.

- Further manipulation of the presented data through numerical modelling to determine the effects of long-term CO_2 injection in the Zululand Basin is recommended as the

next crucial step to understand the resulting long-term impacts at reservoir scale. Researchers such as Xu *et al.* (2004) have done significant work in this area using data obtained from similar experimental studies and represent appropriate references for consultation in this regard.

- Additional experimental work is recommended to investigate the effects of CO_2 and SO_2 on the other core samples and for longer time frames.
- Different techniques that were not available to this study such as Nuclear Magnetic Resonance (NMR) and Computerised Tomography (CT) scan analyses could be considered for future study to evaluate a wider sandstone pore size range.
- Mineral dissolution induced mechanical weakening should be investigated in line with the mineral alterations determined in this study. This is essential in order to prevent reservoir failure during injection (Hangx *et al.*, 2013).

8 REFERENCES

Ã, J.G., Chalmers, H., 2015. 2008-GibbinsChalmers-Carbon capture and storage.pdf 36, 4317–4322. https://doi.org/10.1016/j.enpol.2008.09.058

Ahmadinia, M., Shariatipour, S.M., Andersen, O., Nobakht, B., 2020. Quantitative evaluation of the joint effect of uncertain parameters in CO_2 storage in the Sleipner project, using data-driven models. International Journal of Greenhouse Gas Control 103, 103180. https://doi.org/10.1016/j.ijggc.2020.103180

Alimi, F., Elfil, H., Gadrib, A., 2003. Kinetics of the precipitation of calcium sulphate dihydrate in a desalination unit. Desalination 157,9 -16.

Allen, D.T., Palen, E.J., Haimov, M.I., Hering, S.V., Young, J.R., 1994. Fourier Transform Infrared Spectroscopy of Aerosol Collected in a Low-Pressure Impactor (LPI/FTIR): Method Development and Field Calibration. Aerosol Science and Technology 21, 325–342. https://doi.org/10.1080/02786829408959719

Al-Yaseri, A.Z., Roshan, H., Lebedev, M., Barifcani, A., Iglauer, S., 2016. Dependence of quartz wettability on fluid density: Fluid Density-Quartz Wettability. Geophys. Res. Lett. 43, 3771–3776. https://doi.org/10.1002/2016GL068278

Anovitz, L.M., Cole, D.R., 2015. Characterization and Analysis of Porosity and Pore Structures. Reviews in Mineralogy and Geochemistry 80, 61–164. https://doi.org/10.2138/rmg.2015.80.04

Arts, R., Eiken, O., Chadwick, A., Zweigel, P., van der Meer, L., Zinszner, B., 2004. Monitoring of CO_2 injected at Sleipner using time-lapse seismic data. Energy 29, 1383–1392. https://doi.org/10.1016/j.energy.2004.03.072

Aydin, G., Karakurt, I., Aydiner, K., 2010. Evaluation of geologic storage options of CO_2: Applicability, cost, storage capacity and safety. Energy Policy 38, 5072–5080. https://doi.org/10.1016/j.enpol.2010.04.035

Bachu, S., 2000. Sequestration of CO_2 in geological media: criteria and approach for site selection in response to climate change. Energy Conversion and Management 41, 953–970. https://doi.org/10.1016/S0196-8904(99)00149-1

Bachu, S., 2002. From Regional Characterization to Site Selection. Energy Conversion and Management 41, 87–102. https://doi.org/10.1016/S0196-8904(01)00009-7

Bachu, S., 2007. Carbon dioxide storage capacity in uneconomic coal beds in Alberta, Canada: Methodology, potential and site identification. International Journal of Greenhouse Gas Control 1, 374–385. https://doi.org/10.1016/S1750-5836(07)00070-9

Bachu, S., 2008. CO_2 storage in geological media: Role, means, status and barriers to deployment. Progress in Energy and Combustion Science 34, 254–273. https://doi.org/10.1016/j.pecs.2007.10.001

Bachu, S., Bonijoly, D., Bradshaw, J., Burruss, R., Holloway, S., Christensen, N.P., Mathiassen, O.M., 2007. CO_2 storage capacity estimation: Methodology and gaps. International Journal of Greenhouse Gas Control 1, 430–443. https://doi.org/10.1016/S1750-5836(07)00086-2

Bachu, S., Gunter, W.D., Perkins, E.H., 1994. Aquifer disposal of CO_2: Hydrodynamic and mineral trapping. Energy Conversion and Management 35, 269–279. https://doi.org/10.1016/0196-8904(94)90060-4

Bae, J.-S., Bhatia, S.K., 2006. High-Pressure Adsorption of Methane and Carbon Dioxide on Coal. Energy & Fuels 20, 2599–2607. https://doi.org/10.1021/ef060318y

Bhattacharya, M., Duval, G., 2016. A snapshot of the geotectonics and petroleum geology of the Durban and Zululand Basins, offshore South Africa 34, 7.

Beck, B., 2014. An update on the South African Pilot CO_2 Storage Project. Energy Procedia 63, 6188–6193. https://doi.org/10.1016/j.egypro.2014.11.650

Bishop, J.L., Koeberl, C., Kralik, C., Fröschl, H., Enolert, P.A.J., Andersen, D.W., Pieters, C.M., Wharton, R.A., 1996. Reflectance spectroscopy and geochemical analyses of Lake Hoare sediments, Antarctica: Implications for remote sensing of the Earth and Mars. Geochimica et Cosmochimica Acta 60, 765–785. https://doi.org/10.1016/0016-7037(95)00432-7

Blake, R.E., Walter, L.M., 1999. Kinetics of feldspar and quartz dissolution at 70–80°C and near-neutral pH: effects of organic acids and NaCl. Geochimica et Cosmochimica Acta 63, 2043–2059. https://doi.org/10.1016/S0016-7037(99)00072-1

Booth, J., Hong, Q., Compton, R.G., Prout, K., Payne, R.M., n.d. Gypsum Overgrowths Passivate Calcite to Acid Attack 8.

Bouchelaghem, F., 2010. A numerical and analytical study on calcite dissolution and gypsum precipitation. Applied Mathematical Modelling 14.

Bradshaw, J., Allinson, G., Bradshaw, B.E., Nguyen, V., Rigg, A.J., Spencer, L., Wilson, P., 2004. Australia's CO_2 geological storage potential and matching of emission sources to potential sinks. Energy 29, 1623–1631. https://doi.org/10.1016/j.energy.2004.03.064

Busch, A., Alles, S., Gensterblum, Y., Prinz, D., Dewhurst, D.N., Raven, M.D., Stanjek, H., Krooss, B.M., 2008. Carbon dioxide storage potential of shales. International Journal of Greenhouse Gas Control 2, 297–308. https://doi.org/10.1016/j.ijggc.2008.03.003

Campos, R., Barrios, I., Lillo, J., 2015. Experimental CO_2 injection: Study of physical changes in sandstone porous media using Hg porosimetry and 3D pore network models. Energy Reports 1, 71–79. https://doi.org/10.1016/j.egyr.2015.01.004

Cao, T., Song, Z., Wang, S., Xia, J., 2016. Characterization of pore structure and fractal dimension of Paleozoic shales from the northeastern Sichuan Basin, China. Journal of Natural Gas Science and Engineering 35, 882–895. https://doi.org/10.1016/j.jngse.2016.09.022

Cao, W., Shi, J.-Q., Durucan, S., Korre, A., 2021. Evaluation of shear slip stress transfer mechanism for induced microseismicity at In Salah CO_2 storage site. International Journal of Greenhouse Gas Control 107, 103302. https://doi.org/10.1016/j.ijggc.2021.103302

Carroll, S.A., Knauss, K.G., 2005. Dependence of labradorite dissolution kinetics on CO_2 (aq), Al(aq), and temperature. Chemical Geology 217, 213–225. https://doi.org/10.1016/j.chemgeo.2004.12.008

Chabangu, N., Beck, B., Hicks, N., Botha, G., Viljoen, J., Davids, S., Cloete, M., 2014a. The investigation of CO_2 storage potential in the Zululand Basin in South Africa. Energy Procedia 63, 2789–2799. https://doi.org/10.1016/j.egypro.2014.11.301

Chabangu, N., Beck, B., Hicks, N., Viljoen, J., Davids, S., Cloete, M., 2014b. The investigation of CO_2 storage potential in the Algoa basin in South Africa. Energy Procedia 63, 2800–2810. https://doi.org/10.1016/j.egypro.2014.11.302

Chalmers, G.R.L., Ross, D.J.K., Bustin, R.M., 2012. Geological controls on matrix permeability of Devonian Gas Shales in the Horn River and Liard basins, northeastern British Columbia, Canada. International Journal of Coal Geology 103, 120–131. https://doi.org/10.1016/j.coal.2012.05.006

Chalmers, J.M., Everall, N.J., Ellison, S., n.d. Specular Reflectance: A Convenient Tool for Polymer Characterisation by FTIR-Microscopy? 14.

Chen, Y., Zou, C., Mastalerz, M., Hu, S., Gasaway, C., Tao, X., 2015. Applications of Micro-Fourier Transform Infrared Spectroscopy (FTIR) in the Geological Sciences—A Review. IJMS 16, 30223–30250. https://doi.org/10.3390/ijms161226227

Cheng, Y., Zeng, M., Lu, Z., Du, X., Yin, H., Yang, L., 2020. Effects of Supercritical CO_2 Treatment Temperatures on Mineral Composition, Pore Structure and Functional Groups of Shale: Implications for CO_2 Sequestration. Sustainability 12, 3927. https://doi.org/10.3390/su12093927

Clarkson, C.R., Freeman, M., He, L., Agamalian, M., Melnichenko, Y.B., Mastalerz, M., Bustin, R.M., Radliński, A.P., Blach, T.P., 2012. Characterization of tight gas reservoir pore structure using USANS/SANS and gas adsorption analysis. Fuel 95, 371–385. https://doi.org/10.1016/j.fuel.2011.12.010

Crandell, L.E., Ellis, B.R., Peters, C. a., 2010. Dissolution potential of SO_2 co-injected with CO_2 in geologic sequestration. Environmental Science and Technology 44, 349–355. https://doi.org/10.1021/es902612m

Credoz, A., Bildstein, O., Jullien, M., Raynal, J., Pétronin, J.-C., Lillo, M., Pozo, C., Geniaut, G., 2009. Experimental and modeling study of geochemical reactivity between clayey

caprocks and CO_2 in geological storage conditions. Energy Procedia 1, 3445–3452. https://doi.org/10.1016/j.egypro.2009.02.135

Cui, G., Zhang, L., Tan, C., Ren, S., Zhuang, Y., Enechukwu, C., 2017. Injection of supercritical CO_2 for geothermal exploitation from sandstone and carbonate reservoirs: CO_2 –water–rock interactions and their effects. Journal of CO_2 Utilization 20, 113–128. https://doi.org/10.1016/j.jcou.2017.05.006

Curtis, M.E., Cardott, B.J., Sondergeld, C.H., Rai, C.S., 2012. Development of organic porosity in the Woodford Shale with increasing thermal maturity. International Journal of Coal Geology 103, 26–31. https://doi.org/10.1016/j.coal.2012.08.004

Dai, X., Wang, M., Wei, C., Zhang, J., Wang, X., Zou, M., 2020. Factors affecting shale microscopic pore structure variation during interaction with supercritical CO_2. Journal of CO_2 Utilization 38, 194–211. https://doi.org/10.1016/j.jcou.2020.01.021

Dawson, G.K.W., Pearce, J.K., Biddle, D., Golding, S.D., 2015. Experimental mineral dissolution in Berea Sandstone reacted with CO 2 or SO 2 – CO 2 in NaCl brine under CO 2 sequestration conditions. Chemical Geology 399, 87–97. https://doi.org/10.1016/j.chemgeo.2014.10.005

De Silva, P.N.K., Ranjith, P.G., 2012. A study of methodologies for CO 2 storage capacity estimation of saline aquifers. Fuel 93, 13–27. https://doi.org/10.1016/j.fuel.2011.07.004

de Visser, E., Hendriks, C., Barrio, M., Mølnvik, M.J., de Koeijer, G., Liljemark, S., Le Gallo, Y., 2008. Dynamis CO_2 quality recommendations. International Journal of Greenhouse Gas Control 2, 478–484. https://doi.org/10.1016/j.ijggc.2008.04.006

Ellis, B.R., Crandell, L.E., Peters, C.A., 2010. Limitations for brine acidification due to SO_2 co-injection in geologic carbon sequestration. International Journal of Greenhouse Gas Control 4, 575–582. https://doi.org/10.1016/j.ijggc.2009.11.006

Emberley, S., Hutcheon, I., Shevalier, M., Durocher, K., Mayer, B., Gunter, W.D., Perkins, E.H., 2005. Monitoring of fluid-rock interaction and CO_2 storage through produced fluid sampling at the Weyburn CO_2-injection enhanced oil recovery site, Saskatchewan,

Canada. Applied Geochemistry 20, 1131–1157. https://doi.org/10.1016/j.apgeochem.2005.02.007

Fakher, S., Imqam, A., 2020. High pressure-high temperature carbon dioxide adsorption to shale rocks using a volumetric method. International Journal of Greenhouse Gas Control 95, 102998. https://doi.org/10.1016/j.ijggc.2020.102998

Farquhar, S.M., Pearce, J.K., Dawson, G.K.W., Golab, A., Sommacal, S., Kirste, D., Biddle, D., Golding, S.D., 2015. A fresh approach to investigating CO 2 storage: Experimental CO 2 –water–rock interactions in a low-salinity reservoir system. Chemical Geology 399, 98–122. https://doi.org/10.1016/j.chemgeo.2014.10.006

Fishman, N.S., Hackley, P.C., Lowers, H.A., Hill, R.J., Egenhoff, S.O., Eberl, D.D., Blum, A.E., 2012. The nature of porosity in organic-rich mudstones of the Upper Jurassic Kimmeridge Clay Formation, North Sea, offshore United Kingdom. International Journal of Coal Geology 103, 32–50. https://doi.org/10.1016/j.coal.2012.07.012

Fourie, F.D., Allwright, A.J., Makiwane, N., Govender, N., 2017. CHARACTERISATION AND PROTECTION OF DEEP AQUIFERS IN SOUTH AFRICA: CONSOLIDATION OF DATA SOURCES 12.

Gale, J., 2009. Impure thoughts. International Journal of Greenhouse Gas Control 3, 1–2. https://doi.org/10.1016/j.ijggc.2008.11.001

Gao, S., Wang, Y., Jia, L., Wang, H., Yuan, J., Wang, X., 2013. CO_2-H2O-coal interaction of CO_2 storage in coal beds. International Journal of Mining Science and Technology 23, 525–529. https://doi.org/10.1016/j.ijmst.2013.07.010

Gaus, I., 2010. Role and impact of CO_2-rock interactions during CO_2 storage in sedimentary rocks. International Journal of Greenhouse Gas Control 4, 73–89. https://doi.org/10.1016/j.ijggc.2009.09.015

Ghaderi, S.M., Keith, D.W., Lavoie, R., Leonenko, Y., 2011. Evolution of hydrogen sulfide in sour saline aquifers during carbon dioxide sequestration. International Journal of Greenhouse Gas Control 5, 347–355. https://doi.org/10.1016/j.ijggc.2010.09.008

Ghosh, R., Sen, M.K., Vedanti, N., 2015. Quantitative interpretation of CO_2 plume from Sleipner (North Sea), using post-stack inversion and rock physics modeling. International Journal of Greenhouse Gas Control 32, 147–158. https://doi.org/10.1016/j.ijggc.2014.11.002

Gilfillan, S.M.V., Lollar, B.S., Holland, G., Blagburn, D., Stevens, S., Schoell, M., Cassidy, M., Ding, Z., Zhou, Z., Lacrampe-Couloume, G., Ballentine, C.J., 2009. Solubility trapping in formation water as dominant CO_2 sink in natural gas fields. Nature 458, 614–618. https://doi.org/10.1038/nature07852

Gimeno, B., Artal, M., Velasco, I., Blanco, S.T., Fernández, J., 2017. Influence of SO_2 on CO_2 storage for CCS technology: Evaluation of CO_2/SO_2 co-capture. Applied Energy 206, 172–180. https://doi.org/10.1016/j.apenergy.2017.08.048

Gimeno, B., Artal, M., Velasco, I., Fernández, J., Blanco, S.T., 2018. Influence of SO_2 on CO_2 Transport by Pipeline for Carbon Capture and Storage Technology: Evaluation of CO_2/SO_2 Cocapture. Energy Fuels 32, 8641–8657. https://doi.org/10.1021/acs.energyfuels.8b01666

Glezakou, V.-A., Peter McGrail, B., Todd Schaef, H., 2012. Molecular interactions of SO_2 with carbonate minerals under co-sequestration conditions: A combined experimental and theoretical study. Geochimica et Cosmochimica Acta 92, 265–274. https://doi.org/10.1016/j.gca.2012.06.015

Golding, S.D., Uysal, I.T., Boreham, C.J., Kirste, D., Baublys, K.A., Esterle, J.S., 2011. Adsorption and mineral trapping dominate CO_2 storage in coal systems. Energy Procedia 4, 3131–3138. https://doi.org/10.1016/j.egypro.2011.02.227

Goodman, A., Sanguinito, S., Tkach, M., Natesakhawat, S., Kutchko, B., Fazio, J., Cvetic, P., 2019. Investigating the role of water on CO_2-Utica Shale interactions for carbon storage and shale gas extraction activities – Evidence for pore scale alterations. Fuel 242, 744–755. https://doi.org/10.1016/j.fuel.2019.01.091

Goodman, A., Sanguinito, S., Tkach, M., Natesakhawat, S., Kutchko, B., Fazio, J., Cvetic, P., 2019. Investigating the role of water on CO_2-Utica Shale interactions for carbon storage

and shale gas extraction activities – Evidence for pore scale alterations. Fuel 242, 744–755. https://doi.org/10.1016/j.fuel.2019.01.091

Goodman, A.L., Favors, R.N., Hill, M.M., Larsen, J.W., 2005. Structure changes in Pittsburgh no. 8 coal caused by sorption of CO_2 gas. Energy and Fuels 19, 1759–1760. https://doi.org/10.1021/ef050051n

Gudbrandsson, S., Wolff-Boenisch, D., Gislason, S.R., Oelkers, E.H., 2014. Experimental determination of plagioclase dissolution rates as a function of its composition and pH at 22°C. Geochimica et Cosmochimica Acta 139, 154–172. https://doi.org/10.1016/j.gca.2014.04.028

Gudbrandsson, S., Wolff-Boenisch, D., Gislason, S.R., Oelkers, E.H., 2011. An experimental study of crystalline basalt dissolution from 2⩽pH⩽11 and temperatures from 5 to 75°C. Geochimica et Cosmochimica Acta 75, 5496–5509. https://doi.org/10.1016/j.gca.2011.06.035

Guiliano, M., Asia, L., Onoratini, G., Mille, G., 2007. Applications of diamond crystal ATR FTIR spectroscopy to the characterization of ambers. Spectrochimica Acta Part A: Molecular and Biomolecular Spectroscopy 67, 1407–1411. https://doi.org/10.1016/j.saa.2006.10.033

Gunter, W., Bachu, S., Benson, S., 2004. The Role of Hydrogeological and Geochemical Trapping in Sedimentary Basins for Secure Geological Storage of Carbon Dioxide. Geological Society, London, Special Publications 233, 129–145. https://doi.org/10.1144/GSL.SP.2004.233.01.09

Guo, X., Li, Y., Liu, R., Wang, Q., 2014. Characteristics and controlling factors of micropore structures of the Longmaxi Shale in the Jiaoshiba area, Sichuan Basin. Natural Gas Industry B 1, 165–171. https://doi.org/10.1016/j.ngib.2014.11.007

Gupta, V., Macmillan, I.C., Surie, G., 2004. Entrepreneurial leadership: developing and measuring a cross-cultural construct 19, 241–260. https://doi.org/10.1016/S0883-9026(03)00040-5

Hamza, A., Hussein, I.A., Al-Marri, M.J., Mahmoud, M., Shawabkeh, R., 2021. Impact of clays on CO_2 adsorption and enhanced gas recovery in sandstone reservoirs. International

Journal of Greenhouse Gas Control 106, 103286. https://doi.org/10.1016/j.ijggc.2021.103286

Hangx, S., van der Linden, A., Marcelis, F., Bauer, A., 2013. The effect of CO 2 on the mechanical properties of the Captain Sandstone: Geological storage of CO 2 at the Goldeneye field (UK). International Journal of Greenhouse Gas Control 19, 609–619. https://doi.org/10.1016/j.ijggc.2012.12.016

Head, M.J., Riding, J.B., Eidvin, T., Chadwick, R.A., 2004. Palynological and foraminiferal biostratigraphy of (Upper Pliocene) Nordland Group mudstones at Sleipner, northern North Sea. Marine and Petroleum Geology 21, 277–297. https://doi.org/10.1016/j.marpetgeo.2003.12.002

Heeschen, K., Risse, A., Ostertag-Henning, C., Stadler, S., 2011. Importance of co-captured gases in the underground storage of CO 2: Quantification of mineral alterations in chemical experiments. Energy Procedia 4, 4480–4486. https://doi.org/10.1016/j.egypro.2011.02.403

Hellevang, H., Pham, V.T.H., Aagaard, P., 2013. Kinetic modelling of CO_2–water–rock interactions. International Journal of Greenhouse Gas Control 15, 3–15. https://doi.org/10.1016/j.ijggc.2013.01.027

Herbert, T.D., Tom, B.A., Burnett, C., 1992. Precise major component determinations in deep-sea sediments using Fourier Transform Infrared Spectroscopy. Geochimica et Cosmochimica Acta 56, 1759–1763. https://doi.org/10.1016/0016-7037(92)90242-B

Hermanrud, C., Andresen, T., Eiken, O., Hansen, H., Janbu, A., Lippard, J., Bol\aas, H.N., Simmenes, T.H., Teige, G.M.G., Østmo, S., 2009. Storage of CO_2 in saline aquifers-Lessons learned from 10 years of injection into the Utsira Formation in the Sleipner area. Energy Procedia 1, 1997–2004. https://doi.org/10.1016/j.egypro.2009.01.260

Herzog, H., Golomb, D., 2004. Carbon Capture and Storage from Fossil Fuel Use. Encyclopedia of Energy 1, 277–287. https://doi.org/10.1016/b0-12-176480-x/00422-8

Hicks, N., 2016.

Hohne, D., de Lange, F., Esterhuyse, S., Lollar, B.S., 2019. Case study: methane gas in a groundwater system located in a dolerite ring structure in the Karoo Basin; South Africa. Geological Society of South Africa 12.

Holloway, S., 1997. An overview of the underground disposal of carbon dioxide. Energy Conversion and Management 38, 193–198.

Hsieh, P.-S., Tien, N.-C., Lin, C.-K., Lin, W., Lu, H.-Y., 2017. A multi-sequestration concept of CO 2 geological storage: Shale-Sandstone-Basalt system in Northwestern Taiwan. International Journal of Greenhouse Gas Control 64, 137–151. https://doi.org/10.1016/j.ijggc.2017.07.008

IEA, 2011. Effects of Impurities on Geological Storage of CO_2.

IPCC, 2005. Special Report on CO_2 Capture and Storage, Intergovernmental Panel on Climate Change. https://doi.org/10.1002/anie.201000431

Irfan, M.F., Bisson, T.M., Bobicki, E., Arguelles-Vivas, F., Xu, Z., Liu, Q., Babadagli, T., 2018. CO 2 storage in saline aquifers by dissolution and residual trapping under supercritical conditions: An experimental investigation. Colloids and Surfaces A: Physicochemical and Engineering Aspects 548, 37–45. https://doi.org/10.1016/j.colsurfa.2018.03.062

Jiang, T., Xu, K., 1995. FTIR study of ultradispersed diamond powder synthesized by explosive detonation. Carbon 33, 1663–1671. https://doi.org/10.1016/0008-6223(95)00115-1

Jiang, X., 2011. A review of physical modelling and numerical simulation of long-term geological storage of CO_2. Applied Energy 10.

Jiang, Y., Luo, Y., Lu, Y., Qin, C., Liu, H., 2016. Effects of supercritical CO_2 treatment time, pressure, and temperature on microstructure of shale. Energy 97, 173–181. https://doi.org/10.1016/j.energy.2015.12.124

Kampman, N., Bickle, M., Becker, J., Assayag, N., Chapman, H., 2009. Feldspar dissolution kinetics and Gibbs free energy dependence in a CO_2-enriched groundwater system,

Green River, Utah. Earth and Planetary Science Letters 284, 473–488. https://doi.org/10.1016/j.epsl.2009.05.013

Klima, J., Kratochvilovfi, K., Ludv, J., n.d. FTIR spectro-photoelectrochemical cell with adjustable solution layer thickness. Photocurrent transients at photoexcited TiO 2 polycrystalline electrodes 5.

Kloprogge, J., Frost, R., 2004. Infrared emission spectroscopy of clay minerals: in the application of vibrational spectroscopy to clay minerals and layered double hydroxides.

Knauss, K.G., Johnson, J.W., Steefel, C.I., 2005. Evaluation of the impact of CO_2, co-contaminant gas, aqueous fluid, and reservoir rock interactions on the geologic sequestration of CO_2. Chemical Geology 217, 339–350. https://doi.org/10.1016/j.chemgeo.2004.12.017

Koenen, M., Tambach, T.J., Neele, F.P., 2011. Geochemical effects of impurities in CO_2 on a sandstone reservoir. Energy Procedia 4, 5343–5349. https://doi.org/10.1016/j.egypro.2011.02.516

Krohn, C.E., 1988. Fractal measurements of sandstones, shales, and carbonates. Journal of Geophysical Research: Solid Earth 93, 3297–3305. https://doi.org/10.1029/JB093iB04p03297

Krooss, B.M., Van Bergen, F., Gensterblum, Y., Siemons, N., Pagnier, H.J.M., David, P., 2002. High-pressure methane and carbon dioxide adsorption on dry and moisture-equilibrated Pennsylvanian coals. International Journal of Coal Geology 51, 69–92. https://doi.org/10.1016/S0166-5162(02)00078-2

Kuila, U., Prasad, M., 2013. Specific surface area and pore-size distribution in clays and shales. Geophysical Prospecting 61, 341–362. https://doi.org/10.1111/1365-2478.12028

Kutchko, B., Sanguinito, S., Natesakhawat, S., Cvetic, P., Culp, J.T., Goodman, A., 2020. Quantifying pore scale and matrix interactions of $SCCO_2$ with the Marcellus shale. Fuel 266, 116928. https://doi.org/10.1016/j.fuel.2019.116928

Labani, M.M., Rezaee, R., Saeedi, A., Hinai, A.A., 2013. Evaluation of pore size spectrum of gas shale reservoirs using low pressure nitrogen adsorption, gas expansion and mercury

porosimetry: A case study from the Perth and Canning Basins, Western Australia. Journal of Petroleum Science and Engineering 112, 7–16. https://doi.org/10.1016/j.petrol.2013.11.022

Lahann, R., Mastalerz, M., Rupp, J.A., Drobniak, A., 2013. Influence of CO_2 on New Albany Shale composition and pore structure. International Journal of Coal Geology 108, 2–9. https://doi.org/10.1016/j.coal.2011.05.004

Lai, J., Wang, G., Wang, Z., Chen, J., Pang, X., Wang, S., Zhou, Z., He, Z., Qin, Z., Fan, X., 2018. A review on pore structure characterization in tight sandstones. Earth-Science Reviews 177, 436–457. https://doi.org/10.1016/j.earscirev.2017.12.003

Lane, M.D., 2007. Mid-infrared emission spectroscopy of sulfate and sulfate-bearing minerals. American Mineralogist 92, 1–18. https://doi.org/10.2138/am.2007.2170

Larsen, J.W., 2004. The effects of dissolved CO_2 on coal structure and properties. International Journal of Coal Geology 57, 63–70. https://doi.org/10.1016/j.coal.2003.08.001

Lee, J.Y., Keener, T.C., Yang, Y.J., 2009. Potential flue gas impurities in carbon dioxide streams separated from coal-fired power plants. Journal of the Air and Waste Management Association 59, 725–732. https://doi.org/10.3155/1047-3289.59.6.725

Lei, Q., Zhang, L., Tang, H., Zhao, Y., Chen, M., Xie, C., 2020. Describing the Full Pore Size Distribution of Tight Sandstone and Analyzing the Impact of Clay Type on Pore Size Distribution. Geofluids 2020, 1–20. https://doi.org/10.1155/2020/5208129

Leung, D.Y.C., Caramanna, G., Maroto-Valer, M.M., 2014. An overview of current status of carbon dioxide capture and storage technologies. Renewable and Sustainable Energy Reviews 39, 426–443. https://doi.org/10.1016/j.rser.2014.07.093

Li, D., Jiang, X., 2014. A numerical study of the impurity effects of nitrogen and sulphur dioxide on the solubility trapping of carbon dioxide geological storage. Applied Energy 128, 60–74. https://doi.org/10.1016/j.apenergy.2014.04.051

Linol, B., Chere, N., Muedi, T., J., de Wit, M., Nengovhela, V., 2016. Deep Borehole Lithostratigraphy and Basin Structure of the Southern Karoo Basin Re-Visited. Regional Geology Reviews.

Liu, H., Shao, Y., 2010. Predictions of the impurities in the CO_2 stream of an oxy-coal combustion plant. Applied Energy 87, 3162–3170. https://doi.org/10.1016/j.apenergy.2010.04.014

Liu, Y., Wilcox, J., 2012. Molecular simulation of CO_2 adsorption in micro- and mesoporous carbons with surface heterogeneity. International Journal of Coal Geology 104, 83–95. https://doi.org/10.1016/j.coal.2012.04.007

Loring, J.S., Chen, J., Bénézeth, P., Qafoku, O., Ilton, E.S., Washton, N.M., Thompson, C.J., Martin, P.F., McGrail, B.P., Rosso, K.M., Felmy, A.R., Schaef, H.T., 2015. Evidence for Carbonate Surface Complexation during Forsterite Carbonation in Wet Supercritical Carbon Dioxide. Langmuir 31, 7533–7543. https://doi.org/10.1021/acs.langmuir.5b01052

Loucks, R.G., Reed, R.M., Ruppel, S.C., Jarvie, D.M., 2012. MORPHOLOGY, GENESIS, AND DISTRIBUTION OF NANOMETER-SCALE PORES IN SILICEOUS MUDSTONES OF THE MISSISSIPPIAN BARNETT SHALE. Journal of Sedimentary Research 79, 848–861.

Lu, H.-Y., Lin, C.-K., Lin, W., Liou, T.-S., Chen, W.-F., Chang, P.-Y., 2011. A natural analogue for CO_2 mineral sequestration in Miocene basalt in the Kuanhsi-Chutung area, Northwestern Taiwan. International Journal of Greenhouse Gas Control 5, 1329–1338. https://doi.org/10.1016/j.ijggc.2011.05.037

Lu, X., Jin, D., Wei, S., Zhang, M., Zhu, Q., Shi, X., Deng, Z., Guo, W., Shen, W., 2015. Competitive adsorption of a binary CO_2–CH4 mixture in nanoporous carbons: effects of edge-functionalization. Nanoscale 7, 1002–1012. https://doi.org/10.1039/C4NR05128A

Lucier, A., Zoback, M., 2008. Assessing the economic feasibility of regional deep saline aquifer CO_2 injection and storage: A geomechanics-based workflow applied to the Rose Run sandstone in Eastern Ohio, USA. International journal of greenhouse gas control, 2. 230-247.

Luo, X., Ren, X., Wang, S., 2018. Supercritical CO_2-water-shale Interactions under Supercritical CO_2 Stimulation Conditions. Energy Procedia 144, 182–185. https://doi.org/10.1016/j.egypro.2018.06.024

Makiwane, N., 2019. Characterisation Of The Deep Aquifers Of South Africa – The Karoo Supergroup And Table Mountain Group. Dissertation, University of Free State. 134.

Marsh, H., 1987. Adsorption methods to study microporpsity in coals and carbons. Carbon 25, 49–58.

Mavhengere, P., Maphala, T., Wagner, N., 2015. Physical and structural effects of carbon dioxide storage on vitrinite-rich coal particles under subcritical and supercritical conditions. International Journal of Coal Geology 150–151, 1–6.

Mavhengere, P., Wagner, N., Malumbazo, N., 2021. The effects of long-term supercritical CO_2 exposure on Zululand Basin core samples. Energy 220, 119806. https://doi.org/10.1016/j.energy.2021.119806

Mayerhöfer, T., 2004. Modelling IR-spectra of single-phase polycrystalline materials with random orientation - A unified approach. Vibrational Spectroscopy - VIB SPECTROSC 35, 67–76. https://doi.org/10.1016/j.vibspec.2003.11.011

McCarthy, S.J., Meijs, G.F., Mitchell, N., Gunatillake, P.A., Heath, G., Brandwood, A., Schindhelm, K., 1997. In-tivo degradation of polyurethanes: transmission-FTIR microscopic characterization of polyurethanes sectioned by cryomicrotomy 18, 23.

Melliti, E., 2021. Effect of Fe2+ ions on gypsum precipitation during bulk crystallization of reverse osmosis concentrates 11.

Metz, V., Amram, K., Ganor, J., 2005. Stoichiometry of smectite dissolution reaction. Geochimica et Cosmochimica Acta 69, 1755–1772. https://doi.org/10.1016/j.gca.2004.09.027

Mirzaeian, M., Hall, P.J., 2006. The interactions of coal with CO_2 and its effects on coal structure. Energy and Fuels 20, 2022–2027.

Moosavi, S.A., Goshtasbi, K., Kazemzadeh, E., Bakhtiari, H.A., Esfahani, M.R., Vali, J., 2014. Relationship between porosity and permeability with stress using pore volume

compressibility characteristic of reservoir rocks. Arabian Journal of Geosciences 7, 231–239. https://doi.org/10.1007/s12517-012-0760-x

Mouzakis, K.M., Navarre-Sitchler, A.K., Rother, G., Bañuelos, J.L., Wang, X., Kaszuba, J.P., Heath, J.E., Miller, Q.R.S., Alvarado, V., McCray, J.E., 2016. Experimental Study of Porosity Changes in Shale Caprocks Exposed to CO_2 -Saturated Brines I: Evolution of Mineralogy, Pore Connectivity, Pore Size Distribution, and Surface Area. Environmental Engineering Science 33, 725–735. https://doi.org/10.1089/ees.2015.0588

Munz, I.A., Brandvoll, Ø., Haug, T.A., Iden, K., Smeets, R., Kihle, J., Johansen, H., 2012. Mechanisms and rates of plagioclase carbonation reactions. Geochimica et Cosmochimica Acta 77, 27–51. https://doi.org/10.1016/j.gca.2011.10.036

Nakamura, K., Nishimura, Y., Zetterlund, P., Hatakeyama, T., Hatakeyama, H., 1996. TG-FTIR studies on biodegradable polyurethanes containing mono- and disaccharide components. Thermochimica Acta 282–283, 433–441. https://doi.org/10.1016/0040-6031(96)02834-1

Nghiem, L., Yang, C., Shrivastava, V., Kohse, B., Hassam, M., Card, C., 2009. Risk mitigation through the optimization of residual gas and solubility trapping for CO_2 storage in saline aquifers. Energy Procedia 8.

Okamoto, I., Li, X., Ohsumi, T., 2005. Effect of supercritical CO_2 as the organic solvent on cap rock sealing performance for underground storage. Energy 30, 2344–2351. https://doi.org/10.1016/j.energy.2003.10.025

Okolo, G.N., Everson, R.C., Neomagus, H.W.J.P., Roberts, M.J., Sakurovs, R., 2015. Comparing the porosity and surface areas of coal as measured by gas adsorption, mercury intrusion and SAXS techniques. Fuel 141, 293–304. https://doi.org/10.1016/j.fuel.2014.10.046

Oxburgh, R., Drever, J.I., Sun, Y.-T., 1994. Mechanism of plagioclase dissolution in acid solution at 25°C. Geochimica et Cosmochimica Acta 58, 661–669. https://doi.org/10.1016/0016-7037(94)90496-0

Pan, Y., Hui, D., Luo, P., Zhang, Y., Zhang, L., Sun, L., 2018. In fl uences of subcritical and supercritical CO 2 treatment on the pore structure characteristics of marine and terrestrial shales. Journal of CO_2 Utilization 28, 152–167. https://doi.org/10.1016/j.jcou.2018.09.016

Pearce, J.K., Kirste, D.M., Dawson, G.K.W., Farquhar, S.M., Biddle, D., Golding, S.D., Rudolph, V., 2015. SO_2 impurity impacts on experimental and simulated CO 2 -water-reservoir rock reactions at carbon storage conditions. Chemical Geology 399, 65–86. https://doi.org/10.1016/j.chemgeo.2014.10.028

Pearce, J.K., Law, A.C.K., Dawson, G.K.W., Golding, S.D., 2015. SO_2–CO_2 and pure CO_2 reactivity of ferroan carbonates at carbon storage conditions. Chemical Geology 411, 112–124. https://doi.org/10.1016/j.chemgeo.2015.07.001

Perera, M.S.A., Ranjith, P.G., Choi, S.K., Airey, D., 2011. The effects of sub-critical and super-critical carbon dioxide adsorption-induced coal matrix swelling on the permeability of naturally fractured black coal. Energy 36, 6442–6450. https://doi.org/10.1016/j.energy.2011.09.023

Pham, V.T.H., Lu, P., Aagaard, P., Zhu, C., Hellevang, H., 2011. On the potential of CO_2–water–rock interactions for CO_2 storage using a modified kinetic model. International Journal of Greenhouse Gas Control 5, 1002–1015. https://doi.org/10.1016/j.ijggc.2010.12.002

Pruess, K., García, J., 2002. Multiphase flow dynamics during CO_2 disposal into saline aquifers. Environmental Geology 42, 282–295. https://doi.org/10.1007/s00254-001-0498-3

Qiao, J., Zeng, J., Jiang, S., Ma, Y., Feng, S., Xie, H., Wang, Y., Hu, H., 2020. Role of pore structure in the percolation and storage capacities of deeply buried sandstone reservoirs: A case study of the Junggar Basin, China. Marine and Petroleum Geology 113, 104129. https://doi.org/10.1016/j.marpetgeo.2019.104129

Rani, S., Prusty, B.K., Pal, S.K., 2020. Characterization of shales from Damodar valley coalfields for CH4 recovery and CO_2 sequestration. Environmental Technology & Innovation 18, 100739. https://doi.org/10.1016/j.eti.2020.100739

Rao, A.B., Rubin, E.S., 2002. A Technical, Economic, and Environmental Assessment of Amine-Based CO 2 Capture Technology for Power Plant Greenhouse Gas Control. Environmental Science & Technology 36, 4467–4475. https://doi.org/10.1021/es0158861

Reichle, D.E., Houghton, J., Kane, R., 1999. Review of Carbon Sequestration Science and Technology Opportunities by the Us Department of Energy. Ornl.Gov.

Reig, F.B., Adelantado, J.V.G., Moya Moreno, M.C.M., 2002. FTIR quantitative analysis of calcium carbonate (calcite) and silica (quartz) mixtures using the constant ratio method. Application to geological samples. Talanta 58, 811–821. https://doi.org/10.1016/s0039-9140(02)00372-7

Rezaee, R., Saeedi, A., Clennell, B., 2012. Tight gas sands permeability estimation from mercury injection capillary pressure and nuclear magnetic resonance data. Journal of Petroleum Science and Engineering 88–89, 92–99. https://doi.org/10.1016/j.petrol.2011.12.014

Richiano, S., Varela, A.N., Gómez-Peral, L.E., Cereceda, A., Poiré, D.G., 2015. Composition of the Lower Cretaceous source rock from the Austral Basin (Río Mayer Formation, Patagonia, Argentina): Regional implication for unconventional reservoirs in the Southern Andes. Marine and Petroleum Geology 66, 764–790. https://doi.org/10.1016/j.marpetgeo.2015.07.018

Rimmelé, G., Barlet-Gouédard, V., Renard, F., 2010. Evolution of the Petrophysical and Mineralogical Properties of Two Reservoir Rocks Under Thermodynamic Conditions Relevant for CO_2 Geological Storage at 3 km Depth. Oil Gas Sci. Technol. – Rev. IFP 65, 565–580. https://doi.org/10.2516/ogst/2009071

Řimnáčová, D., Weishauptová, Z., Přibyl, O., Sýkorová, I., René, M., 2020. Effect of shale properties on CH4 and CO_2 sorption capacity in Czech Silurian shales. Journal of Natural Gas Science and Engineering 80, 103377. https://doi.org/10.1016/j.jngse.2020.103377

Romanov, V., Soong, Y., 2008. Long-term CO_2 sorption on upper freeport coal powder and lumps. Energy and Fuels 22, 1167–1169. https://doi.org/10.1021/ef700491t

Rosenbauer, R.J., Koksalan, T., Palandri, J.L., 2005. Experimental investigation of CO_2–brine–rock interactions at elevated temperature and pressure: Implications for CO_2 sequestration in deep-saline aquifers. Fuel Processing Technology 86, 1581–1597. https://doi.org/10.1016/j.fuproc.2005.01.011

Ross, D.J.K., Bustin, M., 2008. Characterizing the shale gas resource potential of Devonian–Mississippian strata in the Western Canada sedimentary basin: Application of an integrated formation evaluation. AAPG Bulletin.

Ross, D.J.K., Bustin, M., 2007. Impact of mass balance calculations on adsorption capacities in microporous shale gas reservoirs. Fuel 86, 2696–2706. https://doi.org/10.1016/j.fuel.2007.02.036

Rubasinghege, G., Grassian, V.H., 2013. Role(s) of adsorbed water in the surface chemistry of environmental interfaces. Chem. Commun. 49, 3071–3094. https://doi.org/10.1039/C3CC38872G

Sakurovs, R., Day, S., Weir, S., Duffy, G., 2007. Effect of coal properties on CO_2 sorption capacity under supercritical conditions. 24th Annual International Pittsburgh Coal Conference 2007, PCC 2007 3, 1386–1403. https://doi.org/10.1016/S1750-5836(07)00120-X

Schmitt, M., Fernandes, C.P., Wolf, F.G., Bellini da Cunha Neto, J.A., Rahner, C.P., Santiago dos Santos, V.S., 2015. Characterization of Brazilian tight gas sandstones relating permeability and Angstrom-to micron-scale pore structures. Journal of Natural Gas Science and Engineering 27, 785–807. https://doi.org/10.1016/j.jngse.2015.09.027

Schuttlefield, J.D., Cox, D., Grassian, V.H., 2007. An investigation of water uptake on clays minerals using ATR-FTIR spectroscopy coupled with quartz crystal microbalance measurements. J. Geophys. Res. 112, D21303. https://doi.org/10.1029/2007JD008973

Şenel, I.G., Gürz, A.G., Yücel, H., Kandas, A.W., Sarofim, A.F., 2001. Characterization of pore structure of Turkish coals. Energy and Fuels 15, 331–338. https://doi.org/10.1021/ef000081k

Shi, Z., Sun, L., Haljasmaa, I., Harbert, W., Sanguinito, S., Tkach, M., Goodman, A., Tsotsis, T.T., Jessen, K., 2019. Impact of Brine/CO_2 exposure on the transport and mechanical

properties of the Mt Simon sandstone. Journal of Petroleum Science and Engineering 177, 295–305. https://doi.org/10.1016/j.petrol.2019.01.112

Stuart Haszeldine, R., 2009. Carbon capture and storage: How Green Can Black Be? Sciencemag 325, 1647–1652. https://doi.org/10.1016/j.enpol.2008.09.058

Tan, J., Horsfield, B., Fink, R., Krooss, B., Schulz, H.-M., Rybacki, E., Zhang, J., Boreham, C.J., van Graas, G., Tocher, B.A., 2014. Shale Gas Potential of the Major Marine Shale Formations in the Upper Yangtze Platform, South China, Part III: Mineralogical, Lithofacial, Petrophysical, and Rock Mechanical Properties. Energy Fuels 28, 2322–2342. https://doi.org/10.1021/ef4022703

Theodosoglou, E., Koroneos, A., Soldatos, T., Zorba, T., Paraskevopoulos, K.M., 2017. COMPARATIVE FOURIER TRANSFORM INFRARED AND X-RAY POWDER DIFFRACTION ANALYSIS OF NATURALLY OCCURRED K-FELDSPARS. geosociety 43, 2752. https://doi.org/10.12681/bgsg.11681

Thommes, M., Kaneko, K., Neimark, A.V., Olivier, J.P., Rodriguez-Reinoso, F., Rouquerol, J., Sing, K.S.W., 2015. Physisorption of gases, with special reference to the evaluation of surface area and pore size distribution (IUPAC Technical Report). Pure and Applied Chemistry 87, 1051–1069. https://doi.org/10.1515/pac-2014-1117

Thompson, C.J., Loring, J.S., Rosso, K.M., Wang, Z., 2013. Comparative reactivity study of forsterite and antigorite in wet supercritical CO_2 by in situ infrared spectroscopy. International Journal of Greenhouse Gas Control 18, 246–255. https://doi.org/10.1016/j.ijggc.2013.07.007

Thyberg, B., Jahren, J., Winje, T., Bjørlykke, K., Faleide, J.I., Marcussen, Ø., 2010. Quartz cementation in Late Cretaceous mudstones, northern North Sea: Changes in rock properties due to dissolution of smectite and precipitation of micro-quartz crystals. Marine and Petroleum Geology 27, 1752–1764. https://doi.org/10.1016/j.marpetgeo.2009.07.005

Torp, T.A., Gale, J., 2004. Demonstrating storage of CO_2 in geological reservoirs: The Sleipner and SACS projects. Energy 29, 1361–1369. https://doi.org/10.1016/j.energy.2004.03.104

Valle, L.M., Rodríguez, R., Grima, C., Martínez, C., 2018. Effects of supercritical CO_2 injection on sandstone wettability and capillary trapping. International Journal of Greenhouse Gas Control 78, 341–348. https://doi.org/10.1016/j.ijggc.2018.09.005

van Soest, H.L., den Elzen, M.G.J., van Vuuren, D.P., 2021. Net-zero emission targets for major emitting countries consistent with the Paris Agreement. Nat Commun 12, 2140. https://doi.org/10.1038/s41467-021-22294-x

Viljoen, J.H.A., Stapelberg, F.D.J., Cloete, M., 2010. Technical report on the geological storage of carbon dioxide.

Vu, H.P., Black, J.R., Haese, R.R., 2018. The geochemical effects of O_2 and SO_2 as CO_2 impurities on fluid-rock reactions in a CO_2 storage reservoir. International Journal of Greenhouse Gas Control 68, 86–98. https://doi.org/10.1016/j.ijggc.2017.11.001

Wang, J., Ryan, D., Anthony, E.J., Wigston, A., Basava-Reddi, L., Wildgust, N., 2012. The effect of impurities in oxyfuel flue gas on CO_2 storage capacity. International Journal of Greenhouse Gas Control 11, 158–162. https://doi.org/10.1016/j.ijggc.2012.08.002

Wang, J., Ryan, D., Anthony, E.J., Wildgust, N., Aiken, T., 2011. Effects of impurities on CO_2 transport, injection, and storage. Energy Procedia 4, 3071–3078. https://doi.org/10.1016/j.egypro.2011.02.219

Wang, X., Wang, X., Hu, W., Wan, Y., Cao, J., Lv, C., Wang, R., Cui, M., 2017. Supercritical CO_2 -involved water–rock interactions at 85°C and partial pressures of 10–20 MPa: Sequestration and enhanced oil recovery. Energy Exploration & Exploitation 35, 237–258. https://doi.org/10.1177/0144598716687933

Ward, C.R., & Taylor, J.C. (1999). Quantitative mineralogical analysis of sandstones using x-ray diffraction techniques. In Hubble, T.C.T. (Ed.). 15th Australian Geological Convention Abstracts no 59, (p. 577). Australia

Weishauptová, Z., Přibyl, O., Sýkorová, I., René, M., 2017. Effect of the properties of Silurian shales from the Barrandian Basin on their methane sorption potential. Fuel 203, 68–81. https://doi.org/10.1016/j.fuel.2017.04.087

Wilke, F.D.H., 2012. On the interaction of pure and impure supercritical CO_2 with rock forming minerals in saline aquifers: An experimental geochemical approach. Applied Geochemistry 8.

Wilkins, S.J., Compton, R.G., Taylor, M.A., Viles, H.A., n.d. Channel Flow Cell Studies of the Inhibiting Action of Gypsum on the Dissolution Kinetics of Calcite: A Laboratory Approach with Implications for Field Monitoring 8.

Wollenweber, J., Alles, S., Busch, A., Krooss, B.M., Stanjek, H., Littke, R., 2010. Experimental investigation of the CO_2 sealing efficiency of caprocks. International Journal of Greenhouse Gas Control 4, 231–241. https://doi.org/10.1016/j.ijggc.2010.01.003

Wright, I.W., Ringrose, P.S., Mathieson, A.S., Eiken, O., 2009. An Overview of Active Large-Scale CO_2 Storage Projects. https://doi.org/10.2118/127096-MS

Wu, S., Zou, C., Ma, D., Zhai, X., Yu, H., Yu, Z., 2019. Reservoir property changes during CO_2–brine flow-through experiments in tight sandstone: Implications for CO_2 enhanced oil recovery in the Triassic Chang 7 Member tight sandstone, Ordos Basin, China. Journal of Asian Earth Sciences 179, 200–210. https://doi.org/10.1016/j.jseaes.2019.05.002

Xi, K., Cao, Y., Haile, B.G., Zhu, R., Jahren, J., Bjørlykke, K., Zhang, X., Hellevang, H., 2016. How does the pore-throat size control the reservoir quality and oiliness of tight sandstones? The case of the Lower Cretaceous Quantou Formation in the southern Songliao Basin, China. Marine and Petroleum Geology 76, 1–15. https://doi.org/10.1016/j.marpetgeo.2016.05.001

Xiao, D., Lu, S., Yang, J., Zhang, L., Li, B., 2017. Classifying Multiscale Pores and Investigating Their Relationship with Porosity and Permeability in Tight Sandstone Gas Reservoirs. Energy Fuels 31, 9188–9200. https://doi.org/10.1021/acs.energyfuels.7b01487

Xu, H., Van Deventer, J.S.J., 2002. Microstructural characterisation of geopolymers synthesised from kaolinite/stilbite mixtures using XRD, MAS-NMR, SEM/EDX,

TEM/EDX, and HREM. Cement and Concrete Research 32, 1705–1716. https://doi.org/10.1016/S0008-8846(02)00859-1

Xu, R., Li, R., Ma, J., He, D., Jiang, P., 2017. Effect of Mineral Dissolution/Precipitation and CO 2 Exsolution on CO 2 transport in Geological Carbon Storage. Acc. Chem. Res. 50, 2056–2066. https://doi.org/10.1021/acs.accounts.6b00651

Xu, T., Apps, J.A., Pruess, K., 2005. Mineral sequestration of carbon dioxide in a sandstone-shale system. Chemical Geology 217, 295–318. https://doi.org/10.1016/j.chemgeo.2004.12.015

Xu, T., Apps, J.A., Pruess, K., 2004. Numerical simulation of CO 2 disposal by mineral trapping in deep aquifers 19, 917–936. https://doi.org/10.1016/j.apgeochem.2003.11.003

Xu, T., Apps, J.A., Pruess, K., Yamamoto, H., 2007. Numerical modeling of injection and mineral trapping of CO 2 with H 2 S and SO 2 in a sandstone formation 242, 319–346. https://doi.org/10.1016/j.chemgeo.2007.03.022

Yang, F., 2016. Pore structure characteristics of lower Silurian shales in the southern Sichuan Basin, China: Insights to pore development and gas storage mechanism. International Journal of Coal Geology 13.

Yang, K., Lu, X., Lin, Y., Neimark, A.V., 2011. Effects of CO_2 adsorption on coal deformation during geological sequestration. Journal of Geophysical Research: Solid Earth 116, 1–11. https://doi.org/10.1029/2010JB008002

Yin, H., Zhou, J., Jiang, Y., Xian, X., Liu, Q., 2016. Physical and structural changes in shale associated with supercritical CO 2 exposure. Fuel 184, 289–303. https://doi.org/10.1016/j.fuel.2016.07.028

Yin, H., Zhou, J., Jiang, Y., Xian, X., Liu, Q., 2016. Physical and structural changes in shale associated with supercritical CO 2 exposure. Fuel 184, 289–303. https://doi.org/10.1016/j.fuel.2016.07.028

Yuvashree, S., Balavijayalakshmi, J., 2019. Graphene based nanocomposites for electrochemical detection of $H2O_2$. Materials Today: Proceedings 18, 1740–1745. https://doi.org/10.1016/j.matpr.2019.05.272

Zhang, G., Zhou, D., Wang, P., Zhang, K., Tang, M., 2020. Influence of supercritical CO_2-water on the micromechanical properties of sandstone. International Journal of Greenhouse Gas Control 97, 103040. https://doi.org/10.1016/j.ijggc.2020.103040

Zhang, L., 2017. Pore structure characteristics of tight sandstones in the northern Songliao Basin, China. Marine and Petroleum Geology 11.

Zhang, T., 2012. Effect of organic-matter type and thermal maturity on methane adsorption in shale-gas systems. Organic Geochemistry 12.

Zhang, W., Li, Y., Xu, T., Cheng, H., Zheng, Y., Xiong, P., 2009. Long-term variations of CO_2 trapped in different mechanisms in deep saline formations: A case study of the Songliao Basin, China. International Journal of Greenhouse Gas Control 3, 161–180. https://doi.org/10.1016/j.ijggc.2008.07.007

Zhao, X., Liao, X., He, L., 2016. The evaluation methods for CO_2 storage in coal beds, in China. Journal of the Energy Institute 89, 389–399. https://doi.org/10.1016/j.joei.2015.03.001

Zhu, H., Zhong, D., Zhang, T., Liu, G., Yao, J., He, C., 2018. Diagenetic controls on the reservoir quality of fine-grained “tight” Sandstones: A Case Study Based on NMR Analysis. Energy and Fuels 32, 1612–1623. https://doi.org/10.1021/acs.energyfuels.7b03734

Ziabakhsh-Ganji, Z., Kooi, H., 2014. Sensitivity of the CO 2 storage capacity of underground geological structures to the presence of SO 2 and other impurities. Applied Energy 135, 43–52. https://doi.org/10.1016/j.apenergy.2014.08.073

9 APPENDICES

9.1 APPENDIX A: SANDSTONE CORE SAMPLE MINERAL ALTERATIONS AFTER CO_2 TREATMENT

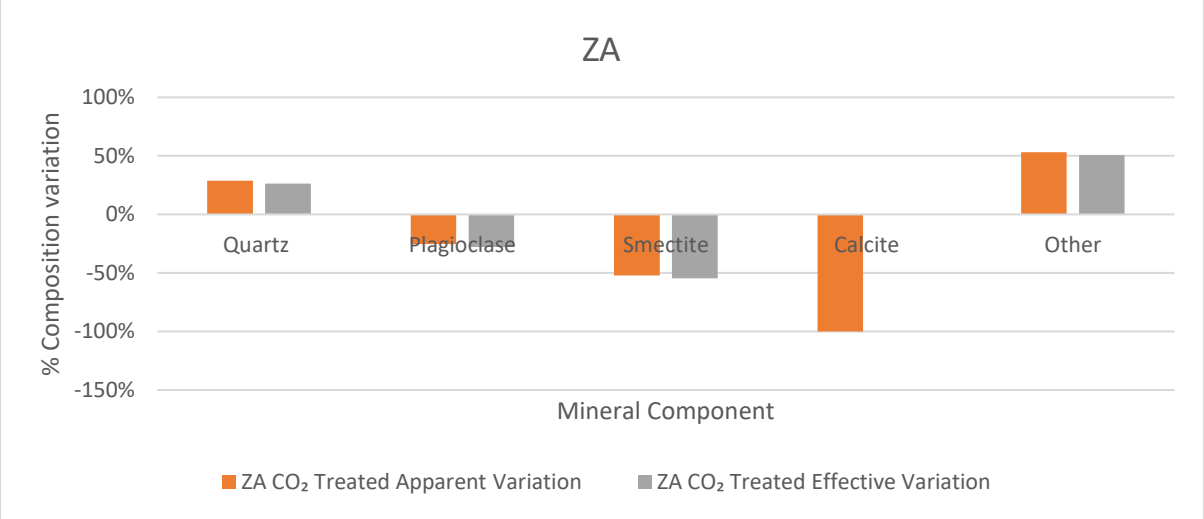

Figure A 9.1: ZA Sample Mineral Alterations

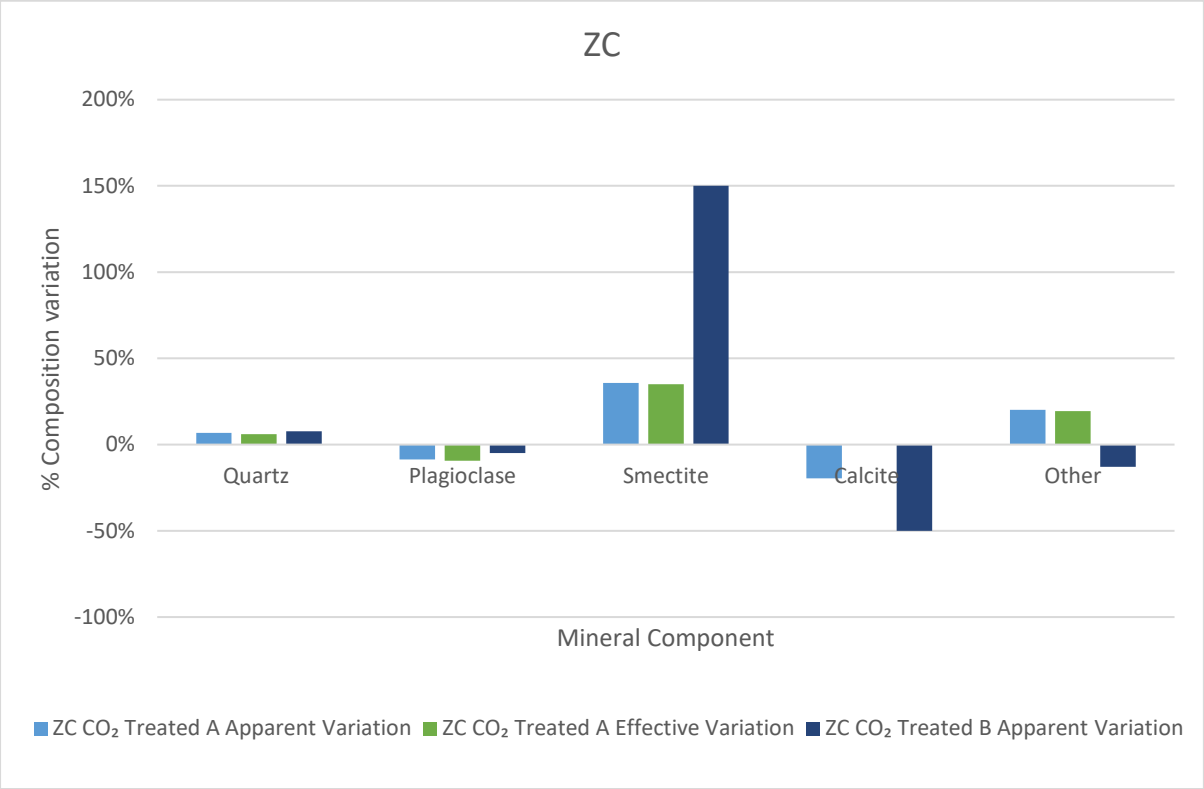

Figure A 9.2: ZC Sample Mineral Alterations

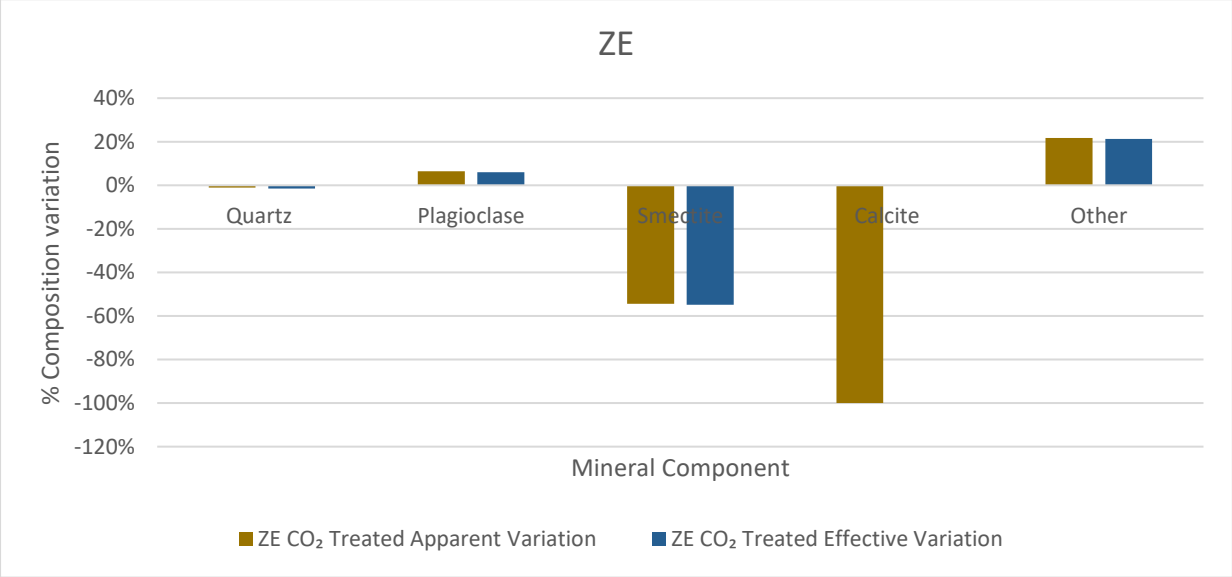

Figure A 9.3: ZE Sample Mineral Alterations

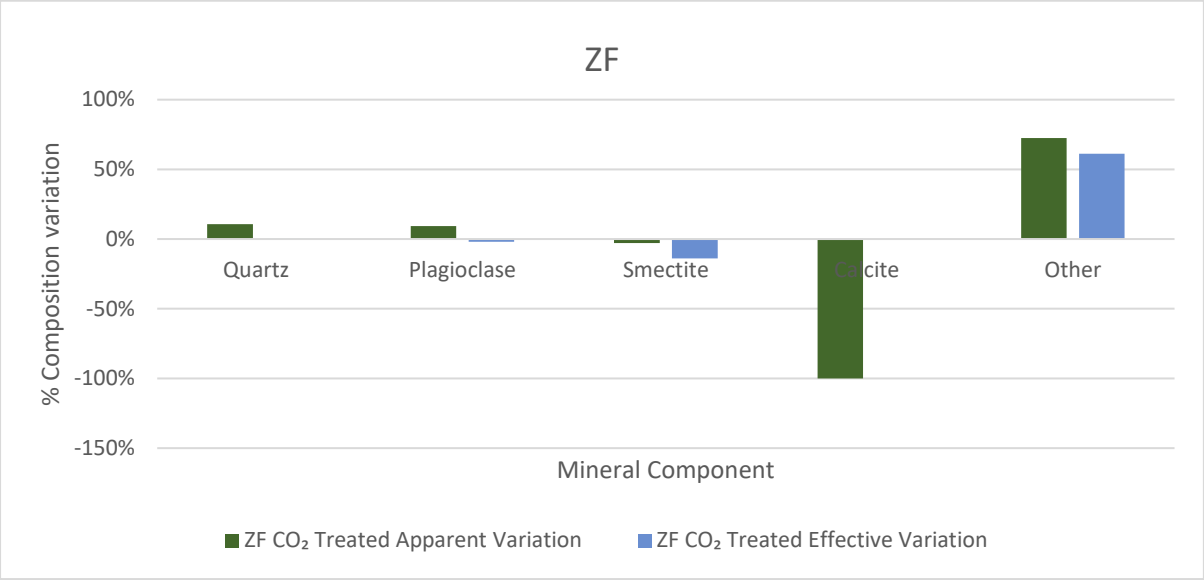

Figure A 9.4: ZF Sample Mineral Alterations

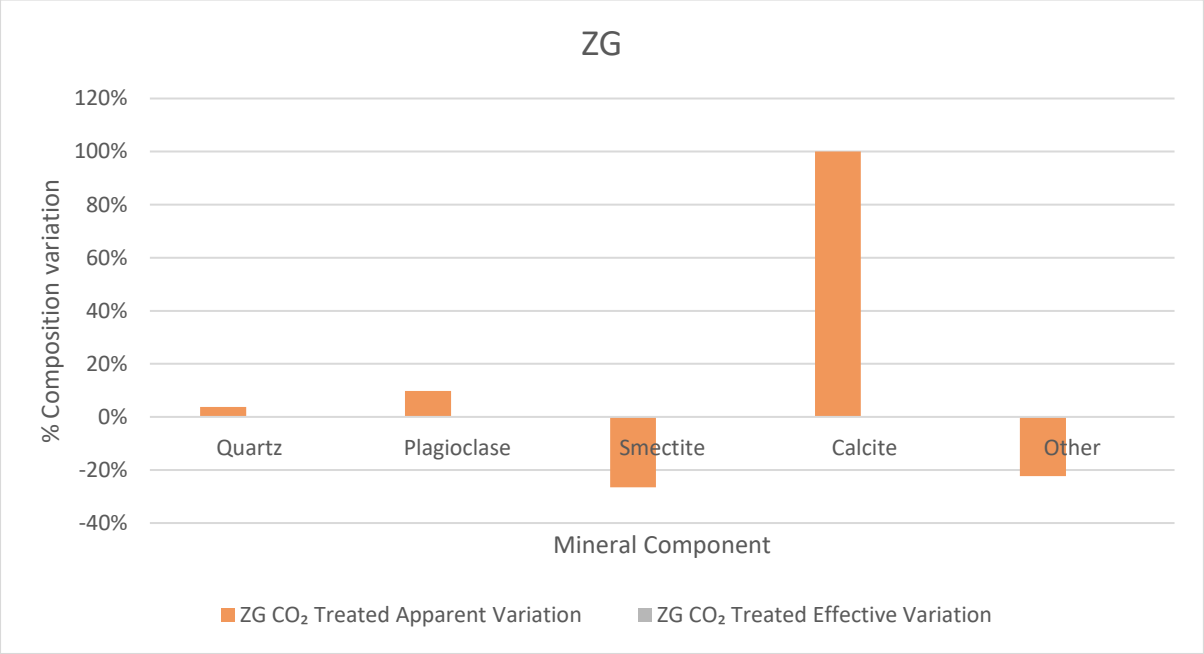

Figure A 9.5: ZG Sample Mineral Alterations